Numerical simulation of subcontinent lithosphere dynamics: craton stability, evolution and formation

Hongliang Wang
Department of Earth Science
Durham University

A thesis submitted for degree of
Doctor of Philosophy (PhD)
2015

Numerical simulation of subcontinent lithosphere dynamics: craton stability, evolution and formation

Hongliang Wang

Abstract

Through geodynamical modelling, two hypotheses about the craton stability and evolution were revisited and an important process of cratonization is investigated. Unlike most previous, related numerical studies, non-Newtonian rheology with composition dependence was used in these studies, and the rheological parameters are thus directly comparable with laboratory experiment of mantle. The first hypothesis, that the cratonic lithosphere is "isopycnic", is found to be not strictly necessary for craton stability and longevity. The high viscosity of the cratonic lithosphere due to compositional effects on the mantle rheology is found to be essential to maintain a thickness difference between cratonic and non-cratonic lithosphere for over billions of years and it allows a modest negative buoyancy of the cratonic root, depending on the strengthening factor due to the compositional effects. The second hypothesis to be tested is that mantle plume impingements cause rapid, significant removal of subcontinental lithosphere. The results presented in this thesis show that the erosion caused by a plume impact on a continent that is strong enough to have survived billions of years of Earth's history is rather limited. A special weakening mechanism of such highly viscous and buoyant roots is required to reactivate this cratonic lithosphere and thus cause significant thinning within 10s of Myrs. The fluid/melt-rock interaction during mantle metasomatism is probably the most likely mechanism to modify and weaken depleted cratonic lithosphere. Therefore, metasomatic weakening is essential for the significant thinning of subcontinental lithosphere observed, e.g.at North China Craton and Namibia, southern African, no matter whether caused by a plume impact or another tectonic event.

Using the reasonable compositional effects on the buoyancy and rheology of mantle rocks from the above studies, numerical experiments are performed to study the formation of thick cratonic lithosphere from a layered, depleted mantle material. In this scenario, substantial tectonic shortening and thickening of previously depleted material seems to be an essential ingredient to initiate the cratonization process. Afterwards, gravitational self-thickening will cause further thickening. Compositional buoyancy resists Rayleigh-Taylor instability collapse and stabilizes the thick cratonic root, while the secular cooling also has a stabilizing effect on the cratonic root by reducing the thermal buoyancy contrast between lithosphere and asthenosphere and increasing mantle viscosity. The presented numerical results are consistent with the vertical movement of cratonic peridotite as suggested on petrological grounds.

Contents

Declaration

I, Hongliang Wang, declare that this thesis, presented for the degree of Doctor of Philosophy at Durham University, is a result of my own original research and has not been previously submitted to Durham University or any other institution. I have clearly indicated, when appropriate, the contributions of colleagues and have made every effort to acknowledge all collaborative work.

Hongliang Wang

Durham University

Acknowledgement

I still clearly remember the feeling when I first saw the sky of United Kingdom. 29, Aug, 2011, a typical British day: rainy, quiet, I flew to Newcastle and took a taxi to Durham. It was one of the most important days in my life, because it actually marked my new life as a PhD student in Durham University, UK. Time has flown since then and now I'm approaching my degree of PhD after three and half year's hard-working. I would like to thank all the people I met and all the things I experienced that helped me to finish my PhD, both in life and work. However, some have contributed more than others and I would like to acknowledge them personally here.

First and foremost, thanks for Jeroen van hunen for all the work he has done to supervise my PhD project. The patient guidance and endless discussion he provided during these years have significantly improved my ability to do geodynamic research. It is almost impossible to do him all credit back, as he participated in every piece of my PhD work: topic selecting, coding, modelling, analysing, discussing, writing, publishing. He has shown his incredible ability to manage his time and energy to supervise me and other PhD students and Postdocs, as well as the heavy administration work. I have learned so much from him and there are still loads that I would like to learn. D. Graham Person at University of Alberta is another important person significantly shaped my PhD research, to whom I owe my special thanks. His great interest in my geodynamical modelling has always reminded me that I'm doing really important things. My appreciation especially goes to many of his long, detailed emails and his revision of my papers. I also owe my special thanks to Yaoling Niu. His scientific vision and enthusiasm has inspired me so much. He has been so kind to provide useful suggestions for my research as well as future career development. Mark Allen's kind suggestions about how to deliver one's own research by poster and oral presentation and useful discussion and revision for my 1st paper also deserve my sincere thanks. My acknowledgement also extends to Simon Mathias, Ed. Llewellin, Colin Macpherson, Helen William and other staff in Durham that help me during these years.

I would like to acknowledge the funding for my PhD project by "Topomod" from Marie Curie Initial Training Network (ITN). "Topomod" provides an international, friendly academic environment, of which I have enjoyed so much as a member. I feel really grateful to all the members, including the administration staff. I wish everyone in this community a very successful future career and happy life. Thanks for the unforgettable friendships from Odin, Tasca, Gabriele, Marine, Konstantinos, Sanjay, Mehdi, Gianluca, Elisa, Siddique, Lars, Jan, Agi, Antoine, Melody. Special thanks to Antoine for his helpful suggestion and discussion without reservation and to Manel Fernandez for his kind invitation for a academic visit to Institut de Ciències de la Terra Jaume Almera (Barcelona, Spain) and his hospitality.

I shall also acknowledge the editors and reviewers of my two published or accepted papers. The successful publications of these two papers in EPSL and G-cubed have relexed me and encouraged me to achieve more. I thank these editors and reviewers for the constructive suggestions and reviews: Yanick Ricard, Thorsten Becker, Shijie Zhong, Sally Gibson, Masaki Yoshida and two anomalous reviewers. Thanks to Kathy Mather for providing the support to my study of the Southern Africa. Thanks Jeroen, Graham and Mark for the most valuable work as the co-authors of my papers.

I also own my thanks to the department of Earth Sciences at Durham University as the administration staff, especially Paula and April, have provided so much convenience for my research. I have benefited a lot from the geodynamics group by the daily communication and discussion, so thanks very much to Kathy, Valentina, Pierre, Roberto, Andy, Lars, Benjamin, Nicolas, Becky and Jordan. My thanks also extend to many other fellow postgraduates and postdoc in the department: Rachael, Alan, Zhuoli (Bill), Yuanyuan, Jinxiu, Sarah, Amelie, Hui, Helen, Alexs, Susane, Bansri, Claire, Andy, Salim, Loraine, Kate, Joise, Helena, Leo, Fran, David, Peters, Stephen, Ian, Jack, Rikan, Lily, Jing, Dr. Stone, Yang, Ang, Longxun, Guanghui, Junjie, Dr. Tang, Xiang and so on. Special thanks to these people for the proofreading of my thesis: Mark, Alan, Ben, Yang. Also special thanks to Corrado, Lilian, Xuan, Vishal, Sheng, Dr. Tang and Alan for their friendship during my PhD work and thesis writing.

The day in England has now passed just like every normal one in my life before I came here. Nothing sounds really extraordinary. I get used to hear the voices of my family over the phone across the whole Eurasian continent in China, from which I keep gaining power all the time as I know. However, when I compare my life before and after I came to England in my mind, there is always a moment that I could not believe how all these amazing things happened on me. Therefore, this thesis is dedicated to this fantastic period of my life in England.

Chapter 1

Introduction

The theories of plate tectonics and mantle convection provide a comprehensive view of how the silicate Earth evolves. Despite the efficiency of these mechanisms for recycling of material, as shown by the formation and subduction of modern oceanic lithosphere within about 200 Myrs, there are portions of the Earth's surface that are found to be older than 3.8 Ga, that is almost 85% of the history of the Earth [*Bowring et al.*, 1989; *Liu et al.*, 1992; *Bowring and Williams*, 1999]. These areas, together with slightly younger Archean areas (>2.5Ga), are referred to as cratons ("kratos" means strength in Greek) and are recognized as the most geologically inactive and tectonically stable parts of our Earth (Fig. 1.1, [*Pearson and Wittig*, 2008]). Stable continental terranes that 'only' date back to Proterozoic are sometimes called Proterozoic cratons or Protons [*Griffin et al.*, 2003b; *Lee et al.*, 2011]. Although seismic studies suggest that Protons might have a similar thermal structure [e.g. *James et al.*, 2001; *Goes et al.*, 2005], they have substantially different composition and longevity compared to Archean cratons. In this thesis, we use the word cratons as Archean cratons, and do not include Proterozoic cratons. Due to their long history, cratons provide unique information about early Earth evolution. Some first-order observations about Archean cratons include (modified from [*Kusky et al.*, 2007]):

1) Many cratons are preserved in the interior of continents (Fig.1.1), and it is difficult to map the exact margins of cratons [*McKenzie and Priestley*, 2008].

2) Typically, low heat flows are measured in cratons, averaging 41±11mW/m^2 [*Morgan*, 1984; *Nyblade*, 1999; *Artemieva and Mooney*, 2001], compared to higher heat flux (>60~80mW/m^2) in most Phanerozoic regions [*Lee et al.*, 2011].

3) Cratonic lithosphere is characterized by high seismic velocities and extends significantly deeper than normal continental lithosphere and ocean lithosphere (>200km) [*Jordan*, 1978; *Sleep*, 2005; *Priestley and McKenzie*, 2013]. However, the existence of even thicker lithosphere (>250km) has been discarded using seismic anisotropy [*Gung et al.*, 2003], which is consistent with the maximum depth extent of kimberlitic xenolith studies [*Pearson and Nowell*, 2002] .

4) Diamonds are found from the kimberlites erupted from Archean cratonic lithosphere, which confirms the cold geotherms of thick cratonic roots as diamonds could only form in high pressure and low temperature environments [*Boyd and Gurney*, 1986].

5) Highly refractory, buoyant peridotites are found from kimberlitic xenoliths erupted from cratonic regions, which experienced large degrees of melt extractions [*Boyd*, 1989]. Worldwide samples show variable degrees of mantle metasomatic overprinting of these cratonic peridotites from different areas [*Erlank et al.*, 1987; *Carlson et al.*, 2005; *Tang et al.*, 2013].

6) Re/Os dating of cratonic peridotites demonstrates that the formation of cratonic mantle and crust are broadly coeval within error (i.e. ±200 Ma, see Fig. 1.2) [*Pearson et al.*, 1995; *Shirey and Walker*, 1998].

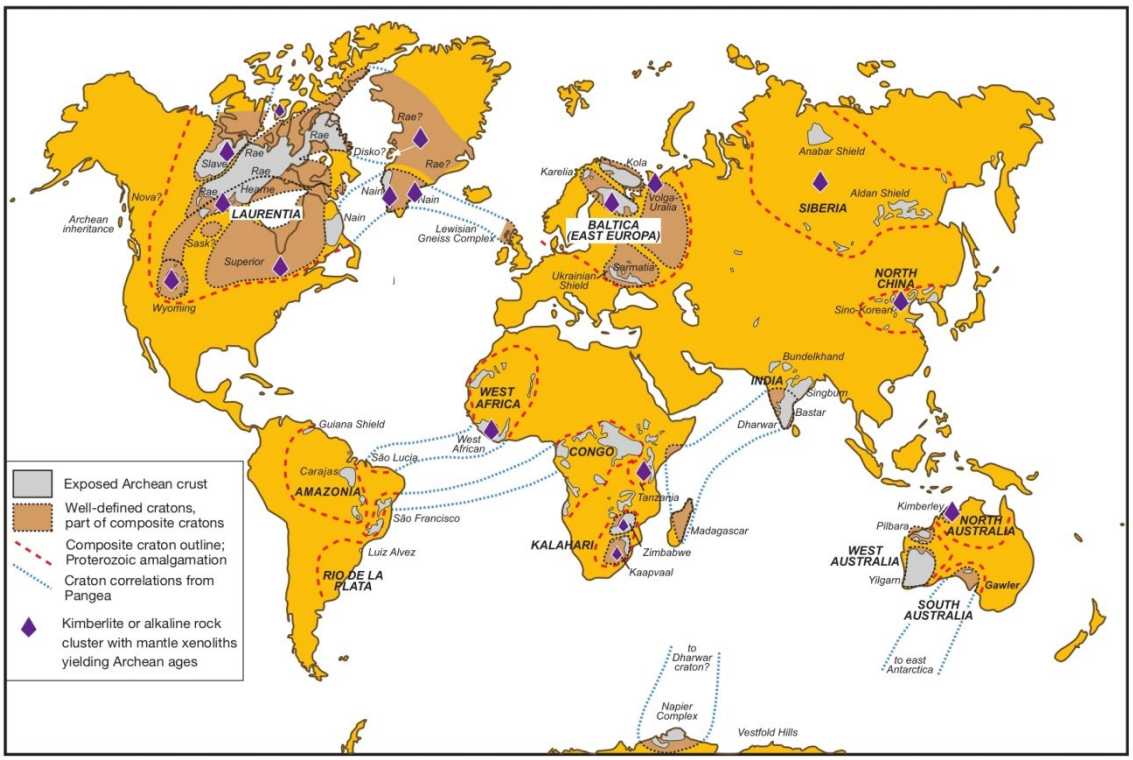

Fig. 1.1: *Global distributions of the Archean cratons and related geological observations (from* [*Pearson and Wittig*, 2014] *).*

These observations have made cratons as the most salient features at the Earth's surface (Fig. 1.1) as well as in Earth's mantle lithosphere. Based on these observations, the main aim of this thesis is to further our understanding of the cratons by using geodynamical modelling. The mechanism of the long term survival of cratons (both crust and mantle lithosphere) for over billions of year is probably the most apparent problem related to cratons. Fig. 1.1 indicates that the cratons are actually involved within plate tectonic activities (e.g. during the breakup of the Pangean supercontinent). Thus, it is important to know how cratons evolved through Earth's history, especially how they responded to major tectonic and mantle dynamic events. Furthermore, most cratons formed in the Archean, when the Earth was most likely much hotter and more vigorous than today [*Herzberg et al.*, 2010]. So it is not immediately apparent how cratons managed to stabilize and survive in such a dynamic environment. This thesis aims to provide a geodynamical perspective for these important scientific questions.

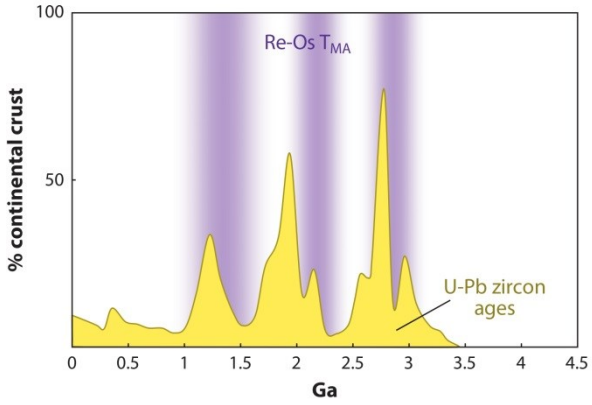

Fig. 1.2: *The age histogram for the crust (U-Pb zircon ages, in yellow) and mantle (Re-Os ages, in blue) (from* [*Lee et al.,* 2011]*) suggests that cratonic crust and mantle formed together.*

1.1 "Isopycnicity" and craton stability

Seismic tomography studies demonstrate that there are significant differences between the velocity structure of continental and oceanic lithosphere [e.g. *James et al.*, 2001; *Goes et al.*, 2005; *Priestley and Mckenzie*, 2006]. The compositional effects on the seismic velocities (both Vp and Vs) of mantle rocks are found to be secondary compared to the thermal effects [*Cammarano et al.*, 2003; *Schutt and Lesher*, 2006], thus the seismic velocity structure of the lithosphere is largely caused by the thermal variation between different types of lithosphere. As a result of the thermal contraction effect on the density, the thick and cool lithosphere would experience significant negative thermal buoyancy. This negative buoyancy, if not cancelled by other effects on the density, would almost certainly act to destabilise the thick cratonic thermal boundary layers, as suggested by Rayleigh-Taylor instability studies of the mantle lithosphere [*Houseman and Molnar*, 1997]. The "isopycnic" hypothesis was proposed to explain the long term survival of cratons [*Jordan*, 1978, 1988]. This hypothesis assumes that depletion-induced positive compositional buoyancy offsets the thermal negative buoyancy, and permanently results in a neutrally buoyant cratonic root. Indeed, cratonic lithosphere probably experienced significant amounts of melt depletion, which increases the Mg-number (Mg# = Mg/(Mg+Fe)× 100) and reduces modal garnet and clinopyroxene (cpx) of the cratonic peridotites, which results in significant chemical buoyancy of the cratonic root [*Boyd*, 1989; *Kelemen et al.*, 1992; *Pearson and Nowell*, 2002; *Kelly et al.*, 2003; *Carlson et al.*, 2005]. This chemical buoyancy of the cratonic root is large enough to offset at least some of the negative thermal buoyancy and contribute to the stability of cratons. By assuming the isostatic balance at the base of lithosphere, *Artemieva and Mooney* [2001] further estimate that the Archean cratonic mantle lithosphere needs to be 1.5% less dense due to chemical depletion effects, while the stable Proterozoic lithosphere should be 0.6-0.7% less dense.

However, to exactly cancel out the negative buoyancy of a gradually changing thermal boundary layer to maintain an "isopycnic" root, a gradually changing depletion profile of cra-

tonic peridotite (i.e. a gradual decrease in Mg# with depth) with an exactly opposite buoyancy effect is required. Well-stratified chemical layers with gradual depletion profiles are only observed at the Slave and Tanzanian cratons [*Lee and Rudnick*, 1999; *Kopylova and Russell*, 2000], but most other cratons don't have such well-stratified lithospheric roots [*Griffin et al.*, 1999, 2003b; *Pearson and Wittig*, 2014]. On the other hand, numerical modelling of the secular thermal evolution of cratonic lithosphere has demonstrated that the isopycnic state of cratonic lithosphere is an inherently ephemeral phenomenon [*Eaton and Claire Perry*, 2013]. The need to reconsider the long-term craton stability beyond the traditional isopycnic hypothesis is thus warranted.

1.2 Rheology of continental lithosphere

Beside chemical buoyancy, other mechanisms have been proposed for the long term stability of cratons, in particular specific rheological conditions, such as shielding by mobile belts surrounding cratons and the high strength of the cratonic root [*Lenardic and Moresi*, 1999; *Shapiro et al.*, 1999; *Lenardic et al.*, 2000; *Sleep*, 2003; *Burov and Watts*, 2006]. As the most abundant and probably weakest mineral in upper mantle material, polycrystalline olivine is suggested to dominate its rheology, and has a strong temperature, pressure, and stress dependence [*Karato and Wu*, 1993; *Kohlstedt et al.*, 1995; *Ranalli and Karato*, 1995]. By assuming that other major minerals, such as clinopyroxene (cpx), orthopyroxene (opx) and garnet, have little effect on the mantle rheology, the composition-dependent rheology is often ignored. Many dynamical observations can be explained through geodynamical modelling using Newtonian and non-Newtonian rheology without considering the rheological effects of composition [e.g. *Gurnis*, 1988; *Tackley*, 1998; *Zhong et al.*, 2000; *van Hunen et al.*, 2005]. The cool status of cratons, indeed, leads to stronger lithosphere compared to other types of lithosphere, but, by itself, such a cold viscous craton root doesn't seem to be able to resist billions of years of craton erosion by mantle convection [*Doin et al.*, 1997; *Shapiro et al.*, 1999; *Sleep*, 2003]. One of the main aims of this thesis is, therefore, to investigate the dynamical need for compositionally strong craton roots.

The compositional variation of the mantle lithosphere, especially the varying volatile (water, oxygen fugacity, melts) content are likely to have significant effects on the rheology [*Hirth and Kohlstedt*, 1996; *Mei and Kohlstedt*, 2000a; *Karato*, 2006; *Keefner et al.*, 2011]. It has been proposed that the dehydration of cratonic roots due to their exceptional melt depletion might contribute to the high strength and longevity of cratonic lithosphere [*Hirth et al.*, 2000; *Carlson et al.*, 2005; *Peslier et al.*, 2010]. However, the effects of water on mantle rheology in laboratory experiments vary considerably between different experiments [*Hirth and Kohlstedt*, 1996; *Karato*, 2010; *Fei et al.*, 2013]. *Hirth and Kohlstedt* [1996] found that the viscosity of water-saturated olivine aggregates is reduced by a factor of 100 ~180 at a confining pressure of 300 MPa (where the solubility of water is ~15.3 wt ppm or $250H/10^6$ Si). *Karato* [2010] proposed viscosity changes up to 4 orders of magnitude for a constant stress at depths of 200–400 km due

to the influence of water. On the contrary, a recent study of the silicon self-diffusion coefficient in forsterite suggests that the effect of water on upper mantle rheology is only up to one order of magnitude [*Fei et al.*, 2013]. This debate about the water effects on the mantle rheology has renewed the discussion on the mechanism of the long term survival of cratons. Throughout this thesis, composition-dependent rheology with laboratory data derived parameters is used to study and long term stability of cratonic lithosphere, as well as the specific dynamical scenarios such as plume-craton interaction and thickening of cratonic root.

1.3 Evolution of subcontinental lithosphere

Even though the Archean cratonic lithosphere is generally considered to be stable and dynamically inactive since it was formed, it is probably not isolated from the mantle convection and plate tectonics. The discovery that the North China craton (NCC) has lost more than 120 km of its lithosphere root in the Mesozoic [*Fan and Menzies*, 1992; *Gao et al.*, 2002b] provides an unique example of how cratonic lithosphere can be completely destroyed during Earth's evolution. There are some indications that other cratons or Proterozoic lithosphere have also experienced some degree of thinning or recycling, such as the Wyoming craton [*Goes et al.*, 2002; *Carlson et al.*, 2004], the Colorado plateau [*Levander et al.*, 2011], the Proterozoic lithosphere around the Kaapvaal craton [*Bell et al.*, 2003; *Mather et al.*, 2011], and the North Atlantic Craton (NAC) [*Tappe et al.*, 2007].

Besides the physical thinning and recycling of Precambrian lithosphere, there is also significant evidence for chemical modification of the lithosphere root over time. With the development of modern geochemical and petrological techniques, increasing evidence shows that much of the Precambrian lithosphere has experienced a progressive, multistage modification (or 'enrichment') to their roots through mantle metasomatism [e.g. *Carlson et al.,* 1995, 2005; *Hanghøj and Kelemen*, 2001; *Simon et al*., 2003; *Chesley et al.,* 2004; *Sand et al.*, 2009; *Janney et al.*, 2010; *Tappe et al.*, 2011; *Tang et al.*, 2013; *Smit et al.,* 2014]. Through fluid/melt-rock interaction, metasomatic refertilization might increase the density and weaken the subcontinental lithospheric mantle (SCLM) and thus affect its stability [*Carlson et al.*, 2005; *Foley*, 2008; *Pearson and Wittig*, 2008; *Schutt and Lesher*, 2010]. Metasomatic processes might also have a weakening effect on the rheology of the constituent peridotites by adding water to the originally dry, depleted continental root [*Peslier et al.*, 2012]. Hydrous metasomatism, induced by water release from a stagnant slab in the transition zone underneath northeast China has been suggested to cause the destruction of the NCC [*Niu*, 2005].

Therefore, it is important to understand how stable subcratonic lithosphere responds to major tectonic events (such as mantle plume impingements, nearby subduction events, or continental collision) and their related metasomatic modification. What are the main controlling factors in the thinning of the cratonic lithosphere? Is it the tectonic events themselves or rather the met-

asomatism they induce? More specifically, it is important to understand under which conditions stable cratonic lithosphere would be completely destroyed or significantly thinned when using realistic rheologies.

1.4 Origin and formation of cratonic lithosphere.

Beside their long term stability and evolution, another important scientific question is the origin and formation of these chemically distinctive cratonic roots. *Sleep* [2005] suggested that cratonic lithosphere formed by processes analogous to modern tectonics. There are mainly three endmember hypotheses for the formation of cratonic lithosphere [*Pearson and Wittig*, 2008; *Arndt et al.*, 2009; *Lee et al.*, 2011]: 1. extensive melting in a mantle plume; 2. accretion and stacking of oceanic lithosphere; 3. accretion of the arc lithosphere. There has been much debate regarding the relative importance of mantle plumes versus subduction in this context [*Lee*, 2006; *Aulbach*, 2012; *Pearson and Wittig*, 2014]. The melting depth of the peridotitic protolith provides one of the key constraints in this debate [*Herzberg*, 1999; *Canil*, 2004; *Pearson and Wittig*, 2008, 2014; *Lee and Chin*, 2014]. High pressure (3-6 GPa) melting conditions of craton protoliths as obtained from bulk-rock major element studies are used as evidence for a plume origin [e.g. *Herzberg*, 1999; *Aulbach*, 2012], although this approach does not consider later metasomatic processes [*Lee*, 2006; *Pearson and Wittig*, 2008]. Recently, *Lee and Chin* [2014] explicitly calculated the temperature and pressure of peridotite melting through the bulk FeO and MgO of the residual peridotite and concluded that Archean cratonic peridotites are likely to be formed at melting temperatures of 1400-1750^{o}C at 30-150 km and then transported to depths of 120-200 km.

Geological evidence also suggests that vertical tectonics (i.e. tectonics in the form of pure shear shortening and stretching, rising diapirs and sinking Rayleigh-Taylor instabilities inside the lithosphere, as opposed to the more horizontal movements associated with plate tectonics) might have been more dominant in the Archean [*Choukroune et al.*, 1995; *Bédard et al.*, 2003; *Sleep*, 2005]. The oval-shaped TTG terranes surrounded by greenstone belts in the east Pilbara have commonly been suggested to be an example of the surface expression of such vertical tectonics [*Van Kranendonk et al.*, 2014]. Thus, the compressive thickening might have been an important process for cratonization in the Archean [*Jordan*, 1978]. A modern example of such compressive thickening is the Tibetan plateau, where it has been suggested that a new craton is forming [*McKenzie and Priestley*, 2008]. This thesis addresses some of these considerations by studying the vertical movement or the compressive thickening process in the Archean environment and investigating how it relates to the formation and stabilization of cratons, which might also help to understand why most cratons were formed in Archean.

1.5 Thesis outline

The primary focus of this thesis is to investigate the main controlling factors on the long term stability and evolution of cratonic roots and how such roots originally formed and stabilized. This will be done using geodynamical modelling. The methodology parts are described in Chapter 2 to 4. Chapter 2 describes the governing equations of mantle convection, rheology and state. Chapter 3 deals with the applied numerical methods including short descriptions of the finite element method and the particle-in-cell (PIC) method as well as some benchmarks of the code. Chapter 4 describes a conservative velocity interpolation developed for the particle advection in the PIC method and its advantage. The remaining four chapters present the main scientific results of this thesis. Chapter 5 studies the craton stability and longevity by using composition-dependent non-Newtonian rheology and results are compared with experimental laboratory data on mantle rheology. Chapter 6 further extends this approach to a composite rheology between Newtonian and non-Newtonian rheology and studies the mechanical erosion of cratonic lithosphere by plume-induced mantle flow. It shows that such plume-related erosion on the originally stable cratonic lithosphere is rather limited, and that metasomatic weakening must play an essential role on the thinning and recycling of the cratonic lithosphere. In Chapter 7, numerical experiments are performed to model the thickening and stabilization of thick cratonic roots from a horizontal layer of depleted viscous mantle material. It illustrates that the compressive thickening is a dynamically viable process in the formation of cratons and that secular cooling has a stabilizing effect on cratons in an Earth that started off much hotter than it is today. This thesis ends with a final chapter with some suggestions for future studies in this research area.

Chapter 2

Mathematic equations and physical model

2.1 Governing equations

The solid rock of the mantle deforms and flows like a fluid on geological time scales, and as such mantle convection follows the principles of general fluid dynamics. For simplicity, three assumptions are often adopted, especially for the dynamics of the upper mantle: 1. incompressible flow; 2. infinite Prandtl number (ratio between the momentum diffusivity and thermal diffusivity, Pr=~10^{23} for the Earth's mantle) that makes inertial forces negligible; 3. The (Extended) Boussinesq approximation [*Mckenzie et al.*, 1974; *Schubert and Turcotte*, 2004]. Generally speaking, the following non-dimensional governing equations for mass, momentum and energy conservation are solved:

$$\nabla \cdot \mathbf{u} = 0 \tag{2.1}$$

$$-\nabla P + \nabla \cdot \left(\eta\left(\nabla \mathbf{u} + \nabla^{T} \mathbf{u}\right)\right) + \left(RaT - Rb_{i} C_{i}\right)\mathbf{e}_{z} = 0 \tag{2.2}$$

$$\frac{\partial T}{\partial t} + \mathbf{u} \cdot \nabla T = \nabla^{2} T + Q_{0} + \frac{Di}{Ra}\eta \dot{\varepsilon}^{2} + Di\,(T + Ts)\mathbf{u}_{z} \tag{2.3}$$

A standard non-dimensionalisation is used, with $x = x'h,\ t = t'h^{2}/\kappa,\ \eta = \eta'\eta_{0}$, where, in the equations above, the primes of the non-dimensional parameters are dropped for clarity. The dimensional physical parameters and their scaling factors are listed and explained in Table 2.1. The last two terms in Eq. (2.3) are added as an extension to the normal Boussinesq approximation (which makes it the so called "Extended Boussinesq Approximation") and correspond to viscous dissipation and adiabatic heating, respectively [*Christensen and Yuen*, 1985; *King et al.*, 2010]. The Rayleigh numbers Ra (thermal), Rb_i (chemical) and dissipation number Di are defined as:

$$Ra = \frac{\alpha \rho_{0} \Delta T g h^{3}}{\kappa \eta_{0}} \tag{2.4}$$

$$Ra = \frac{\delta \rho_{i} g h^{3}}{\kappa \eta_{0}} \tag{2.5}$$

$$Di = \frac{\alpha g h}{C_{p}} \tag{2.6}$$

Table 2.1 Symbols, units and default parameters.

Sym-bol	Description	Default value and units	Scaling factors[b]
A	rheological pre-exponent (dislocation)	$[MPa^{-n}s^{-1}]$	
B	rheological pre-exponent (diffusion)	$[MPa^{-1}]$	
E	activation energy	[kJ/mol]	$R\Delta T$
V	activation volume	$[cm^3/mol]$	$R\Delta T/\rho gh$
g	gravitational acceleration	9.8 $[m/s^2]$	
h	model height	[km]	
C_p	thermal capacity	1250 $[J\ kg^{-1}K^{-1}]$	
n	power law exponent	[-]	
P	deviatoric pressure	[Pa]	$\kappa\eta_0/h^2$
R	gas constant	8.3 [J/mol]	
Ra	thermal Rayleigh number	[-]	
Rb	compositional Rayleigh number[a]	[-]	
T	temperature	$[^0C]$	ΔT
T_s	surface temperature	273 [K]	
ΔT	temperature drop	$[^0C]$	
$\dot{\varepsilon}$	strain rate	$[s^{-1}]$	κ /h^2
α	thermal expansion coefficient	$3.5x10^{-5}$ $[K^{-1}]$	
η_0	reference viscosity	10^{20} [Pa·s]	
η	viscosity	[Pa·s]	η_0
κ	thermal diffusivity	10^{-6} $[m^2/s]$	
ρ	mantle density	3300 $[kg/m^3]$	
$\Delta\rho_1$	density difference of upper crust and mantle	600 $[kg/m^3]$	
$\Delta\rho_2$	maximum density change due to depletion	52.5 $[kg/m^3]$	
Q_0	radioactive heat production	0.02 $[\mu W/m^3]$	$\kappa\rho Cp\ \Delta T\ /h^2$
C_i	composition field	0~1 [-]	
$C\eta$	rheologically effective composition value[a]	0.6 [-]	
$\Delta\eta_0$	strengthening factor when $C\geq C\eta$	[-]	
t	time	[s]	h^2/κ
$\boldsymbol{e}_z$	vertical unit vector	[-]	
$\boldsymbol{u}$	velocity vector	m/s	κ/h

[a] $C\eta$ is chosen such that the second cratonic layer has the maximum strengthening factor due to its initial compositional field.

[b] Scaling laws are depicted as $X=X'*S_x$, where X, X', S_x are the dimensional value, non-dimensional value and scaling factor, respectively.

The chemical convection is simulated by solving the following composition conservation equation with particle-in-cell (PIC) method:

$$\frac{\partial C_i}{\partial t} + (\mathbf{u} \cdot \nabla \quad) C_i = 0 \tag{2.7}$$

2.2 Rheology of upper mantle

The rheology of the upper mantle material is mainly controlled by temperature, pressure and stress and it has been suggested that mantle rheology is dominated by that of olivine (most abundant mineral, >50% in the upper mantle), and that the other minerals (cpx, opx, garnet, etc.) make little difference to the rheology of upper mantle [*Karato and Wu*, 1993; *Ranalli and Karato*, 1995; *Hirth and Kohlstedt*, 1996]. Many observations can be explained through geodynamical modelling without having to consider the rheological impact of compositional heterogeneity. However, without this consideration, the long term survival of cratonic lithosphere has proved to be difficult to explain [*Doin et al.*, 1997; *Sleep*, 2003; *King*, 2005]. Therefore, we aim to study the long term dynamics of the continental lithosphere by using a composition-dependent rheology in our numerical models.

2.2.1 Rheological law

The deformation of rocks at high temperature, high pressure such as in earth's interior can be described by [*Ranalli and Karato*, 1995] :

$$\dot{\varepsilon} = A \sigma^n d^m exp\left(-\frac{E + PV}{RT}\right) \tag{2.8}$$

where σ is the deviatoric stress, d is the grain size, m is the exponent of grain size. Other variables are described in Table 2.1. However, in numerical studies, the rheological property of rock is often used as an “effective viscosity”:

$$\eta = A^{(-\frac{1}{n})} \dot{\varepsilon}^{(\frac{1-n}{n})} exp\left(\frac{E + \rho g z V}{nRT}\right) \tag{2.9}$$

If n = 1, the viscosity doesn't depend on the applied deviatoric stress. This is referred to as “Newtonian rheology”, and applies to diffusion creep. The simplicity and numerical efficiency of Newtonian rheology has made it very popular in the geodynamic research and can be used to explain many geodynamic phenomena. However, rheological laboratory studies on mantle material suggest that the dominant creep mechanism in the upper mantle is dislocation creep [*Karato*, 2010], which is characterized by a non-Newtonian rheology (n>1).

While the rheological parameters of a mantle peridotite (dominated by olivine) are well determined by the laboratory studies, the rheology of crustal rocks is less constrained. In order to simplify the model and focus on the mantle dynamics, we ignore the rheological differences between mantle and crust in the models described in Chapters 5 and 6.

2.2.2 Composition-dependent rheology

The survival of cratons from the time of their formation in the Archean requires a cratonic root that is stronger than normal mantle material [*Sleep*, 2003]. Volatiles, especially water, are found to be one of the dominant influences on mantle rheology [*Mei and Kohlstedt*, 2000a, 2000b; *Karato*, 2010; *Keefner et al.*, 2011]. The dehydration of cratonic roots due to their high melt depletion has long been proposed to contribute to the high strength of cratonic lithosphere [*Hirth et al.*, 2000; *Carlson et al.*, 2005; *Peslier et al.*, 2010]. However, the effects of water on mantle rheology in laboratory experiments vary considerably between different experiments [*Hirth and Kohlstedt*, 1996; *Mei and Kohlstedt*, 2000b; *Karato*, 2010; *Fei et al.*, 2013]. *Hirth and Kohlstedt* (1996) found that the viscosity of water-saturated olivine aggregates is reduced by a factor of 100 ~ 180 at a confining pressure of 300 MPa (where the solubility of water is ~15.3 wt ppm or 250H/106 Si). *Karato* [2010] proposed viscosity changes up to 4 orders of magnitude for a constant stress at depths of 200–400 km due to the influence of water. In contrast, a more recent study of the silicon self-diffusion coefficient in forsterite suggests that the effect of water on upper mantle rheology is only up to one order of magnitude [*Fei et al.*, 2013]. The important but disputed effect of water has left the composition dependence of the rheology rather unconstrained by laboratory experiments to the present. Therefore, it is important to constrain to what extent this composition dependence of the rheology is required for the long-term stability of cratonic roots.

The composition dependence of the mantle rheology is characterised by a strengthening factor $\Delta\eta$ in the numerical experiments presented in this thesis:

$$\eta_{dl} = A^{(-\frac{1}{n})} \dot{\varepsilon}^{(\frac{1-n}{n})} exp\left(\frac{E + \rho gzV}{nRT}\right) \times \Delta\eta \tag{2.10}$$

$$\Delta\eta = \Delta\eta_0^{\min(1, \frac{C_2}{C_\eta})} \tag{2.11}$$

where C_2 is a composition value used to track the cratonic root material. This rheology has been used to study the craton stability and longevity during the normal plate mantle interaction in Chapter 5.

A composite rheology of non-Newtonian and Newtonian rheology is used to study the impact of a plume on the cratonic root and thickening of the cratonic root in Chapter 6 and 7, respectively. It is described by Eqs. (2.10)-(2.13).

$$\eta_{df} = Bexp\left(\frac{E + \rho gzV}{RT}\right) \times \Delta\eta^{n} \tag{2.12}$$

$$\eta_{eff} = min\left(\eta_{df}, \eta_{dl}\right) \tag{2.13}$$

Due to the non-linear stress-strain rate relationship used in the composite rheology, the effective compositional viscosity increase depends on the ambient stress or strain rate, and hypothetically two endmember situations exist. For the case that strain rate is kept constant, changing the strengthening factor Δη in Eq. (2.11) will change the effective viscosity proportionally. If, however, stress remains constant, then increasing $\Delta\eta$ will result in an effective viscosity increase of $\Delta\eta^n$. We report 'constant strain rate' values $\Delta\eta$, and values used in this thesis ($\Delta\eta$ =1, 2, 3, 4, 5, 6,10) correspond to 'constant stress' values of $\Delta\eta^n$ =1, 11.3, 46.8, 128, 279.5 and 529.1, 3162.3, respectively, for n=3.5. Laboratory experiments, including those in [*Hirth and Kohlstedt*, 1996; *Mei and Kohlstedt*, 2000b; *Karato*, 2010; *Fei et al.*, 2013] listed above, often report 'constant stress' values. Considering the significant variation in the results of laboratory experiments [*Hirth and Kohlstedt*, 1996; *Karato*, 2010; *Fei et al.*, 2013], the range of strengthening factors in this study is considered representative.

2.3. Thermo-chemical buoyancy

The main driving force behind the thermochemical convection is the buoyancy force from density variations. As we focus on the lithospheric dynamics of the cratonic root, we ignore any density variations due to phase transitions. Thus, the buoyancy force in the present models mainly consists of by two competing components: thermal and compositional buoyancy, as described by the following equation of state:

$$\Delta\rho(T, C) = \Delta\rho_c - \alpha\rho_0(T - T_s) \tag{2.14}$$

The symbols and descriptions are listed in Table 2.1. The reference density ρ_0 represents the density of the undepleted upper mantle under the condition of the Earth's surface. The composition-dependent term depends on the depletion of the cratonic root during its creation and the metasomatic refertilization afterwards. The mantle potential temperature in the Archean has been suggested to be 250-350 K higher than the present temperature [*Herzberg et al.*, 2010]. By using the standard thermal expansion coefficient and reference density as list in Table 2.1, a temperature difference of 250~350 K would give rise to a density variation of ~30 kg/m^3, which is comparable to the $\Delta\rho_c$. Combined with the fact that higher temperature also induce lower viscosity, this suggested that the mantle convection must been more vigorous and the dynamics for the cratonic lithosphere may have differed in the Archean, which will be discussed in Chapter 7.

Chapter 3

Numerical methods

3.1 Stokes solver

A Cartesian version of the finite element code Citcom [*Moresi and Solomatov*, 1995; *Zhong et al.*, 2000; *van Hunen et al.*, 2005] is used to solve the mass, momentum and energy conservation equations 2.1 - 2.3. The finite element (FE) method discretizes the model domain into many small subdomains, called finite elements, in which the variable field is described by a local simple function (shape function) of the values on local nodes. Through variational methods (the calculus of variations), the problem can be approximated by minimizing an associated error function. By solving the equivalent weak formulation that satisfies the boundary conditions, a numerical solution of the partial differential equations can be obtained. Citcom is based on a Galerkin weak-form FE formulation for the Stokes flow [*Hughes*, 2000] and uses 4-node quadrilateral elements. An Uzawa algorithm [*Atanga and Silvester*, 1992] is used to solve the matrix equations from the weak formulations of Eqs. (2.1) and (2.2). To avoid numerical instabilities in parts of the model domain where heat advection dominates over heat diffusion, the energy equation 2.3 is solved by a streamline upwind Petrov-Galerkin method (SUPG) [*Brooks*, 1981] with the velocity solution from Eq. (2.1) and (2.2). In order to speed up the computations, a multigrid solver is implemented that eliminates the iteration error simultaneously at different length scales [*Moresi and Solomatov*, 1995; *Zhong et al.*, 2000].

3.2 Particle-In-Cell methods

As we focus on the effects the composition has on the rheology and buoyancy in the mantle, the chemical field, which is updated according to Eq. (2.7), plays an important role in this work. To avoid the presence of unwanted numerical diffusion, Eq. (2.7) is solved with a particle-tracking technique [*van Hunen et al.*, 2000; *Ballmer et al.*, 2007]. In this method, tracers carry compositional information that is used for density and rheology calculations, and are advected at every time step by a 2nd order Runge-Kutta scheme. The velocities at which those tracers move are interpolated from the FE solution of Eqs. (2.1) and (2.2) at the element nodal points. The tracer composition values are, in turn, required by the FE method at the integration points inside every element in order to calculate the buoyancy and viscosity, but we simply use an average elemental value for all the integration points in an element. This value is calculated by interpolation from the tracers within a given control volume by using the "ratio" method described in [*Tackley and King*, 2003]. Usually, and also in this version of Citcom, this control volume is the local finite element. The implementation of this socalled 'Particle-In-Cell' (PIC) method in the code has been benchmarked against *van Keken et al.[* 1997] and *Schmeling et al.*[2008]. In or-

der to handle the particle inflow and outflow in the open boundary problems such as those described in Chapter 7, the particles within any element facing an open boundary (i.e. a boundary through which material can flow in or out of the computational domain) are refreshed at every time step (Fig. 3.1**)**: we first remove all the old particles in these elements and then refill them with randomly distributed particles. This technique uses a virtual pool of particles for the boundary elements, and this method maintains a statistically constant number of tracers in the computation domain. The new particles inherit the (interpolated) values of the old particles in the element. As we only do this in a single layer of elements, this technique does not affect the internal dynamics of the convection.

The commonly used velocity interpolation method to particles is bilinear (2D) or trilinear (3D) interpolation, which induces particle clustering and dispersion in regions of strong velocity gradients. To avoid these problems, we developed and implemented a solution to this problem by implementing a conservative, divergence-free velocity interpolation, which will be discussed in Chapter 4.

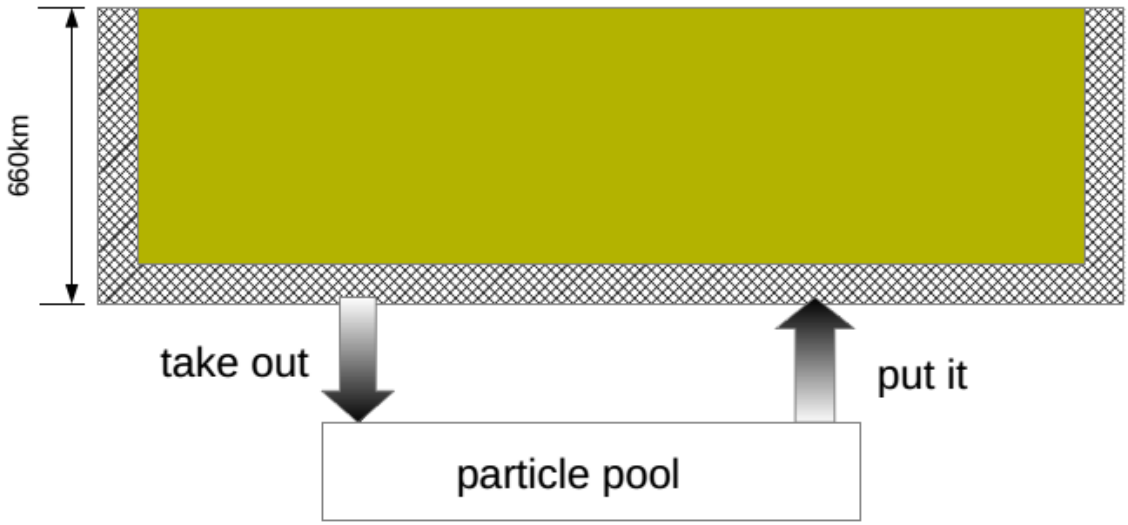

Fig. 3.1: *The particle refreshment in the boundary elements where there are particles inflow/outflow.*

3.3 Non-Newtonian rheology tests

The implementation of non-Newtonian rheology has been benchmarked using the results of *Christensen* [1984], who shows 2-D results for non-Newtonian rheology convection for a range of rheological parameters. As temperature plays a dominate role on the viscosity contrast in our models, we choose his case 4.2b (strong pressure and temperature dependence) and 4.4b (temperature dominated viscosity) as two benchmark problems for the non-Newtonian rheology. The Newtonian rheology counterparts (case 4.2c and 4.4c) of these two cases are also calculated for comparison. The reader is referred to *Christensen* [1984] for the detailed descriptions of model setup for these convection problems.

The steady state solutions of these four cases are calculated for comparison with the published benchmark results. Fig. 3.2 shows the viscosity and temperature field comparison (case 4.2b, 4.2c) between the results from Citcom and the result from *Christensen* [1984]. As the contours in Fig. 3.2 illustrate, our results have very similar (or almost the same) patterns of viscosity and temperature structures when compared to the benchmark results. Similar comparison results can also been seen for case 4.4b and 4.4c, as showed in Fig. 3.3. The Nusselt number, which characterises the ratio of the convective and conduction heat transfer across the boundary, is often used for the benchmarking for the mantle convection problems [e.g. *Blankenbach et al.*, 1989; *King et al.*, 2010]. Table 3.1 shows the Nusselt number and root mean square of the velocity for cases 4.2b and 4.4b with different resolutions. The similar results of the medium and high resolution models indicate convergence of these two models with improved resolution. The difference of the Nusselt numbers between the medium resolution (105-by-75) and the result of *Christensen* [1984] is within 5%. These comparisons confirm that both the Newtonian and non-Newtonian rheology are correctly implemented in Citcom.

Christensen [1984] illustrated that if activation enthalpy for the Newtonian case is reduced by a factor X compared to the non-Newtonian case, the two models share similar temperature structures with their non-Newtonian counterparts, even though their viscosity structure differs significantly. This characteristic is commonly used in numerical studies to mimic the effectts of non-Newtonian rheology using a computationally more efficient Newtonian rheology (e.g. van Hunen et al., 2005). However, it is worth noting that the similarity in the temperature field is only observed in steady state situations, and the time dependent fluid dynamics can be quite different between models with Newtonian and non-Newtonian rheology. Thus, it is worthwhile to use fully non-Newtonian rheology models to study the long term dynamics of the continental lithosphere such as described in Chapters 5, 6 and 7.

Table 3.1 Comparison of the Nusselt number and root mean square velocity for case 4.2 and 4.4c (*Christensen* [1984])

	50x70		75x105		100x140		Christensen[1984]
	Nu	Vrms	Nu	Vrms	Nu	Vrms	Nu
Case4.2b	8.01	2.350e2	8.355	2.3044e2	8.46	2.290e2	8.59
Case4.4b	7.72	1.529e2	7.78	1.530e2	7.75	1.524e2	7.77

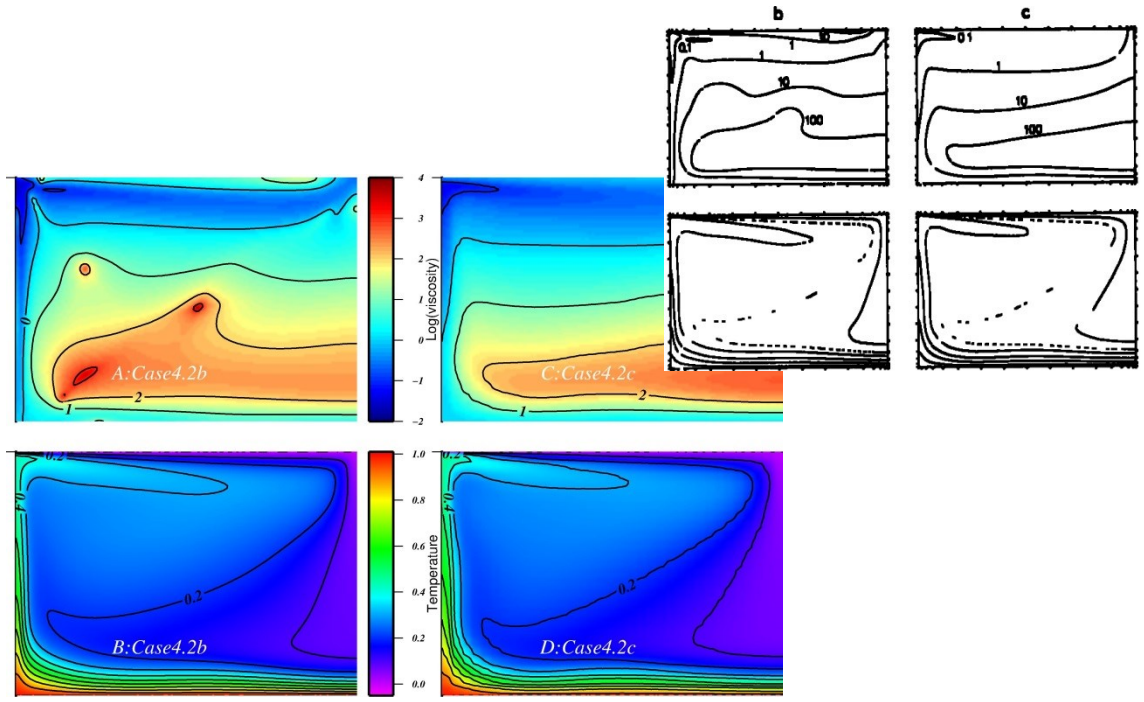

Fig. 3.2: *Viscosity and temperature comparison between our numerical results (down) with the case 4.2b and 4.2c in Christensen [1984] (right). Strong pressure and temperature dependent viscosity is used in these models. Case 4.2b and 4.2c use non-Newtonian and Newtonian rheology, respectively.*

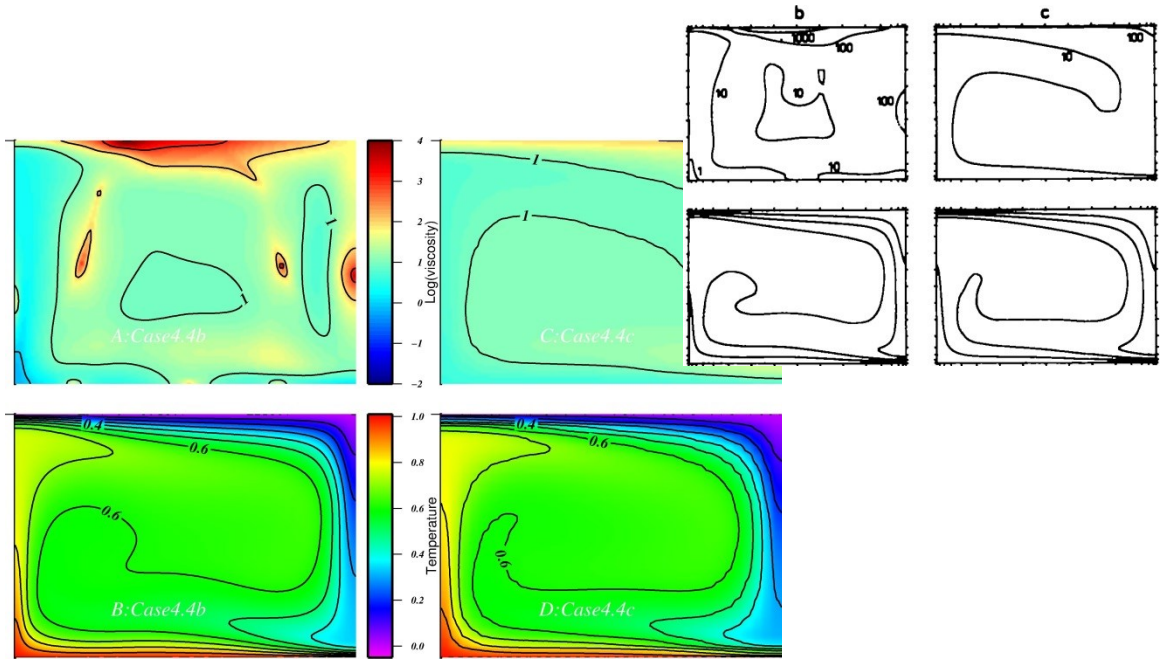

Fig. 3.3: *Viscosity and temperature comparison between our numerical results (down) with the case 4.4b and 4.4c in Christensen [1984] (right). Strong temperature dependent viscosity is used in these models. Case 4.4b and 4.4c use non-Newtonian and Newtonian rheology, respectively.*

Chapter 4

Advantages of a conservative velocity interpolation (CVI) scheme for particle-in-cell methods with application in geodynamic modelling[1]

Abstract

The particle-in-cell method is generally considered a flexible and robust method to model the geodynamic problems with chemical heterogeneity. However, velocity interpolation from grid points to particle locations is often performed without considering the divergence of the velocity field, which can lead to significant particle dispersion or clustering if those particles move through regions of strong velocity gradients. This may ultimately result in cells void of particles, which, if left untreated, may, in turn, lead to numerical inaccuracies. Here, we apply a two-dimensional conservative velocity interpolation scheme (CVI) to steady state and time-dependent flow fields with strong velocity gradients (e.g. due to large local viscosity variation), and derive and apply the three-dimensional equivalent. We show that the introduction of CVI significantly reduces the dispersion and clustering of particles in both steady-state and time-dependent flow problems, and maintains a locally steady number of particles, without the need for ad-hoc remedies such as very high initial particle densities or re-seeding during the calculation. We illustrate that this method provides a significant improvement to particle distributions in common geodynamic modelling problems such as subduction zones or lithosphere-asthenosphere boundary dynamics.

[1] This Chapter has been accepted for publication to Geochemistry, Geophysics, Geosystems as "Advantages of a conservative velocity interpolation (CVI) scheme for particle-in-cell methods with application in geodynamic modelling" by Hongliang Wang, Roberto Agrusta, and Jeroen van Hunen. The methodology was elaborated and the manuscript written by H. Wang. The co-authors have participated in this study by providing training, feedback on the manuscript, the subduction model application, and useful discussions.

4.1. Introduction

Chemical heterogeneities play an important role in mantle dynamics and an accurate numerical method to treat them in geodynamic models is of prime importance [*Tackley et al.*, 2001; *McNamara and Zhong*, 2004]. Several techniques are used to track the composition field in computational fluid dynamics, and the particle-in-cell method (PIC), which advects composition-carrying particles with the ambient velocity field, is found to be a very flexible and robust method to model many geodynamical problems [*van Keken et al.*, 1997; *Tackley and King*, 2003], and is commonly used in the mantle convection community [e.g. *van Keken et al.*, 1997; *Schmeling*, 2000; *Gerya and Yuen*, 2003b; *Moresi et al.*, 2003; *Tackley and King*, 2003; *Ballmer et al.*, 2009].

The algorithm of the PIC method to track the composition field typically involves 1) velocity interpolation from a grid of computational nodal points (hereafter collectively referred to as the mesh) to the particle locations, 2) time-integrated advection of the particles, and 3) interpolation of the particle information to the mesh. For most problems, a 2^{nd} or 4^{th} order Runge-Kutta scheme usually proves to be sufficiently accurate to advect the particles [*Gerya and Yuen*, 2003b; *Moresi et al.*, 2003; *McNamara and Zhong*, 2004]. Although a commonly used bilinear or biquadratic velocity interpolation to and from the particles may be sufficiently accurate for many flow problems [*van Keken et al.*, 1997; *Gerya and Yuen*, 2003b; *Tackley and King*, 2003], these methods interpolate the velocity components independently, without considering the divergence of the velocity field. Such interpolation schemes might induce non-physical clustering of the particles, depending on the flow field [*Jenny et al.*, 2001; *Meyer and Jenny*, 2004]. This effect may not be significant or obvious when the velocity field is rather smooth, but an unphysical distribution of the particles can become significant if strong velocity gradients are present. Ultimately, this may result in grid cells or elements totally void of particles, which are sometimes remedied using locally very high mesh resolutions and/or particle densities, or various ad-hoc solutions, such as assuming a default composition for those empty cells, or repeated reseeding with additional particles [*Poliakov and Podladchikov*, 1992; *Weinberg and Schmeling*, 1992; *Edwards and Bridson*, 2012]. As we will illustrate below, this problem can be particularly severe in case of geodynamical applications with sharp viscosity contrasts and thus strong velocity gradients, such as plate interfaces in subduction zones.

An improved velocity interpolation scheme that conserves the divergence of the flow field has been developed by *Jenny et al*. [2001] and the simplified scheme for incompressible flow (i.e. divergence free) has been demonstrated that it largely eliminates the spurious distribution of particles for 2D incompressible flow problem [*Meyer and Jenny*, 2004]. Other types of divergence free interpolations has also been proposed for specific 2D incompressible flow field [*Vennell and Beatson*, 2009; *McNally*, 2011], although equivalent schemes for 3D flow are of-

ten absent. Impressed by the simplicity of the scheme in 2D Cartesian coordinate system as described by *Meyer and Jenny* [2004], we test it in our code and further develop the equivalent 3D scheme in this study. We illustrate that the divergence free interpolations (i.e. conservative velocity interpolation for incompressible flow) in both 2D and 3D calculations are very successful in many geodynamical scenarios where large local viscosity contrasts are common.

4.2 Method

4.2.1 Governing equations

To illustrate the concept of particle divergence in an incompressible, infinite Prandtl-number flow field, the following standard non-dimensional governing equations for conservation of mass, momentum, energy and composition are solved under the Boussinesq approximation:

$$\nabla \cdot \mathbf{u} = 0 , \tag{4.1}$$

$$-\nabla P + \nabla\left(\eta\left(\nabla \mathbf{u} + \nabla^{T}\mathbf{u}\right)\right) + \left(RaT - RbC\right)\mathbf{e}_{z} = 0 , \tag{4.2}$$

$$\frac{\partial T}{\partial t} + \mathbf{u} \cdot \nabla T = \nabla^{2} T , \tag{4.3}$$

$$\frac{\partial C}{\partial t} + \mathbf{u} \cdot \nabla C = 0 . \tag{4.4}$$

where ***u****, P, η, T, C, t, Ra and Rb* represent velocity, pressure, viscosity, temperature, composition, time, the thermal and compositional Rayleigh number, respectively, and e_z is the vertical unit vector positive upward.

For the steady state flow problems in section 4.3, analytical solutions for Eqs. (4.1) and (4.2) are applied at the nodes at every time step. In that case, particles are passively advected through the interpolated velocity field and do not affect the flow. For the time dependent flow problems in section 4.4, the flow field is solved numerically using a Cartesian finite element code Citcom [*Moresi and Solomatov*, 1995; *Zhong et al.*, 2000]. In the case of active particles, the composition field carried by the particles can have a feedback on the solution of Eqs. (4.2) and (4.3).

Eq. (4.4) is solved by a particle-tracking technique, in which the particles are advected at every time step by a 2nd order Runge-Kutta scheme with interpolated velocities based on the node velocities from Eqs. (4.1) and (4.2). The compositional value is then interpolated to the finite element integration points.

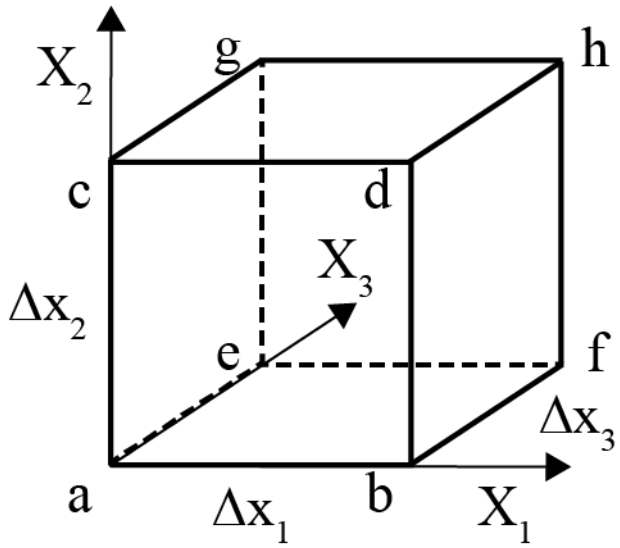

Fig. 4.1: *Schematic diagram to show the node name convention of a 3D finite element used in this study.*

4.2.2 Velocity interpolation scheme

The non-conservative interpolation from nodal points of a local finite element to any point within the element is done using a bilinear (in 2D) or tri-linear (3D) interpolation scheme with 2nd-order accuracy. In the general 3D case, this interpolated velocity U^L is defined as:

$$\begin{aligned} U_i^L(x_1,x_2,x_3) = {} & (1-x_1)(1-x_2)\left[(1-x_3)U_i^a + x_3 U_i^e\right] + \\ & x_1(1-x_2)\left[(1-x_3)U_i^b + x_3 U_i^f\right] + \\ & (1-x_1)\,x_2\left[(1-x_3)U_i^c + x_3 U_i^g\right] + \\ & x_1\,x_2\left[(1-x_3)U_i^d + x_3 U_i^h\right] \end{aligned} \tag{4.5}$$

where U_i is the ith-component of the velocity field at local coordinates (x_1, x_2, x_3) and superscripts a - h refer to the nodal points of the unit cell, as illustrated in Fig. 4.1. The improved conservative interpolation can be derived by adding a correction term to conserve the divergence velocity field after the interpolation. The 2D case for the incompressible flow is provided by *Meyer and Jenny* [2004], in which correction terms are added to the bilinear interpolations (Eq. (4. 5)):

$$U_i = U_i^L + \Delta U_i \tag{4.6}$$

with ΔU_i a correction term. Here, we derive the general, 3D version of this correction term for incompressible flow as:

$$\begin{aligned} \Delta U_1 &= x_1(1-x_1)(C_{10} + x_2 C_{12}) \\ \Delta U_2 &= x_2(1-x_2)(C_{20} + x_3 C_{23}) \\ \Delta U_3 &= x_3(1-x_3)(C_{30} + x_1 C_{31}) \end{aligned} \tag{4.7}$$

where the coefficients (C_{10}, C_{12}, C_{20}, C_{23}, C_{30}, C_{31}) are defined as (see Appendix A):

$$
\begin{aligned}
C_{12} &= \frac{\Delta x_1}{2\Delta x_3}\left[-U_3^a + U_3^b + U_3^c - U_3^d + U_3^e - U_3^f - U_3^g + U_3^h\right] \\
C_{23} &= \frac{\Delta x_2}{2\Delta x_1}\left[-U_1^a + U_1^b + U_1^c - U_1^d + U_1^e - U_1^f - U_1^g + U_1^h\right] \\
C_{31} &= \frac{\Delta x_3}{2\Delta x_2}\left[-U_2^a + U_2^b + U_2^c - U_2^d + U_2^e - U_2^f - U_2^g + U_2^h\right] \\
C_{10} &= \frac{\Delta x_1}{2\Delta x_2}\left[U_2^a - U_2^b - U_2^c + U_2^d\right] + \frac{\Delta x_1}{2\Delta x_3}\left[U_3^a - U_3^b - U_3^e + U_3^f + C_{31}\right] \\
C_{20} &= \frac{\Delta x_2}{2\Delta x_1}\left[U_1^a - U_1^b - U_1^c + U_1^d + C_{12}\right] + \frac{\Delta x_2}{2\Delta x_3}\left[U_3^a - U_3^c - U_3^e + U_3^g\right] \\
C_{30} &= \frac{\Delta x_3}{2\Delta x_1}\left[U_1^a - U_1^b - U_1^e + U_1^f\right] + \frac{\Delta x_3}{2\Delta x_2}\left[U_2^a - U_2^c - U_2^e + U_2^g + C_{23}\right]
\end{aligned}
\tag{4.8}
$$

In 2D, the interpolation and correction schemes simplify significantly by ignoring all terms associated to the 3th dimension (i.e. $x_3 = 0$ and $U_i^e = U_i^f = U_i^g = U_i^h = 0$), in which case Eq. (4.7) simplifies to the 2D incompressible scheme of *Meyer and Jenny* [2004].

Adding these corrections doesn't improve the order of accuracy of the interpolation (it remains a 2nd order accurate scheme), but they ensure a divergence-free velocity field over the cell.

4.3 Steady state flow experiments

In this section, two 2D steady state flow problems with analytical solutions are used to illustrate and test the non-conservative and conservative velocity interpolation, hereafter called n-CVI (Eq. (4.6) with $\Delta U_i = 0$) and CVI (Eq. (4.6) with $\Delta U_i \neq 0$) respectively. The flow in these problems is incompressible, so ideally, no particle convergence or divergence should occur.

4.3.1 Couette flow

The first test is a simple laminar flow of viscous fluids between two relatively moving parallel plates, known as the Couette flow. This flow is characterized with a constant shear stress throughout the flow domain, so analytical solutions for different viscosity layering are easily derived. We imposed the analytical solution of the velocity field for a Couette flow with two different viscous fluids (viscosity ratio of 10^3) in a unit model domain. The flow is at a 45-degree angle to the boundaries of the domain, as shown in Figs. 4.2a and 4.2b. To clearly illustrate the potential problem with n-CVI scheme, a very course mesh of 8×8 cells is used and an initially randomly distributed set of 10^4 particles. To provide a continuous solution in time, particles are allowed to flow into and out of the model domain at every time step.

When the n-CVI is used, a significant pattern develops in the particle distribution, since the sharply contrasting velocities of the 4 corners of any cell that lies across the two viscosity domains will result in spurious velocities inside the cell due to the imperfect interpolation (Fig. 4.2a). The particle dispersion and clustering in those cells occurs because particles in the upper part of the cell move with a much faster velocity than they should, due to the bilinear interpolation from the high velocity of the lower right node, while they will stay almost stagnant once they move to the next cell that doesn't contain any high velocity node. Fig. 4.2b illustrates that these spurious particle distribution patterns disappear when the CVI scheme is applied.

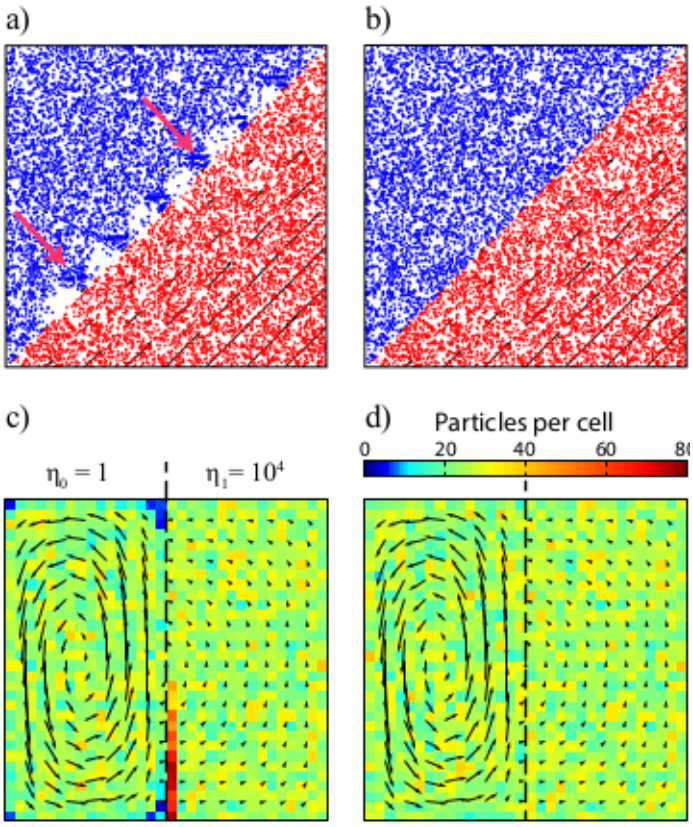

Fig. 4.2: *Particle distribution for the two steady-state cases after 5000 time steps, with black arrows showing the velocity field at the nodes. (a, b) Particle distributions obtained by a diagonal Couette flow, with red and blue areas indicating low and high viscosity, respectively. a) The velocity is interpolated with the n-CVI scheme. The dispersion (white areas) and clustering (highlight by pink arrows) of particles at the boundary between the two rheological layers is clearly visible. b) The interpolation is carried out with the CVI, in which case the particle clustering is absent. (c, d) SolCx test with the n-CVI scheme (c) and with the CVI scheme (d). The colour scale indicates the number of particles per cell. Using the n-CVI produces almost empty cells and clustering of particles at the edge of the viscosity interface, while with the CVI any clustering is virtually absent.*

4.3.2 solCx with viscosity jump of 10^4

The second test is the analytical solution for 2D incompressible Stokes flow with a sharp lateral viscosity jump, developed by *Zhong* [1996], which was later termed "solCx" [*Duretz et al.*, 2011]. Here we use a viscosity jump of 10^4 in the middle of the box. The computational domain

has a unit aspect ratio, and it is discretised by 32×32 cells. The flow is driven by an internal sinusoidal force [*Duretz et al.*, 2011], with free slip mechanical boundary conditions. The analytical solution has been used as benchmark for high viscosity contrast experiments [*Moresi et al.*, 1996; *Duretz et al.*, 2011; *Thielmann et al.*, 2014]. The source code to calculate the analytical solution is provided as part of the open source software Underworld [*Moresi et al.,* 2007].

A set of 25600 initially randomly distributed particles (~25 per cell) is advected using the analytical velocity solution at the nodes and interpolated from the nodes to the particles for every time step. As shown in Fig. 4.2c, particle clustering forms with the n-CVI within 5000 time steps advection. Particle clustering develops near the viscosity jump where the strong velocity gradient is located. Strong gradients in the velocity field (which is originally divergence-free at the cell nodes) for cells that cross the viscosity interface result in an interpolated velocity that is not divergence-free anymore, because the interpolation scheme doesn't explicit conserve the divergence (Fig. 4.2c). For the CVI scheme, the interpolation is explicitly divergence-free, and therefore particles do not cluster (Fig. 4.2d).

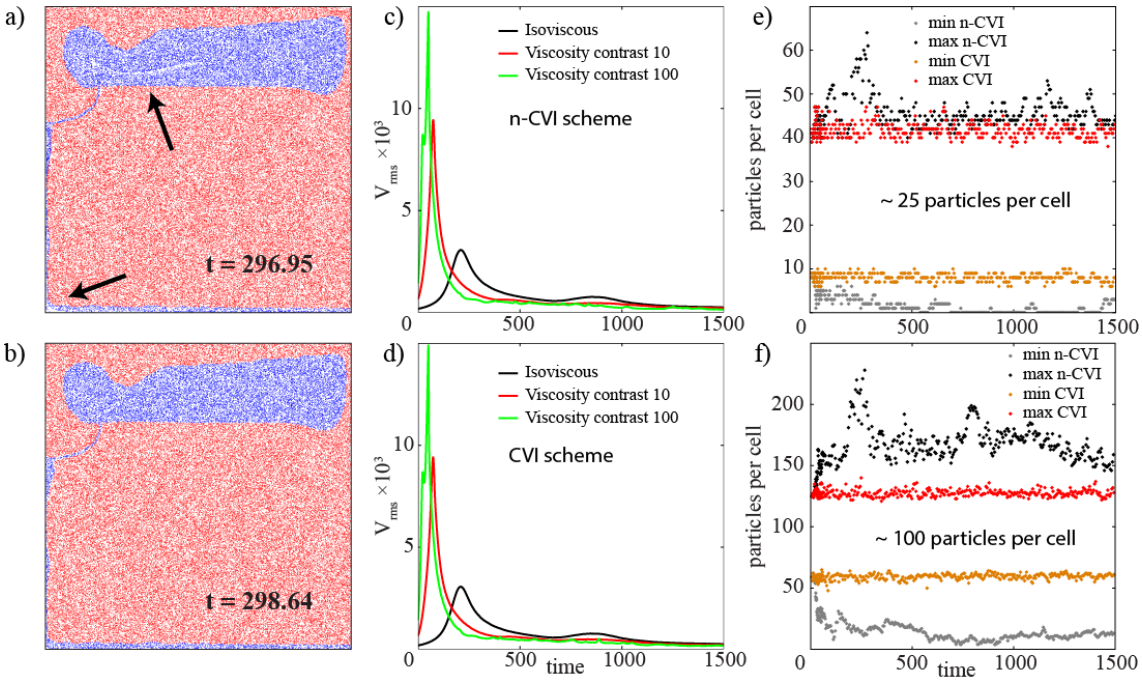

Fig. 4.3: *Rayleigh-Taylor instability benchmark test after van Keken et al. [1997]. a) and b) particles distribution for the case with a viscosity contrast of 100 (red and blue are high and low viscosity, respectively) obtained using the n-CVI (a) and CVI (b) scheme, respectively. The black arrows in a) indicate gaps in the particle distribution. c) and d) Time series of the velocity rms for three viscosity contrasts (1, 10, 100) for the n-CVI (c) and CVI scheme (d) respectively. e) and f) The maximum and minimum number of particles per cell across all cells for100 calculations for an initial particle density of ~25 particle per cell (e) and ~100 particles per cell (f).*

4.4 Time dependent flow in geodynamical applications

To illustrate the advantage of the CVI scheme for more geodynamically interesting problems, three time-dependent flow problems in which particles affect the flow field are modelled with different particle velocity interpolations in this section. We first compare our results with the standard benchmark problem from van Keken et al [1997], and then we test two types of specific geodynamic problems.

4.4.1 Rayleigh Taylor instability with a viscosity contrast.

We use a Rayleigh-Taylor instability [*van Keken et al.*, 1997] to test the bilinear interpolation for a thermochemical convection problem. This benchmark case has become a rather standard test in the geodynamical community for particle-based methods. The convection is driven by compositional density differences. The composition is advected with particles, and for the cases with viscosity contrast between the layers the viscosity is also carried by the particles. So an important difference with the previous, analytical test cases is that particles actively affect the flow field. Fig. 4.3a and 4.3b show flow results obtained for the case with viscosity contrast of 100 performed in a model domain discretised by 64×64 cells and filled with ~25 particles per cell. Fig. 4.3a illustrates the gaps in the particle distribution using the n-CVI, whereas with the CVI scheme the particles remain proportionally distributed throughout the domain (Fig. 4.3b). The interpolation method does not significantly affect the flow pattern, as shown by the time series for the root mean square velocity of the three cases demonstrated (Fig. 4.3c, 4.3d). The advantage of using the CVI scheme is more clearly illustrated in Fig. 4.3e and 4.3f where the maximum and the minimum number of particles per cell throughout the simulation are plotted. This shows how, in the n-CVI scheme, the number of particles per cell is strongly time-dependent, with some elements eventually being completely void of particles, whereas the CVI scheme maintains a statistically constant particle density everywhere.

4.4.2 2D subduction dynamics

Converging plates in subduction zones are decoupled by a thin weak layer [e.g. *Agrusta et al*., 2014] (Fig. 4.4a), and here we explore how intense shearing and local large viscosity contrasts affect the velocity interpolation for each of the interpolation schemes. The dynamics are calculated using a finite element method, in which a ~15 km thick weak (10^{20} Pa·s) decoupling layer (down to 200 km depth) between the converging plates is modelled using active particles. The model domain represents the upper mantle, with a box height of 660 km and an aspect ratio of 3, discretised into 520×127 elements. The ~$3x10^6$ particles are distributed initially randomly across the domain. The box resolution is refined vertically and horizontally to better resolve the weak layer and area at subduction trench. For a detailed description of the numerical set-up and rheological model, see [*Agrusta et al.*, 2014].

A model snapshot at 2.3 Myr (Fig. 4.4a) illustrates how the sharp viscosity contrast between the rigid plate and the weak layer generates a high velocity gradient that induces the particles to accumulate in the weak layer and leaves voids above it with the n-CVI scheme (Fig. 4.4a, left panel), whereas the CVI scheme prevents this behaviour (Fig. 4.4a, right panel). This particle behaviour is very similar to the Couette flow illustrated above.

4.4.3 3D lithosphere dynamics

Another example of a geodynamical scenario in which particle distribution can be significantly affected is the long-term interaction between the base of the lithosphere and the convecting mantle. Here we test the CVI scheme on a 3D model of a very viscous cratonic root in a much weaker thermochemically convecting mantle that has often been studied in 2D situations [*Lenardic et al.*, 2003; *O'Neill et al.*, 2008; *Wang et al.*, 2014]. The computational domain is 660 km deep with a unit aspect ratio. To represent a buoyant craton, a half-sphere, compositionally different from the surrounding mantle is situated at the top of the cube (Figs. 4.4b-e). The viscosity contrast between the half-sphere cratonic root and the mantle is 10^3. The initial internal temperature field is 1350^{o}C everywhere. T=0 and T=1350^{o}C are imposed on the surface and bottom, respectively, with zero heat flux on the sides and with free-slip mechanical boundary conditions everywhere. We use a coarse mesh resolution of 33×33×33 cells with 10^6 particles. Fig. 4.4b shows the temperature field after a dimensionless time of 1200. The particle distribution in cross-section slices of one cell width, projected in a cross section, show the particle distribution with the n-CVI and CVI schemes in Fig. 4.4c and 4.4d, respectively. Similar to the 2D calculations, the trilinear n-CVI induces particle clustering near the compositional boundary (Fig. 4.4c), whereas the 3D CVI scheme maintains a homogenous particle distribution (Fig. 4.4d). With the n-CVI, the minimum particle number reaches zero quickly and remains small afterwards; the maximum particle number keeps increasing steadily, which illustrates the ongoing clustering of particles. In contrast, the minimum and maximum particle count per cell stays between 10 and 55 with the CVI scheme, which illustrates again a persistently homogenous particle distribution through time (Fig. 4.4e).

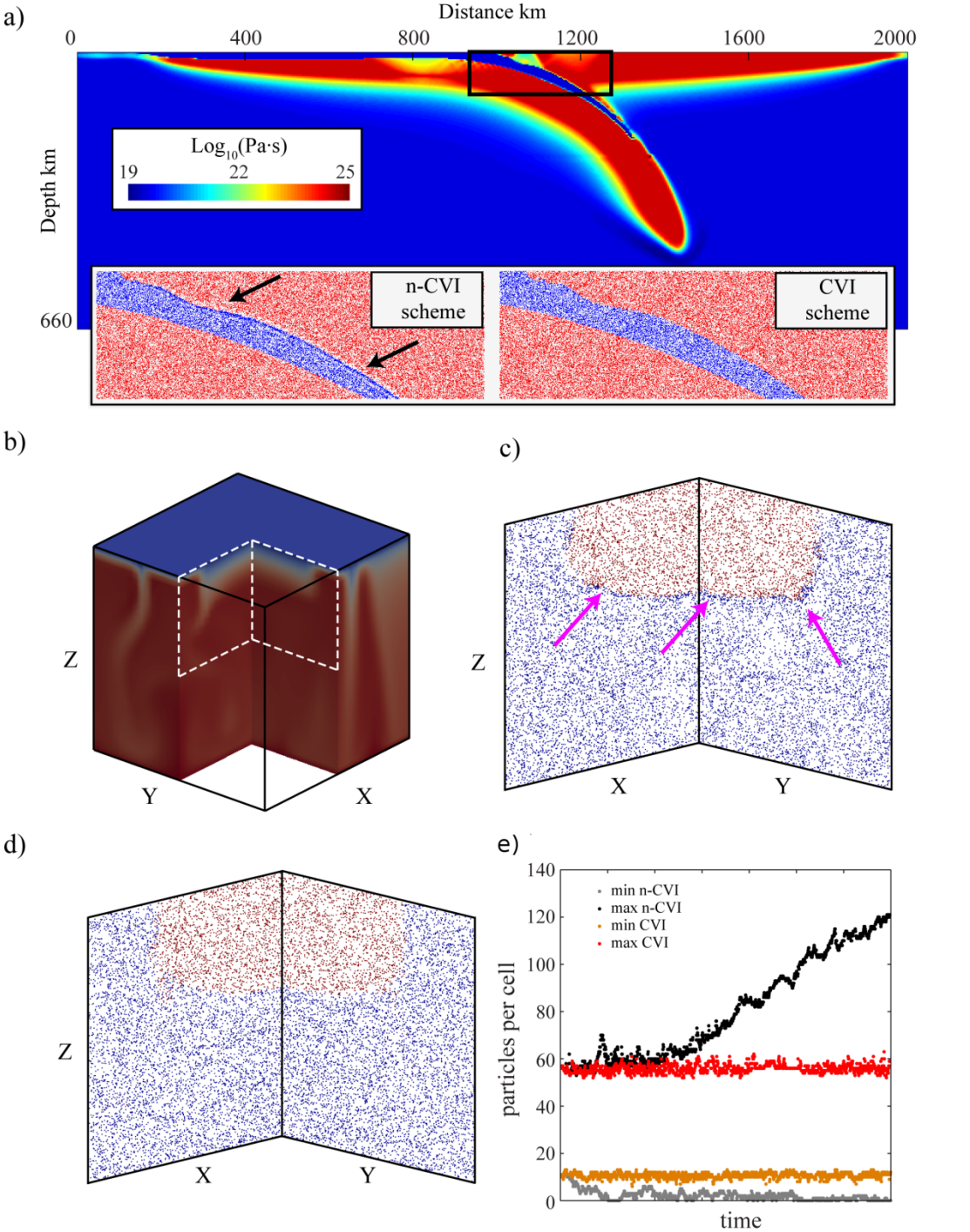

Fig.4.4: *Two examples on the effect of the different velocity interpolation schemes for geodynamically relevant scenarios in 2D and 3D. a) Particle distribution around a weak layer that decouples converging plates in a subduction zone. Particle clustering develops at the interface between the weak layer and the overriding plate by using the n-CVI scheme (bottom left inset), whereas particles remain evenly distributed by using the CVI scheme (bottom right inset). b) Temperature field near an idealised buoyant craton in a 3D scenario, with particle distributions obtained with the n-CVI (c) and CVI (d) scheme. The arrows point towards occurrences of particle clustering. e) Time series of the maximum and minimum number of particles per element for each of the two interpolation schemes in the 3D craton model.*

4.5 Discussion and conclusion

In this study, we reported a solution for a commonly observed problem in geodynamic modelling related to the PIC method. Using the analytical solution of two steady-state flow problems, we demonstrate that the commonly observed clustering and dispersion of particles in a PIC method is insensitive to numerical discretisation techniques or particle advection methods, but instead is caused by the non-conservative interpolation method of the velocity field from the cell nodes to the particles. The conservative velocity interpolation (CVI) proposed in this study solves this problem for incompressible flow by ensuring a divergence-free velocity field for the particles. We illustrate that this method works very well for both steady-state flow problems and geodynamically more complex and relevant time-dependent flow problems.

4.5.1 Numerical advantage and wider applicability

Maintaining a certain minimum particle density in every computation cell is important for the success of PIC methods [*van Keken et al.*, 1997; *Tackley and King*, 2003]. However, significant clustering and dispersion of particles commonly occurs in the presence of strong velocity gradients, e.g. due to locally high viscosity contrasts. Using a very high particle density might help to avoid significant gaps in the particle distribution but not always, and such remedy quickly becomes computationally expensive, especially in 3D models. Reseeding particles to the areas approaching low particle density may appear to solve the problem, but doesn't have solid physical base. Our results show how the particle distribution problem can easily be solved by using a conservative velocity interpolation (i.e. divergence-free interpolation for incompressible flow) from cell nodes to particles. This method has the advantage that the divergence property of the velocity field is maintained [*Jenny et al.*, 2001; *Meyer and Jenny*, 2004], which is physically reasonable. The proposed solution is very easily implemented and requires negligibly higher computational costs.

The presented new interpolation scheme has been applied to 4-node quadrilateral cells in a divergence-free flow field (i.e. incompressible flow), for which the proposed solution is very easily implemented. But the advantages of a conservative interpolation should apply more generally to compressible flow problems [Jenny et al., 2001] and more complex meshing techniques. However, some modifications are required to apply this scheme to more complex meshing techniques. For example, staggered grids are commonly used in finite difference and finite volume methods (e.g. Gerya and Yuen [2003b]), and have different node locations for the different velocity components. Therefore, an adapted implementation of the CVI scheme is required for more complex grid configurations, which will be the topic of future investigation.

4.5.2 Geodynamic application

With the arrival of new numerical techniques and increased computational capacity, the geodynamical modelling of chemical heterogeneity has become more and more prominent [e.g. *Gerya and Yuen*, 2003a; *McNamara and Zhong*, 2004; *Tackley*, 2008]. Examples include varying mineral compositions, or volatile content, which can have a substantial effect on the rheology of the crust and mantle [*Hirth and Kohlstedt*, 1996; *Karato*, 2006; *Keefner et al.*, 2011]. These slow or non-diffusive properties can create and maintain sharp local viscosity contrasts and strong velocity gradients. Here we show how, in such scenarios, non-conservative velocity interpolation such as the bilinear/trilinear scheme could lead to significant clustering and dispersion of particles. The 2D and 3D conservative velocity interpolation (CVI) schemes presented in this study provides a simple, effective way to improve the PIC method for the incompressible flow problems under this situation. CVI is a physically correct interpolation scheme that is easily implemented and maintains statistically constant particle densities, thereby avoiding particle dispersion and locally decreasing particle densities over time. Initial particle densities can therefore be relatively low, which improves the computation efficiency, especially for 3D calculations.

The presented new interpolation scheme has been applied to 4-node quadrilateral cells in a divergence-free flow field (i.e. incompressible flow), but the advantages of a conservative interpolation should apply more generally to compressible flow problems [*Jenny et al.*, 2001] and other meshing technique. However, further additional work might be required to apply such schemes to other meshing technique. For example, the commonly used staggered grid (e.g. Gerya and Yuan [2003b]) have different node points for different velocity components, which probably lead completely different implementation of the conservative or divergence-free interpolation. The derivation of the CVI scheme for a staggered grid and other meshing technique is beyond the scope of this paper. For more general flow problem, including 3D compressible flow, conservative interpolation can be achieved through more mathmatically advanced methods such as Galerkin projection of a discrete field [*Farrell and Maddison*, 2011]. However, the level of improvement and necessity to use a conservative velocity interpolation scheme depends on the geodynamical application

Acknowledgments

The work has been supported by EU FP7 Marie Curie Initial Training Network ‘Topomod’, contract No. 264517 (HW). RA acknowledges funding from NERC (grant NE/J008028/1) and JvH was funded by the European Research Council (ERC StG 279828). The authors would like to thank Henri Samuel, Antoine Rozel and Lara Kalnins for useful discussions. The data for this paper are available by contacting the corresponding author.

Chapter5

Craton stability and longevity: the roles of composition-dependent rheology and buoyancy[2]

Abstract

Survival of thick cratonic roots in a vigorously convecting mantle system for billions of years has long been studied by the geodynamical community. High strength of the cratonic root is generally considered to be the most important factor, but the role of lithospheric mantle depletion and dehydration in this strengthening is still debated. Geodynamical models often argue for a significant strength or buoyancy contrast between cratonic and non-cratonic mantle lithosphere, induced by mantle depletion and dehydration. But recent laboratory experiments argue for only a modest effect of dehydration strengthening. Can we reconcile laboratory experiments and geodynamical models?

We perform and discuss new numerical models to investigate craton stability and longevity with different composition-dependent rheology and buoyancy. Our results show that highly viscous and possibly buoyant cratonic root is essential to stabilise a geometry in which thick cratonic lithosphere and thinner non-cratonic lithosphere coexist for billions of years. Using non-Newtonian rheology, a modest strengthening factor of $\Delta\eta=3$ can protect compositionally buoyant cratonic roots from erosion by mantle convection for over billions of years. A larger strengthening factor ($\Delta\eta=10$) can maintain long term craton stability even with little or no intrinsic buoyancy. Such composition-dependent rheology is comparable to the laboratory experiments. This implies that a strict isopycnic state of cratonic lithosphere may not be necessary for the preservation of a cratonic root, provided a sufficient level of compositional strengthening is present.

[2] This Chapter has been previously published as "Wang, H.L., van Hunen, J., Pearson, D.G. & Allen, M.B. (2014). Craton stability and longevity: The roles of composition-dependent rheology and buoyancy. Earth and Planetary Science Letters 391: 224-233". All model development and results were performed and the manuscript written by H. Wang. The co-authors have participated in this study by providing training, feedback on the manuscript, and useful discussions.

5.1 Introduction

Cratons – the most ancient parts of the continents, are characterized by their old crust and thick lithosphere. Most cratonic lithosphere (e.g. that beneath the Kaapvaal, Siberia and Slave cratons) has a thickness up to 200-250 km [*Boyd*, 1973; *Boyd et al.*, 1997; *Gung et al.*, 2003; *Mather et al.*, 2011], although some cratons have been subjected to recent thinning events, e.g. the North China Craton and Wyoming craton [*Fan and Menzies*, 1992; *Goes et al.*, 2002; *Gao et al.*, 2008]. While the oceanic plates recycle into the mantle within about 200 Myrs, cratons are found to be covered by Archean crust. Furthermore, geochemical evidence, predominantly from diamond inclusion dating and Re-Os isotopes, suggests that the age of cratonic lithosphere is broadly similar to its crust, at least to the extent that Archean mantle lithosphere generally underlies Archean crust [*Richardson et al.*, 1984; *Pearson*, 1999]. Hence, it is clear that the present cratonic lithosphere had a thick cratonic keel and survived erosion by mantle convection for billions of years.

While the evidence for the long-term stability of deep cratonic lithosphere is clear, our understanding of all the parameters that contribute to this stability remains relatively poor and conflicting. The longevity and stability of cratons has been attributed to either external factors such as weak mobile belts surrounding cratons, or internal factors such as the intrinsic buoyancy and high strength of the cratonic root [*Carlson et al.*, 2005]. Mobile belts surrounding a craton may shield it from plate-tectonic related stresses and erosion, and can increase its stability significantly [*Lenardic et al.*, 2000, 2003; *Yoshida*, 2010, 2012; *Yoshida and Santosh*, 2011]. But for more continuous thermal erosion by the convecting mantle within the asthenosphere, the effects of peripheral mobile belts appear to be limited. This process, known as entrainment of cratonic material [*Sleep*, 2003] by the lateral and sublithospheric small scale convection, is driven by the lateral and vertical density contrasts surrounding the cratonic root [*Doin et al.*, 1997; *Shapiro et al.*, 1999; *Solomatov and Moresi*, 2000]. Hence, the role of compositionally distinct cratonic root needs to be investigated. Chemical buoyancy promotes resistance to thermal erosion and improves the stability of cratons, but has been suggested to be insufficient to ensure craton longevity by itself [*Doin et al.*, 1997; *Lenardic and Moresi*, 1999; *O'Neill et al.*, 2008; *François et al.*, 2012]. Thus, "physical protection" from both mobile belts and chemical buoyancy does not appear to be sufficient to explain why the cratonic root has survived in a convecting mantle for billions of years.

Lenardic et al. [2003] proposed that a thick chemically distinct root with more than twice the thickness of typical oceanic lithosphere is required for long term craton stability even if a very viscous cratonic root (1000 times more viscous) is employed. They further argued that the high brittle yield strength for cratonic lithosphere is a more effective and robust way to provide craton stability over several mantle overturn times. *O'Neill et al.* [2008] updated this conclusion by demonstrating that long term craton stability can be provided by a compositional viscosity

ratio of 50 to 150, with a root /oceanic lithosphere yield strength ratio of 5-30. Based on a scaling research, *Sleep* [2003] indicates that a viscosity factor of 20 with weakly temperature dependent viscosity is needed for survival of cratonic lithosphere. Furthermore, *Beuchert et al.* [2010] argued that thermal craton stability in stagnant lid approach for billions years could be provided by sufficiently high temperature-dependent viscosity contrast (10^7 to 10^{10}) even without invoking any compositional difference. While it is well known from petrological studies that the cratonic lithosphere is compositionally distinct from oceanic lithospheric mantle and even post-Archean continental lithospheric mantle [*Boyd*, 1989; *Pearson and Wittig*, 2008], the conflicting modelling results show that it remains far from clear to what extent composition-dependent rheology is required. Also, because any mechanism for creating lithosphere creates strong compositional stratification, it is important to explore the role played by a composition-dependent rheology and buoyancy.

The need to further explore the effect of composition-dependent rheology on lithosphere stability is also driven by results from laboratory rheological experiments. Volatiles, especially water are supposed to be among the dominant influences on mantle rheology [*Mei and Kohlstedt*, 2000a, 2000b; *Karato*, 2006; *Keefner et al.*, 2011]. The dehydration of cratonic roots due to their exceptional melt depletion has long been proposed to contribute to the high strength of cratonic lithosphere [*Hirth et al.*, 2000; *Carlson et al.*, 2005; *Peslier et al.*, 2010]. But the effects of water on mantle rheology in laboratory experiments vary considerably between different experiments [*Hirth and Kohlstedt*, 1996; *Mei and Kohlstedt*, 2000a, 2000b; *Karato*, 2006; *Fei et al.*, 2013]. *Hirth and Kohlstedt* [1996] found the viscosity of water-saturated olivine aggregates is reduced by a factor of 100~180 at a confining pressure of 300 MPa (where the solubility of water is ~15.3wt ppm or 250H/10^6Si). *Karato* [2010] proposed viscosity changes up to 4 orders of magnitude for a constant stress at depths of 200-400 km due to the influence of water. In contrast, a recent study of the silicon self-diffusion coefficient in forsterite suggests that the effect of water on upper mantle rheology is only up to one order of magnitude [*Fei et al.*, 2013] .

The role of different deformation mechanisms in the upper mantle might also need further investigation. Most of the previous numerical research on craton stability used a Newtonian rheology for mantle deformation. *François et al.* (2012) used non-Newtonian rheology but without any compositional dependency. Mantle rheology laboratory studies suggest that the dominant creep mechanism in upper mantle is dislocation creep, even though diffusion creep (grain-size sensitive) may operate in some conditions [*Karato*, 2010]. This point has also been supported by geodynamical modelling and measurements of seismic anisotropy of upper mantle [*Mainprice et al.*, 2005; *van Hunen et al.*, 2005; *van Hunen and Čadek*, 2009]. Diffusion creep, usually taken as Newtonian rheology in numerical modelling, could turn into non-Newtonian rheology if the grain-size dependence is not ignored and influence the mantle flow pattern sub-

stantially [*Rozel*, 2012]. Although Newtonian rheology is proved to be able to mimic non-Newtonian rheology with an equivalent activation energy [*Christensen*, 1984], it may fail to capture some important characteristics of mantle convection (e.g. *Asaadi et al.,* 2011).

Given the significant variation in results from both geodynamical modelling and laboratory rheological experiments, further investigation in the effects of compositional rheology and buoyancy due to mantle dehydration and depletion on craton stability is warranted. Here, we present numerical modelling results on the effects of compositional rheology and buoyancy on the stability of cratonic roots. We aim to determine how viscous or buoyant cratonic roots need to be to ensure craton stability and longevity over Gyr timescales using both non-Newtonian and Newtonian rheology.

5.2 Model description

5.2.1 Governing equations

A Cartesian version of the finite element code Citcom is used in our numerical simulation [*Moresi and Solomatov*, 1995; *Zhong et al.*, 2000; *van Hunen and Allen*, 2011], which solves the incompressible flow using the Boussinesq approximations. The non-dimensional governing equations of conservation of mass, momentum, energy are:

$$\nabla \cdot \mathbf{u} = 0 \tag{5.1}$$

$$-\nabla P + \nabla \left(\eta \left(\nabla \mathbf{u} + \nabla^{\mathrm{T}} \mathbf{u}\right)\right) + \left(RaT - Rb_i C_i\right) e_z = 0 \tag{5.2}$$

$$\frac{\partial T}{\partial t} + \mathbf{u} \cdot \nabla T = \nabla^2 T + Q_0 \tag{5.3}$$

A standard non-dimensionalisation is applied, with $x = x'h,\ t = t'h^2/\kappa,\ \eta = \eta'\eta_0$. The primes of the non-dimensional parameters are dropped in the equations above for clarity. Their dimensional counterparts are defined in Table 5.1. Different chemical fields are used to track different material (C_1 for upper crust and lower crust; C_2 for depleted mantle and fertile mantle), which are advected with the flow through the equation:

$$\frac{\partial C_i}{\partial t} + \mathbf{u} \cdot \nabla C_i = 0 \tag{5.4}$$

where C_i is calculated from the distribution of tracers. Eq. (5.4) is solved by a particle-tracking technique [*van Hunen et al.*, 2000; *Ballmer et al.*, 2007], in which the tracers, that carry the information about density and rheology, are advected with the velocity field from Eq. (5.1) and (5.2). This method has been benchmarked against *van Keken et al.* [1997] and *Schmeling et al.* [2008]. One tracer function is used to track crustal material (including upper and lower crust), while another tracks different depletion of mantle material (fertile mantle, highly depleted, and less depleted cratonic root material) (Fig. 5.1).

Table 5.1 Symbols, units and default parameters.

Symbol	Description	Default value and units
A	rheological pre-exponent	$[MPa^{-n}s^{-1}]$ (ds), $[MPa^{-1}]$ (df)
E	activation energy	500 (ds), 310 (df) [kJ/mol]
V	activation volume	$[cm^3/mol]$
g	gravitational acceleration	9.8 $[m/s^2]$
h	model height	660 [km]
C_p	Thermal capacity	1250 $[J\ kg^{-1}K^{-1}]$
n	rheological power law exponent	3.5 (ds), 1 (df) [-]
P	deviatoric pressure	[Pa]
R	gas constant	8.3 [J/mol]
Ra	thermal Rayleigh number	$4.43x10^6$ [-]
Rb[a]	compositional Rayleigh number	$1.69x10^7$, $1.97x10^6$ [-]
T	Temperature	$[^0C]$
ΔT	temperature drop over model domain	1350 $[^0C]$
$\dot{\varepsilon}$	strain rate	$[S^{-1}]$
α	thermal expansion coefficient	$3.5x10^{-5}$ $[K^{-1}]$
η_0	reference viscosity	10^{20} [Pa·s]
η	Viscosity	[Pa·s]
κ	thermal diffusivity	10^{-6} $[m^2/s]$
ρ	mantle density	3300 $[kg/m^3]$
$\Delta\rho_1$	density difference of upper crust and mantle	600 $[kg/m^3]$
$\Delta\rho_2$	maximum density change due to depletion	70 $[kg/m^3]$
Q_0	radioactive heating	0.04 $[\mu W/m^3]$
C_i	composition field	0~1 [-]
$C\eta$[b]	rheologically effective composition value	0.6 [-]

[a] $1.69x10^7$ and $1.97x10^6$ are the compositional Rayleigh numbers for crust and cratonic root, respectively.

[b] $C\eta$ is chosen to make the second cratonic layer has the maximum strengthening factor due to its initial compositional field.

The thermal Rayleigh number Ra and compositional Rayleigh number Rb are defined as:

$$Ra = \frac{\alpha \rho_0 g \Delta T h^3}{\kappa \eta_0} \quad (5.5)$$

$$Rb_i = \frac{\delta \rho_i g h^3}{\kappa \eta_0} \quad (5.6)$$

The description of parameters in Eqs. (5.5)-(5.6) is listed in Table 5.1. The Rayleigh numbers given in the table are calculated by using relatively high reference viscosity η_0. The viscosity of asthenosphere is, however, significantly lower (e.g. Fig. 5.2).

5.2.2 Model setup

Our models extend to 660 km in depth and 2640 km in horizontal width, with a 660 km-wide craton positioned in the middle of the model domain (Fig. 5.1). In order to deal with locally sharp and large viscosity contrast, a resolution of 192-by-96 finite elements is used, with mesh refinement in the cratonic root area. This provides the vertical resolution is 4.7 km around the cratonic root area and 8-9 km in the circum-cratonic regions. 640000 tracers were used in the model, which provides an average tracer density of about 35 tracers per finite element.The velocity boundary conditions used in the models are free slip at the surface and side boundaries, and no-slip at the bottom. Half space cooling models are used to define the initial thermal structure of cratonic lithosphere (400 Myrs in most cases) and normal lithosphere (150 Myrs). Temperature is fixed at the surface (T=0^{o}C) and bottom (T_b=1485^{o}C in most cases), while side boundaries are insulating. This setup leads to a mantle potential temperature around 1350 ^{o}C in asthenosphere after the thermal boundary layers form at bottom in our models. In order to monitor the thickness changes of the lithosphere, we define a thermal lithosphere asthenosphere boundary (LAB) by the isotherm of T=1215°C and calculate the average thicknesses of cratonic and non-cratonic lithosphere through time. The selection of rheological parameters in most models (all except N11 and N12) is based on the assumption that non-cratonic lithosphere should have a thickness of about 140 km. This value is a reasonable average for Phanerozoic and Neoproterozoic lithosphere, i.e. lithosphere younger than ~1 Ga (Artemieva, 2011). These rheological parameters also result in a reasonable viscosity at asthenosphere between 10^{18} Pa·s and 10^{19}Pa·s that is constant with the value suggested by *Solomatov and Moresi* [2000].

A two- layer cratonic keel model (modified from Afonso et al. (2008)'s three-layer model) was used: a highly depleted layer (with C=1) from 36 km (Moho) to 144 km depth and a less depleted layer (C=0.6) from 144 km to 234 km depth. We assume the density reduction to be proportional to C, with the most depleted lithosphere 2.1% (70 kg/m^3) less dense than fertile lithosphere, which is within the range of density reduction (1.5% ~2.5%) due to a bulk Mg number change from fertile mantle (e.g.Mg# = 88) to depleted cratonic root (Mg# = 92 -

94)(Pearson and Wittig, 2008). The density of crust and the depleted cratonic root is described by:

$$\rho_c = \rho_m - C_i \Delta \rho_i \tag{5.7}$$

All models have a buoyant crust composed of 18 km upper crust and 18 km lower crust, which are 600 kg/m^3 and 400 kg/m^3 less dense than the normal mantle, respectively. However, we found that, the effect of this crust density contrast on the dynamics of the convection system is minor. We ignore the difference in radioactive heating between crust and mantle and their decay over the long-term history of the Earth, but use a uniform, equivalent value of Q_0= 0.04 μW/m^3, which is roughly twice the value of modern, undepleted mantle as an average for the past 2 Ga. This simplified heat production model allows us to investigate the statistically steady-state situation, and therefore gain a more fundamental understanding of the dominant processes.

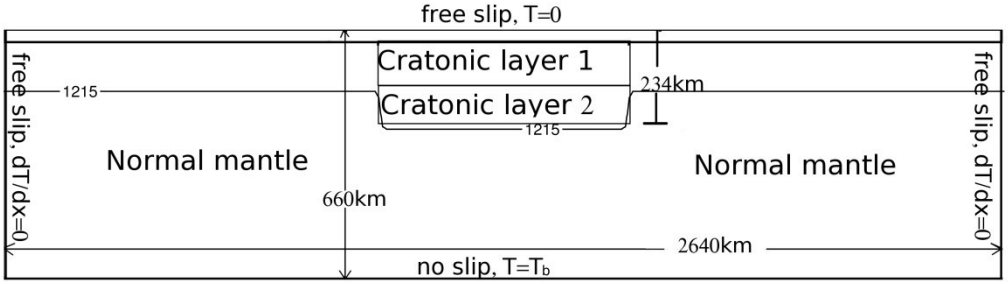

Fig. 5.1: *Model setup, including initial material setup, mechanical and thermal boundary conditions. The model extends to 660km depth and has a 1:4 aspect ratio. The material setup includes: a 36km crust on the surface, two cratonic layers in the middle of the model domain (extends to 234km depth); normal mantle elsewhere. The first and second cratonic layers are 70kg/m^3 and 42kg/m^3 less dense than the normal mantle, respectively. Half space cooling models are used to define the initial thermal structure of cratonic lithosphere (400 Myrs unless mentioned otherwise) and normal lithosphere (150 Myrs). The curve in the domain indicate the isotherm of and 1215^{0}C.*

5.2.3 Rheology

As this study focuses on the role played by the rheology of cratonic root, we ignore any rheological differences made by the crust to simplify the model setup. The effective viscosity in our models is described by:

$$\eta_m = A^{-\frac{1}{n}} \dot{\varepsilon}^{\frac{1-n}{n}} \exp\left(\frac{E + \rho g z V}{nRT}\right) \tag{5.8}$$

with n=3.5 for non-Newtonian rheology (i.e. dislocation creep) and n=1 for Newtonian rheology (i.e. diffusion creep). Our non-Newtonian rheology has been benchmarked against results of Christensen (1984). The descriptions and default values of the parameters in Eq. (5.8) are listed in Table 5.1.

In order to study the effects of composition-dependent rheology of cratonic root, a strengthening factor Δη is used. As a result, the effective viscosity of cratonic root is dependent on the depletion, and given by:

$$\eta_C = \eta_m \times \Delta\eta^{\min(1, \frac{C_2}{C_\eta})} \quad (5.9)$$

Combined with Eq. (5.8), Eq. (5.9) defines a composition-dependent rheology in which the effective viscosity of cratonic root is $\Delta\eta$ times of normal mantle at constant strain rate. This is equivalent to a viscosity contrast $\Delta\eta^n$ if the constant-stress definition of effective viscosity is used for non-Newtonian rheology. A maximum model viscosity cut-off was set up to 10^{25} Pa s in most models, but tests with10^{26} Pa s and 10^{27} Pa s were done to assure that higher viscosity cut-off would not affect the results.

5.3 Results

To investigate cratonic stability under a range of circumstances, numerical model calculations were performed with different rheology and buoyancy settings (Table 5.2). We define a successful model for craton preservation using the following two criteria: 1) the cratonic root survives erosion via mantle convection and preserves a thickness in excess of 200 km for 2 Gyrs; 2) over the same period, non-cratonic lithosphere maintains a reasonable thickness of ~140±10 km To illustrate the dominant geodynamical features in those models, we start with the description of a reference model.

5.3.1 Reference model

Our reference model uses the two-layered cratonic root and non-Newtonian rheology with a compositional rheological factor $\Delta\eta$=10 (Eq. (5.9)). Fig.5.2 shows the evolutions of temperature, cratonic root shape and viscosity for the duration of 2 Gyrs. The main part of the cratonic root is stable, with only limited erosion at its edges. There is a viscosity contrast of about 3 to 4 orders magnitude between the cratonic root and asthenosphere (Fig.5.2). Hence, due to the combined non-Newtonian and temperature dependent effect, the compositional rheological factor Δη=10 results in sufficient viscosity at the cratonic root to resist significant erosion from the underlying convecting mantle.

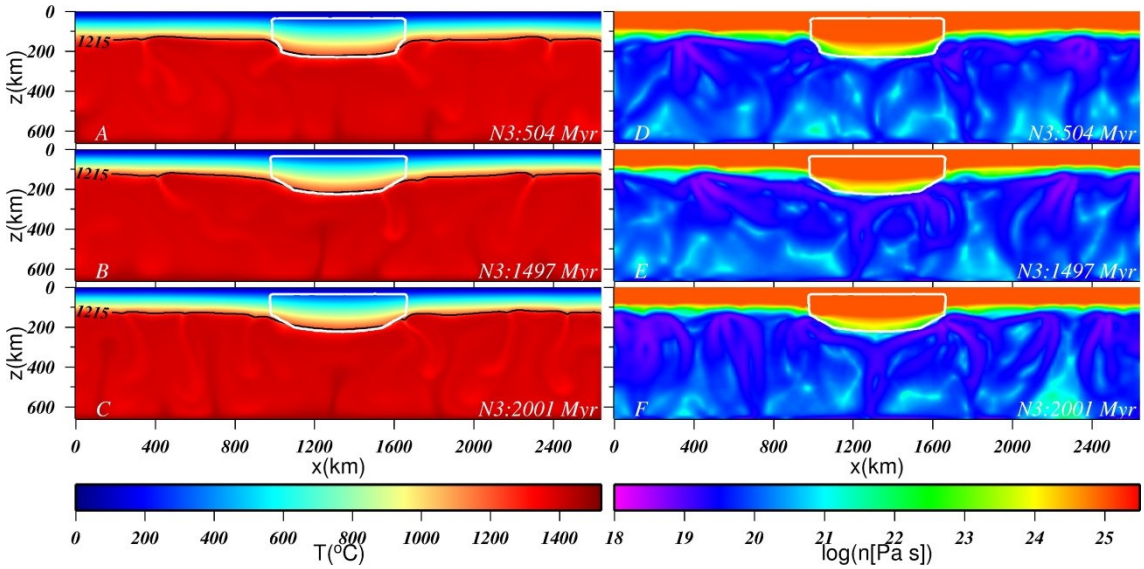

Fig. 5.2: *Thermal (a,b,c) and rheological (d,e,f) evolution of the reference model N3 for a model time of 0.5 Gyrs after the start of the model calculation (a,d), 1.5 Gyrs (b,e), and 2.0 Gyrs (c,f). The white contour outlines the compositionally different cratonic root. The isotherm of T=1215°C is plotted in the temperature image to represent the lithosphere asthenosphere boundary (LAB). The reference model shows cratonic root has been well preserved through about 2 Gyrs.*

The thickness changes of cratonic lithosphere and non-cratonic lithosphere are monitored through time by using the T=1215°C isotherm as the LAB. The results are plotted as the red lines in Fig.5.3A, with thick and thin lines represent cratonic and non-cratonic lithosphere respectively. In this model, the thicknesses of cratonic and non-cratonic lithosphere are maintained as 210 km and 140 km respectively.

5.3.2 Compositional rheology

Fig.5.3A shows four numerical experiments performed with different strengthening factors Δη in terms of thickness evolution of cratonic and non-cratonic lithosphere, including reference model N3. All of the other three models have the same initial buoyant cratonic root setting as in the reference model. Without any compositional rheology (model N1, $\Delta\eta$ =1), the thickness of cratonic lithosphere decreases slowly with time (Fig. 5.3A), and cratonic root almost disappears over 1.2 Gyrs (Fig.5.4A). This means that just starting with a buoyant and cold cratonic keel (and therefore stronger than the surroundings) is not sufficient to preserve a craton from long term heating and erosion. An even higher strengthening factor (model N4, $\Delta\eta$=30) restricts the erosion of cratonic lithosphere only marginally more than the default $\Delta\eta$ =10 (Fig.5.3A). Comparably, a smaller strengthening factor (N2, $\Delta\eta$ =3) may also maintain the thick cratonic root for billions of years (Fig. 5.3A), but the lowermost cratonic root is stretched significantly (Fig.5.4B).

Table 5. 2 Comparison of parameters in all models.

Model	Δη	Buoyancy	V[cm^3/mol]	A	T_b^e [^{0}C]
N1	1	Y	5	$2.32x10^5$	1485
N2	3	Y	5	$2.32x10^5$	1485
N3	10	Y	5	$2.32x10^5$	1485
N4	30	Y	5	$2.32x10^5$	1485
N5	1	N	5	$2.32x10^5$	1485
N6	3	N	5	$2.32x10^5$	1485
N7	10	N	5	$2.32x10^5$	1485
N8	30	N	5	$2.32x10^5$	1485
N9	10	Y	10	$5x10^6$	1512
N10	10	Y	15	$8x10^7$	1552.5
N11[a]	10	Y	5	$2.32x10^5$	1485
N12[b]	10	Y	5	$2.32x10^5$	1485
N13	10	Y	5	$2.32x10^6$	1485
N14[c]	10	Y	5	$2.32x10^5$	1485
L1[d]	10	Y	2.5	$6.5x10^{-3}$	1485
L2	100	Y	2.5	$6.5x10^{-3}$	1485

[a] Compared with reference model N3, maximum viscosity cut-off is changed from 10^{25} to 10^{24} Pa·s.

[b] Compared with reference model N3, maximum viscosity cut-off is changed from 10^{25} to 10^{26} Pa·s.

[c] Radioactive heating is changed from 0.04uW/m^3 to 0.06uW/m^3.

[d] Model L1 and L2 use Newtonian rheology with activation energy of E 310kJ/mol, while other models use non-Newtonian rheology with V=500kJ/mol (Table 5.1).

[e] Tb is selected so that the internal mantle temperature would be around 1350^{0}C in our model.

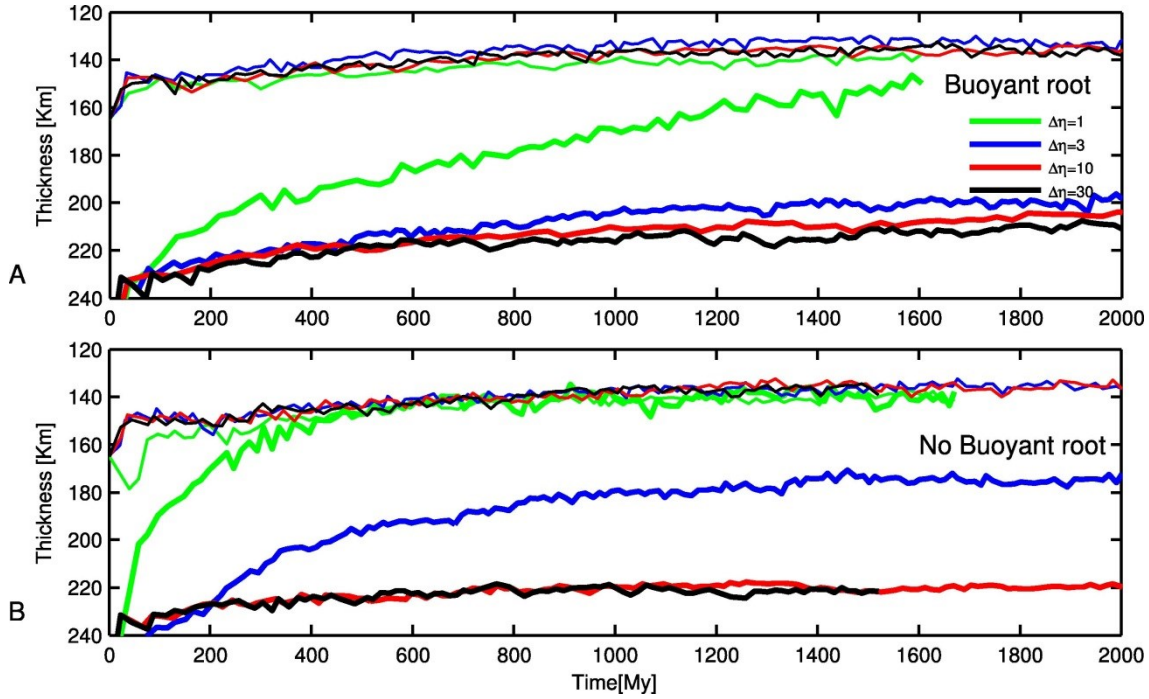

Fig. 5.3: *Thickness evolutions of cratonic (thick lines) and non-cratonic lithosphere (thin lines) for models with non-Newtonian rheology over a time period of 2000 Myrs. The red lines represent the reference model N3, while green, blue and black lines represent models with strengthening factor of 1(model N1),3(model N2) and 30 (Model N4) . Fig.5.3B shows models without extra buoyancy of the cratonic root (model N5,N6, N7, N8), compared with models in 5.3A.*

From Fig. 5.3A, an estimate of the thinning rate of cratonic lithosphere is calculated through polynomial fitting. Models with composition-dependent rheology show a substantial reduced thinning rate compared to model N1. The thinning rate in the reference model N3 ($\Delta\eta$ =10) decreases from ~30km/Gyrs in the beginning to ~2km/Gyrs at 2 Gyr, which makes a well-preserved craton. The thinning rate in model N1 ($\Delta\eta$ =1) also decreases with time, but it start at ~80km/Gyrs and maintain a rate of ~20km/Gyr at 1.5Gyr, which precludes the longevity of thick cratonic lithosphere. This shows that a strong cratonic root is essential to resist the long-term erosion from the convecting mantle.

Another 4 similar experiments were performed but without compositional buoyancy in the cratonic roots (Figs.5.3B, 5.4C, 5.4D). Despite the absence of compositional buoyancy, the cratonic lithosphere is still well preserved with $\Delta\eta$ =10 in model N7, and keeps a thickness well beyond 200 km throughout the entire 2 Gyrs model calculation (Fig.5.3B, 5.4D). Again, the difference between $\Delta\eta$ =30 (model N8) and $\Delta\eta$ =10 (model N7) is statistically insignificant. Thus, no higher strengthening factor than $\Delta\eta$ =10 is required even if the cratonic root is not compositionally buoyant.

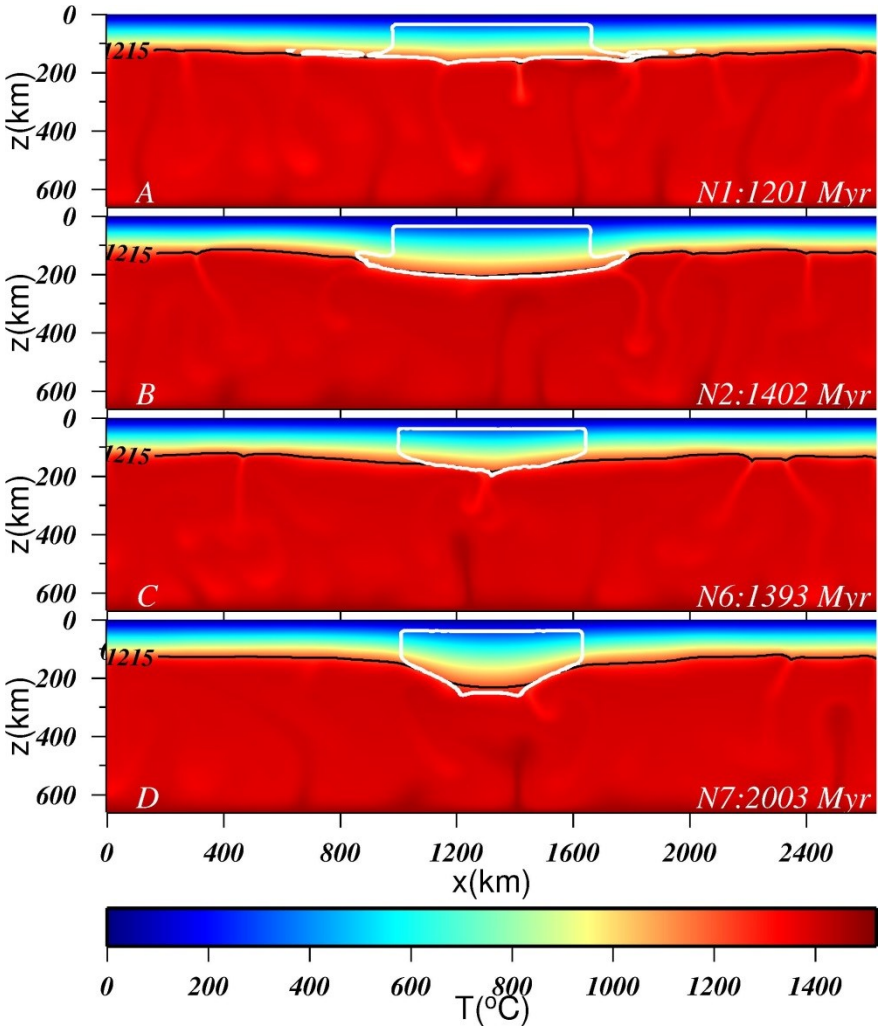

Fig. 5.4: *The temperature field and cratonic root (white box) of model N1at 1.2 Gyr (A), N2 at 1.4 Gyr (B), N6 at 1.4 Gyr (C) and N7 at 2 Gyr (D) from the model start time. Compositional buoyancy of cratonic root delays the erosion process in model N1 (A) compared with model N5. Model N7 has a different shape of cratonic root with the reference model N3, which indicates that compositional buoyancy of cratonic root might have an important effect on the long term deformation of cratonic lithosphere.*

5.3.3 Compositional buoyancy

The effects of compositional buoyancy are investigated by the comparison between models with and without buoyant cratonic roots (model N1-N4 in Fig.5.3A versus N5-N8 in Fig.5.3B). Model N5 shows that the cratonic lithosphere would be eroded away rapidly within 400 Myrs (Fig.5.3B) if the compositional buoyancy is removed from model N1. Model N6 demonstrates that the smaller strengthening factor ($\Delta\eta$ =3) cannot prevent substantial entrainment of cratonic material if the cratonic root is not compositionally buoyant (Fig.5.3B, 5.4C). This illustrates that compositional buoyancy could cancel the negative thermal buoyancy of cratonic root and thus keep cratonic material stay underneath the area surrounding the craton (Fig.5.4A, 5.4B). The changes in the geometry of cratonic root in model N7 (Fig.5.4D) also shows the compositional buoyancy has some effects on the long-term deformation of cratonic roots. However, due to the

lack of sufficient negative thermal buoyancy to counteract the compositional buoyancy, the lowermost cratonic root may suffer from an extensional gravity instability that stretches the root and thus smoothes the boundary between cratonic and non-cratonic lithosphere as Fig.5.4B shows. Hence, the compositional buoyancy of the cratonic root plays a dual role: while compositional buoyancy can help resist the entrainment of cratonic material into asthenosphere significantly and contribute to the longevity of thick cratons, it may also reduce the craton thickness

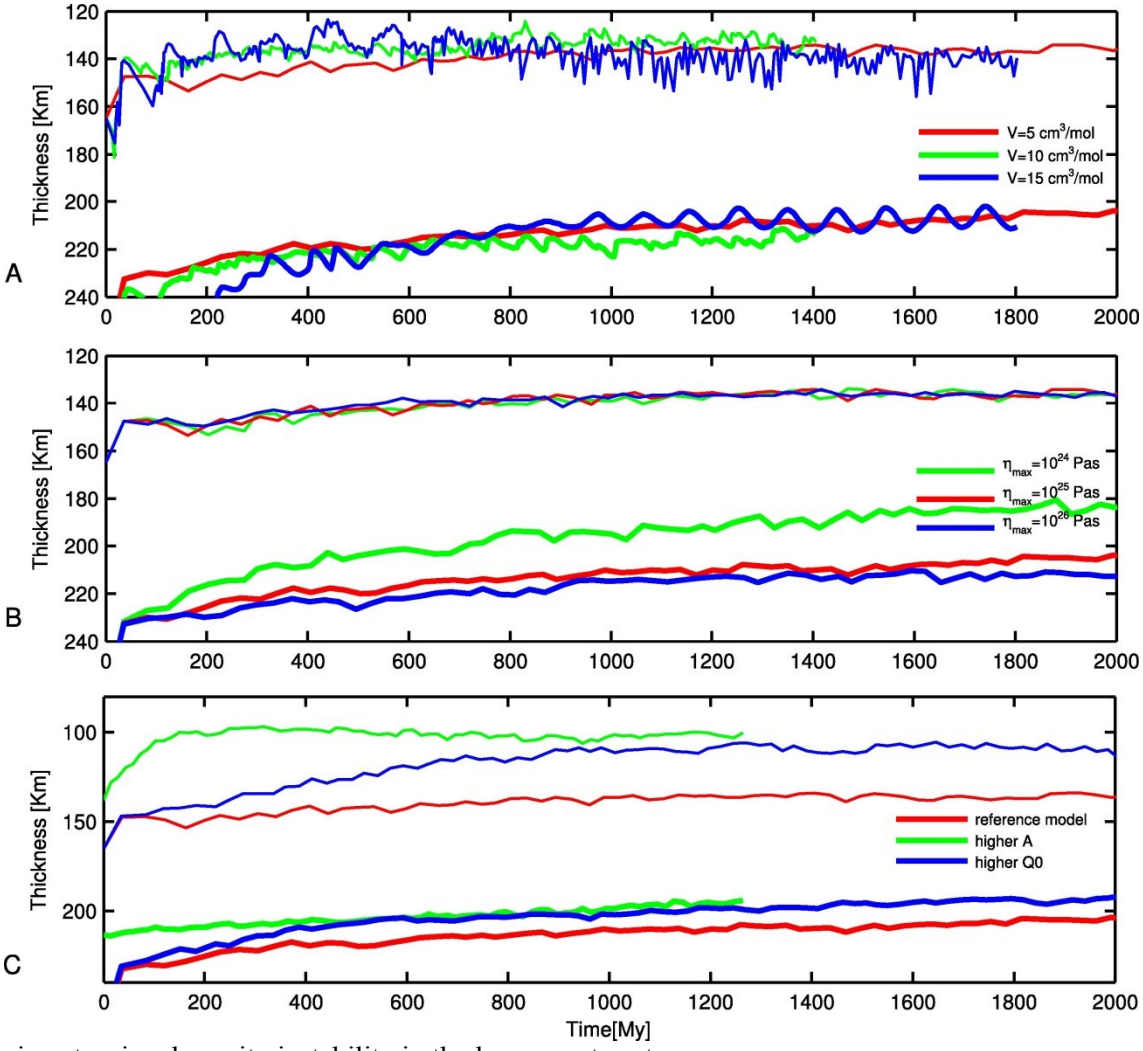

via extensional gravity instability in the lowermost root.

Fig. 5.5*: Thickness evolutions of cratonic and non-cratonic lithosphere over a time period of 2000 Myrs in different models, compared with the reference model N3. (A): Different activation volumes (models N9, N10). (B):Different maximum viscosity cutoff (models N11, N12). (C): More vigorous mantle by reducing the background viscosity with higher A (model N13) or using higher radioactive heating Q0 (model N14).*

Despite the significant effect of compositional buoyancy in some of the models discussed here, it is unlikely to play a dominant role in the survival of cratons for billions of years. Compositional buoyancy has important influence in models with less strong cratonic roots (model N1, N2), but the geometry of cratonic root is not well preserved in these models. The models

with $\Delta\eta$ =10 or more have the capacity to maintain long-living cratons, but in those models, the role of compositional buoyancy is rather modest.

5.3.4 Mantle viscosity

Long term craton stability may not only be affected by the strength of the cratonic root itself, but also by the viscous properties of the surrounding mantle and lithosphere [*Doin et al.*, 1997; *Beuchert et al.*, 2010]. In this section, models are designed to investigate the effects of pressure-dependent viscosity and the maximum lithospheric viscosity cut-off. Additionally, experiments with less viscous mantle and a warmer mantle are also performed in order to explore the parameter sensitivity.

Relative to reference model N3, we first increase the activation volume from 5 cm^3/mol to 10 and 15 cm^3/mol in model N9 and N10. In order to keep non-cratonic lithosphere at around 140 km, the basal temperature and rheological parameter A were adjusted accordingly. Higher activation volume V induces stronger variations of lithosphere thickness, but a thickness difference of ~70 km between cratonic and non-cratonic lithosphere is still maintained (Fig. 5.5A). Higher V increases the viscosity of the deeper mantle, which results in a thicker basal thermal boundary layer and larger, less frequent, but more regular upwelling thermal structures forming under the cratons, which, in turn, tend to erode the cratonic root slightly (Figs.5.2, 5.6A, 5.6C). This induces a periodic pattern of cratonic root thickness variations in model N10 (Fig. 5.5A). The shape of the cratonic roots deforms due to these upwelling thermal structures shown in Figs.5.6A and 5.6C, but they do not thin the cratonic lithosphere significantly. Hence, a strengthening factor of 10 with non-Newtonian rheology could still ensure long term craton stability even with stronger pressure dependence of the viscosity.

To investigate the effects of viscosity contrast, model N11 and N12 were performed with a maximum viscosity changed from 10^{25} Pa·s to 10^{24} Pa·s and 10^{26} Pa·s, respectively (Fig.5.5B). While the non-cratonic lithosphere keeps the same thickness as in the reference model, a higher maximum viscosity makes only marginal difference to cratonic lithosphere, whereas a lower maximum viscosity leads to a significant thinning of cratonic thickness (Fig.5.5B). This confirms that the default viscosity contrast in our model is sufficiently high for long term craton stability, that more elevated values will not induce a substantial difference, and that a significantly lower value would not be sufficient to maintain craton stability for billions of years.

Model N13 and N14 in Fig.5.5C illustrate the effects of a more vigorous and warmer mantle, respectively, conditions that may be applicable to the Archean Earth [*Herzberg et al.*, 2010]. Both cratonic and non-cratonic lithosphere are thinner than in the reference model N3, but the thinning of cratonic lithosphere (~10-15 km) is significantly smaller than that of non-cratonic lithosphere (~30-40 km) (Figs.5.5C, 5.6B, 5.6D). This shows that a difference in thickness be-

tween two types of lithosphere is expected to maintained (or even enhanced) in a more vigorous mantle.

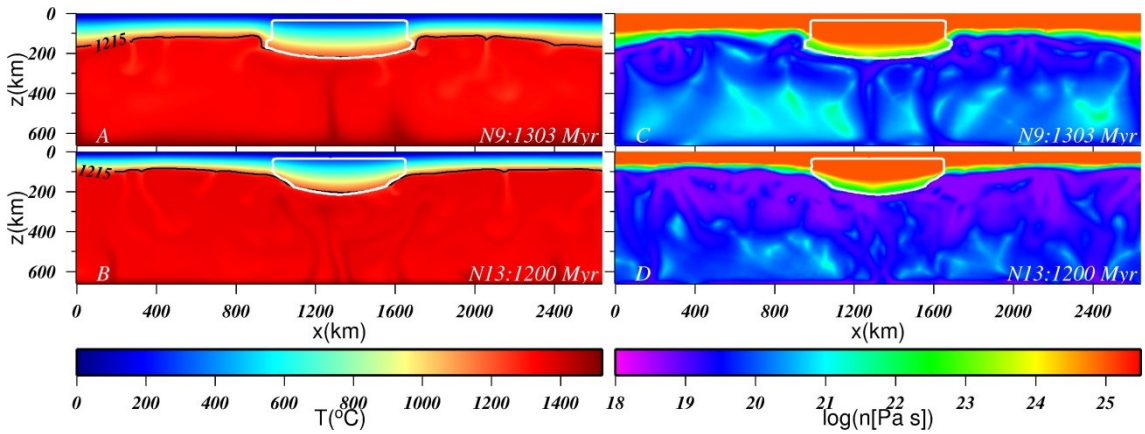

Fig. 5.6: *Temperature (A,C) and viscosity (B,D) distribution of model N9 (V=10 cm^3/mol)at 1.3Gyr and model N13 at 1.2 Gyr from the model start time. Model N9 shows the effects of stronger pressure-dependent rheology, which strengthens the upwelling flow under cratons. Model N13 shows the effects of a more vigorous mantle, in which the thickness of non-cratonic lithosphere decreases much more than cratonic lithosphere.*

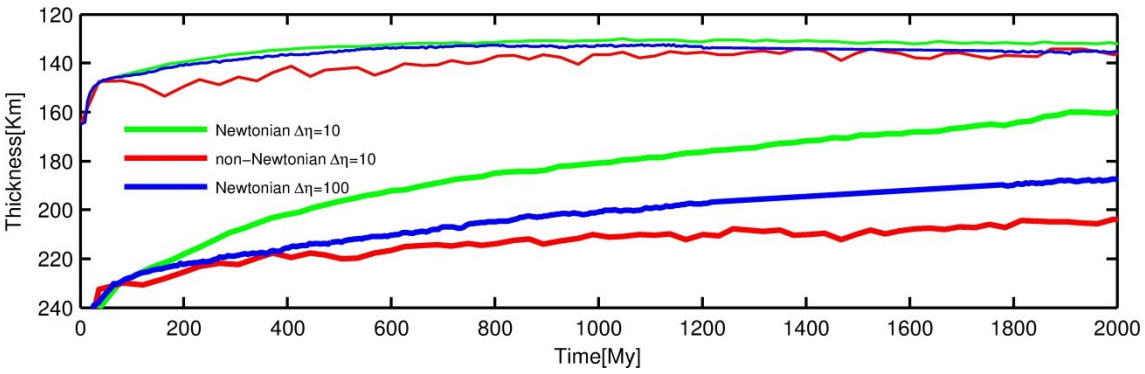

Fig. 5.7: *Thickness evolutions of cratonic and normal lithosphere over a time period of 2000 Myrs for Newtonian rheology models (L1, L2), compared with reference model N3.*

5.3.5 Newtonian rheology

All previous models were calculated using a non-Newtonian rheology with typical dislocation creep parameters. To compare with previous studies and to put the non-Newtonian results in context, we performed several Newtonian calculations. The activation energy is chosen within the range from laboratory experiment, and the rheological pre-factor A is adjusted to assure that non-cratonic lithosphere maintains a thickness of ~140 km (Table 5.2). Fig.5.7 shows the lithosphere thickness evolution in Newtonian models (L1 and L2), together with the reference model N3 for comparison.

A modest activation volume of V=2.5 cm^3 /mol is used in model L1 and L2 to introduce a pressure-dependent rheology and a slightly more viscous transition zone. In Newtonian rheology, $\Delta\eta$ =10 cannot maintain a cratonic root whereas $\Delta\eta$ =100 enables the cratonic root to maintain a thickness of ~190 km for 2 Gyrs (Fig.5.7). This required viscosity contrast for Newtonian rheology agrees with the findings by *O'Neill et al.* [2008], who found that a viscosity ratio of 50~150 is required between the cratonic root and asthenosphere when Newtonian rheology is applied. However, our reference model N3 and even model N2 ($\Delta\eta$ =10 and $\Delta\eta$ =3 with non-Newtonian rheology) still preserve cratonic lithosphere better than model L2 ($\Delta\eta$ =100 with Newtonian rheology) according to the thickness evolutions of cratonic lithosphere (Figs 5.3A, 5.7).

5.4 Discussion

5.4.1 Comparison with previous work

Our geodynamical models illustrate the critical role of compositionally dependent rheology and buoyancy in the long-term stabilisation of thick Archean lithosphere. A strengthening factor of $\Delta\eta$=10 in non-Newtonian rheology can protect the cratonic keel in a stagnant lid situation for billions of years even with little or no compositional buoyancy, while a smaller strengthening factor $\Delta\eta$=3 could also maintain thick but neutrally buoyant cratonic root (isopycnic status). In comparison with laboratory studies on mantle rheology, strengthening factor of $\Delta\eta$ in Eq. (5.9) would translate into $\Delta\eta^n$ for the constant-stress definition used in the laboratory studies. Therefore, $\Delta\eta$=10 falls into the range of experimental results for dehydration strengthening for dislocation creep between ~140 [*Hirth and Kohlstedt*, 1996] and 10000 [*Karato*, 2010]. *Fei et al.* (2013) argue that that the effect of water on viscosity of upper mantle is only up to one order of magnitude. Such low values may apply better to our findings that $\Delta\eta$ = 3 with non-Newtonian rheology might be sufficient to support longevity, and could indicate that buoyancy plays a more significant role.

The role played by composition-dependent rheology has been previously questioned by *Beuchert et al.* [2010], with the argument that published numerical models have insufficient temperature dependent viscosity contrast, which could drives an artificial requirement for composition dependent rheology. Our research confirms that the viscosity contrast of 10^5, normally used in many geodynamic modelling, is not suitable for modelling long term craton stability (Fig.5.5B). However, our models shows that composition-dependent rheology is still required to resist the long term erosion and maintain the different thicknesses between cratonic and non-cratonic lithosphere, and such behaviour is almost inevitable from the observed compositional variation of many cratonic lithospheres [e.g., *Pearson and Wittig*, 2013]. The erosion process in our model, previously described as entrainment of cratonic material, requires high viscosity rather than buoyancy alone for craton preservation as emphasized by *Sleep* [2003]. Using a scal-

ing law relationship, *Sleep* [2003] concluded that weakly temperature dependent viscosity require lower strengthening factor than strong temperature-dependent viscosity. With non-Newtonian rheology, the temperature dependence of viscosity is reduced by a factor of "n" (3.5) and also by the strain rate dependence compared to Newtonian rheology , which plausibly explain why non-Newtonian rheology require a much smaller $\Delta\eta$ than Newtonian rheology in our models.

5.4.2 Cratons in a thermally evolving earth

Our models are designed largely from consideration of the current mantle status and result in a strengthening factor of 10 or less is required for long term craton stability. It is widely accepted that the mantle in the Archean was much hotter and thus more vigorous than the current mantle [e.g., *Herzberg et al.*, 2010]. A hotter early mantle means that cratons possibly experienced stronger convection and erosion when formed in the Archean and so we need to consider this potential effect. As our models show, the thickness difference of more than 70 km between cratonic and non-cratonic lithosphere could persist in a less viscous upper mantle (Figs. 5.5C, 5.6B, 5.6D), even though such a hotter mantle leads to a reduced thickness of both cratonic (10~15 km) and non-cratonic lithosphere (30~40 km). Hence, the $\Delta\eta$=10 in our model is able to maintain the thickness difference between cratonic and non-cratonic lithosphere in a hotter and vigorous mantle, thought to be more akin to Archean conditions. More realistic convection parameters of the present-day Earth with plate tectonics and perhaps mantle plumes, might require additional conditions for the survival of cratons, such as weak mobile belts or continental margins [*Lenardic et al.*, 2000, 2003; *Yoshida*, 2010, 2012]. However, this is beyond the scope of this paper.

The compositional buoyancy of cratonic roots could delay the erosion from small-scale convection significantly (Figs. 5.3A and 5.3B) and has an influence on the long term deformation and shape of cratonic roots (Figs. 5.2 and 5.4D), but it is not really necessary for craton preservation. The intrinsically more viscous cratonic root would allow modest negative buoyancy of the cratonic root according to our numerical experiments. Modest negative, or variable buoyancy in cratonic roots is consistent with modelling of temperature induced gravity anomalies beneath cratons [*Kaban et al.*, 2003]. that indicates that density variations due to temperature are only partly compensated for by density variations due to composition. Such observations along with petrological studies of cratonic mantle xenoliths that show variations in density with depth/equilibration temperature deviating significantly from the expected variation of density with depth for an isopycnic state [*Boyd et al.*, 1997; *Lee et al.*, 2006; *Schutt and Lesher*, 2010] indicate that the "isopycnic" hypothesis of *Jordan* [1978] is not a necessary condition for craton survival. Furthermore, a 500~1500m topographical depression of cratons compared to previously predictions from pure crustal isostasy, has been suggested by crustal isostatic re-

search [*Mooney and Vidale*, 2003]. This, combined with the fact that a number of cratons with thick lithospheric roots such as the Kaapvaal and Siberian cratons are covered to some degree with Phanerozoic oceanic sediments, indicates that craton freeboard might have varied through time. Our modelling has the important implication that the common petrological processes that lead to an increase in the density of the cratonic root after their formation, such as refertilization of peridotites by silicate metasomatism [*Simon et al.*, 2003; *Schutt and Lesher*, 2010] do not necessarily jeopardize the stability of cratons.

5.4.3 Implications for thinning of cratonic lithosphere

The process of thinning and removing cratonic lithosphere has generated great attention recently since some cratons have been found to have lost part of, or most of their lithospheric roots [*Fan and Menzies*, 1992; *Kusky et al.*, 2007; *Foley*, 2008; *Lee et al.*, 2011]. Our models illustrate that the cratonic root should be more viscous and thus very robust against long term erosion by small-scale convection, and explain craton stability and longevity in a stagnant lid regime. Geodynamical modelling of the process of significant removal of cratonic lithosphere should take this increased viscosity of cratonic root into account. As the cratonic root is more viscous than normal mantle under the same conditions, the heating (from mantle plumes or any other thermal events) would likely have a bigger impact on non-cratonic lithosphere than on cratonic roots. The greater susceptibility of less depleted, non-cratonic mantle to thermal erosion is in line with the observed thickness reduction experienced by circum-cratonic lithosphere in southern Africa [*Bell et al.*, 2003; *Mather et al.*, 2011]. Given the robustness of cratonic roots, a special weakening mechanism is required to destabilize them.

Compared with previous studies, this study shows that non-Newtonian rheology (dislocation creep regime) with compositional strengthening due to mantle depletion and dehydration that is in agreement with laboratory experimental studies is able to ensure long term craton stability. This point, on the other hand, also indicates the cratons could be very susceptible to stress change. Furthermore, recent laboratory experiments show that the interaction between melt segregation and stress would weaken mantle material more than a homogeneous melt distribution [*Holtzman et al.*, 2012]. This effect would enhance the stress and strain rate localization during any thermal-tectonic events and make significant removal of cratonic lithosphere possible. Water, despite its debated direct effects on mantle rheology, could also play an important role as it could induce hydrous redox melting by lowering the solidus of mantle rocks and thus weaken cratonic root in that way [*Foley*, 2008, 2011; *Green et al.*, 2010]. These factors, combined with stress effects, need to be investigated geodynamically for their potential to destroy cratonic roots.

5.5 Conclusion

We have studied the role played by composition-dependent rheology and buoyancy on craton stability and longevity in non-Newtonian rheology. Based on our models, the following points are concluded.

1. Composition-dependent rheology is necessary in order to maintain a different thickness between cratonic and normal lithosphere for over billions of years.

2. With non-Newtonian rheology, a strengthening factor of 10 could preserve a cratonic root from the erosion by small scale convection over 2 Gyrs, no matter whether the cratonic root is compositionally buoyant or not. A smaller strengthening factor ($\Delta\eta$=3) can also protect the cratonic root from eroding away for billions of years but a neutrally buoyant root is also required in this scenario.

3. The buoyancy of a cratonic root does have some effects on long term cratonic stability, but its effects may be secondary compared to composition-dependent rheology. Positive or even modest negative buoyancy of a cratonic root is permitted, provided that sufficient composition-dependent rheology is present. This conclusion is in agreement with the relatively subtle petrological controls on the buoyancy of mantle rocks and the geological evidence that the freeboard of cratons may have varied considerably through time, with several cratons having been at or below sea level for distinct periods.

Acknowledgments

The authors would like to thank Masaki Yoshida and an anonymous reviewer for their very constructive reviews that helped to improve this work significantly. The work has been supported by EU FP7 Marie Curie Initial Training Network ‘Topomod’, contract no. 264517 (HW). JvH acknowledges funding from the European Research Council (ERC StG 279828).

Chapter 6

The thinning of subcontinental lithosphere: the roles of plume impact and metasomatic weakening[3]

Abstract

Geologically rapid (10s of Myr) partial removal of thick continental lithosphere is evident beneath Precambrian terranes such as North China Craton, southern Africa and the North Atlantic Craton, and has been linked with thermo-mechanical erosion by mantle plumes. We performed numerical experiments with realistic viscosities to test this hypothesis and constrain the most important parameters that influence cratonic lithosphere erosion. Our models indicate that the thermo-mechanical erosion by a plume impact on typical Archean lithospheric mantle is unlikely to be more effective than long-term erosion from normal plate-mantle interaction. Therefore, unmodified cratonic roots that have been stable for billions of years will not be significantly disrupted by the erosion of a plume event. However, the buoyancy and strength of highly depleted continental roots can be modified by fluid-melt metasomatism, and our models show that this is essential for the thinning of originally stable continental roots. The long-term but punctuated history of metasomatic enrichment beneath ancient continents makes this mode of weakening very likely. The effect of the plume impact is to speed up the erosion significantly and help the removal of the lithospheric root to occur within 10s of Myr if affected by metasomatic weakening.

[3] This Chapter has been accepted for publication in Geochemistry, Geophysics, Geosystems as "The thinning of subcontinental lithosphere: the roles of plume impact and metasomatic weakening" by Hongliang Wang, Jeroen van Hunen and D. Graham Pearson. All model development and results were performed and the manuscript written by H. Wang. The co-authors have participated in this study by providing training, feedback on the manuscript, and useful discussions.

6.1 Introduction

The contrasting composition and heterogeneity between ancient cratonic and oceanic lithosphere is one of the most salient features of modern plate tectonics. Thick Archean cratonic lithosphere is generally considered to be stable and dynamically inactive since it was formed. However, the discovery that the North China Craton (NCC) has lost a significant part of its root in the Mesozoic [*Gao et al.*, 2002a; *Zhu and Zheng*, 2009] shows that cratons are not isolated features in Earth's dynamic system. The chemical distinction of highly melt-depleted cratonic roots is considered to be the most important reason for the survival of Archean lithosphere [*Boyd,* 1989; *Carlson et al.,* 2005]. Geodynamical research supports this hypothesis through numerical modeling by using reasonable density structure and mantle rheology [*Doin et al.*, 1997; *Lenardic and Moresi*, 1999; *O'Neill et al.*, 2008; *Wang et al.*, 2014].

Increasing evidence due to the development of modern geochemical and petrological techniques shows that many Precambrian terranes have experienced some degree of progressive, multistage modification (or enrichment) to their roots through mantle metasomatism [e.g. *Carlson et al.,*2005; *Hanghøj and Kelemen*, 2001; *Simon et al*., 2003; *Chesley et al.,* 2004; *Sand et al.*, 2009; *Janney et al.*, 2010; *Tappe et al.*, 2011; *Tang et al.*, 2013; *Smit et al.,* 2014], even though such roots appear to be mostly physically stable. Seismic tomography further indicates the widespread refertilization of Archean lithosphere by mantle thermal events, e.g. the Bushveld and Karoo events in the Kalahari craton [*James et al.*, 2001; *Griffin et al.*, 2003a]. Through fluid/melt-rock interaction, metasomatic refertilization might increase the density and weaken the rheology of sub-continental lithospheric mantle (SCLM) and thus affect its stability [*Schutt and Lesher*, 2010]. By decreasing the Mg number (Mg#) of the originally depleted continental lithosphere and raising its pyroxene and garnet content, the enrichment of the depleted mantle could reduce the chemical buoyancy of SCLM significantly [*Pearson and Nowell*, 2002; *Griffin et al.*, 2003b; *Carlson et al.*, 2005; *Pearson and Wittig*, 2008; *Gibson et al.*, 2013]. Metasomatic processes might also have a weakening effect on the rheology of the constituent peridotites by adding water to the originally dry, depleted continental root [*Peslier et al.*, 2012]. Moreover, research on the Slave craton in Canada indicates that metasomatism may affect the mantle rheology based on the correlation between elastic thickness and mantle composition [*Poudjom Djomani et al.*, 2005]. Hence, the accumulating evidence that metasomatic refertilization affects both the compositional buoyancy and the rheology of the SCLM and leads to the possible destabilization of thick lithospheric roots, provides the motivation to numerically simulate this process to constrain the overall controls.

Although most Precambrian terranes appear to have been geologically stable/inactive, many have experienced some degree of thinning or recycling [*Lee et al.*, 2011], such as the North China Craton (NCC) [*Gao et al.*, 2002a], the Wyoming craton [*Carlson et al.*, 2004], the Colo-

rado plateau [*Levander et al.*, 2011], the Proterozoic lithosphere around the Kaapvaal craton [*Bell et al.*, 2003; *Mather et al.*, 2011], and the North Atlantic Craton (NAC) [*Tappe et al.*, 2007]. The destruction of the NCC appears to be a unique example of complete removal of the cratonic root, and has received a lot of attention recently [*Zhu and Zheng*, 2009]. With its abundant kimberlite pipes, the Kaapvaal craton of southern Africa provides a good natural laboratory to study the modification and evolution of Precambrian lithosphere [*Simon et al.,* 2003; *Griffin et al.,* 2003a; *Gibson et al.,* 2008; *Kobussen et al.*, 2008]. *Carlson et al.* [2005] suggested that the loss of buoyancy through mantle metasomatism is a possible mechanism that could rapidly transfer the continental lithospheric mantle into the asthenosphere and cause intracontinental deformation and volcanism. These events might, in some cases, lead to continental breakup [*Tappe et al.*, 2007]. The increased temperatures and flow stress related to mantle plume impact provide another, perhaps related mechanism for the lithosphere removal events [*Ebinger and Sleep*, 1998; *Sleep et al.*, 2002; *Bell et al.*, 2003].

Geodynamical modeling has long been used to study the general mantle dynamics of plume–lithosphere interaction [*Ribe and Christensen*, 1994; *Nyblade and Sleep*, 2003; *van Hunen and Zhong*, 2003; *François et al.*, 2012], but the mechanical erosion and thinning of the continental lithosphere has received less attention. *Sleep et al.* [2002] demonstrated that a cratonic root can deflect plume material and convection can focus on the edge of the root, which could lead to a reduction of the root width. *Morency et al.* [2002] found that, depending on the width of the cratonic block, it takes 50 -750 Myrs to convectively remove a 250 km thick cratonic root if the lithosphere has an equilibrium thickness of about 100 km, but the chemical heterogeneity of continental lithosphere and plume events were not considered in their study. *Guillou-Frottier et al.*, [2012] argued for several different plume-induced dynamical instabilities near the cratonic root to explain the P-T-t paths recorded by the metallogenic data from South Africa. These studies do not explicitly explore the role of compositional buoyancy and strengthening on cratonic mantle dynamics for a situation in which a plume impacts on the subcontinental root. In particular, metasomatic refertilization could change the chemical heterogeneity of mantle lithosphere, and may have important geodynamical consequences.

In this study, we perform new numerical experiments to explore how the buoyancy and rheology of subcontinental lithosphere affect plume-continent interaction and study the mechanism of lithosphere removal. The potential mechanisms of lithosphere removal underneath Precambrian terranes such as southern Africa and the NCC will be discussed based on the numerical results.

6.2 Model description

6.2.1 Governing equations

We use a Cartesian version of the finite element code Citcom [*Moresi and Solomatov*, 1995; *Zhong et al.*, 2000; *van Hunen et al.*, 2005] to solve the incompressible flow with the extended Boussinesq approximations [*Christensen and Yuen*, 1985; *King et al.*, 2010]. It solves the following non-dimensional governing equations for mass, momentum, energy conservation:

$$\nabla \cdot \mathbf{u} = 0 \tag{6.1}$$

$$-\nabla P + \nabla \cdot \left(\eta\left(\nabla \mathbf{u} + \nabla^{\mathrm{T}} \mathbf{u}\right)\right) + \left(RaT - Rb_i C_i\right)\mathbf{e}_z = 0 \tag{6.2}$$

$$\frac{\partial T}{\partial t} + \mathbf{u} \cdot \nabla T = \nabla^2 T + Q_0 + \frac{Di}{Ra}\eta \dot{\varepsilon}^2 + Di\,(T + T_s)u_z \tag{6.3}$$

A standard non-dimensionalization is used with $x = x'h, t = t'h^2/\kappa, \eta = \eta'\eta_0$, where, in the equations above, the primes of the non-dimensional parameters are dropped for clarity. The dimensional physical parameters are listed and explained in Table 6.1. The thermal and chemical Rayleigh number Ra and Rb_i are defined as:

$$Ra = \frac{\alpha \rho_0 g \Delta T h^3}{\kappa \eta_0} \tag{6.4}$$

$$Rb_i = \frac{\delta \rho_i g h^3}{\kappa \eta_0} \tag{6.5}$$

$$Di = \frac{\alpha g h}{c_p} \tag{6.6}$$

A particle-tracking technique is used to track different chemical materials) [*van Hunen et al.*, 2000; *Di Giuseppe et al.*, 2008], which has been benchmarked against *van Keken et al.* [1997] and *Schmeling et al.* [2008]. The following compositional equation is thus solved:

$$\frac{\partial C_i}{\partial t} + \mathbf{u} \cdot \nabla C_i = 0 \tag{6.7}$$

Table 6.1 Symbols, units and default parameters.

Symbol	Description	Default value and units
A	rheological pre-exponent (dislocation)	[$MPa^{-n}s^{-1}$]
B	rheological pre-exponent (diffusion)	[MPa^{-1}]
E	activation energy	500 (ds), 300 (df) [kJ/mol]
V	activation volume	10(ds), 6(df) [cm^3/mol]
g	gravitational acceleration	9.8 [m/s^2]
h	model height	660 [km]
C_p	thermal capacity	1250 [J $kg^{-1}K^{-1}$]
n	rheological power law exponent	3.5 (ds), 1 (df) [-]
P	deviatoric pressure	[Pa]
R	gas constant	8.3 [J/mol]
Ra	thermal Rayleigh number	$4.43x10^6$ [-]
Rb	compositional Rayleigh number[a]	$1.69x10^7$, $1.48x10^6$ [-]
T	temperature	[^{0}C]
T_s	surface temperature	273 [K]
ΔT	temperature drop over model domain	1350 [^{0}C]
T_p	maximum plume excess temperature	250 [^{0}C]
R_p	plume radius	50 [km]
έ	strain rate	[s^{-1}]
α	thermal expansion coefficient	$3.5x10^{-5}$ [K^{-1}]
η_0	reference viscosity	10^{20} [Pa·s]
η	viscosity	[Pa·s]
κ	thermal diffusivity	10^{-6} [m^2/s]
ρ	mantle density	3300 [kg/m^3]
$\Delta\rho_1$	density difference of upper crust and man-	600 [kg/m^3]
$\Delta\rho_2$	maximum density change due to depletion	52.5 [kg/m^3]
Q_0	radioactive heating	0.04 [$\mu W/m^3$]
C_i	composition field	0~1 [-]
C_η	rheologically effective composition value[b]	0.6 [-]
$\Delta\eta_0$	strengthening factor when $C \geq C_\eta$	[-]

[a] $1.69x10^7$ and $1.48x10^6$ are the compositional Rayleigh numbers for crust and cratonic root, respectively.

[b] Cη is chosen to make the second cratonic layer has the maximum strengthening factor due to its initial compositional field.

Two particle functions are used in our models, with *i*=1 and 2 representing the crust and the depleted mantle, respectively. As non-Newtonian rheology has been found to be important for both the stability and dynamics of the cratonic lithosphere [*Wang et al.,* 2014; *Wang et al.*, 2015], we use a composite rheology of non-Newtonian and Newtonian rheology to represent the dislocation creep and diffusion creep, respectively. Thus, the composition-dependent viscosities are calculated as follows:

$$\eta_{dl} = A^{\frac{-1}{n}} \dot{\varepsilon}^{(\frac{1-n}{n})} exp\left(\frac{E + \rho gzV}{nRT}\right) \times \Delta\eta \tag{6.8}$$

$$\eta_{df} = Bexp\left(\frac{E + \rho gzV}{RT}\right) \times \Delta\eta^{n} \tag{6.9}$$

$$\eta_{eff} = min\left(\eta_{dl}, \eta_{df}\right) \tag{6.10}$$

The implementation of non-Newtonian rheology has been benchmarked against *Christensen* [1984]. Due to the non-linear stress-strain rate relationship used in the composite rheology, the effective compositional viscosity increase depends on the ambient stress or strain rate, and two end member situations exist. For the hypothetical case that strain rate is kept constant, changing the strengthening factor Δη in Eq. (6.8) will change the effective viscosity proportionally. If, however, stress remains constant, then increasing Δη will result in an effective viscosity increase of $\Delta\eta^n$. In this study, we report 'constant strain rate' values Δη in Eq. (6.8) and values used (Δη =2, 3, 4, 5, 6) actually lead to an increase of non-Newtonian viscosity by $\Delta\eta^n$ =11.3, 46.8, 128, 279.5 and 529.1 in the definition of "constant stress". Thus, we use a strengthening factor of $\Delta\eta^n$ for Newtonian viscosity in Eq. (6.9) to have similar compositional effect. Considering the significant variation in the results of the laboratory experiment on mantle rheology [*Hirth and Kohlstedt*, 1996; *Karato*, 2010; *Fei et al.*, 2013], the range of strengthening factors in this study is considered representative.

6.2.2 Model setup

The computational domain is 660 km deep and 3980 km wide, with mantle plumes rising up on the left side of the thick chemical root (hereafter referred to as the "craton"). This model setup is illustrated in Fig. 6.1A together with the mechanical and thermal boundary conditions. We calculated a model with a stable chemical root (with compositional buoyancy and strengthening factor of $\Delta\rho$ =31.5 kg/m^3 and $\Delta\eta$=4, respectively) to a quasi-steady-state thermal condition and use it as the initial temperature field in this study. Typical thermal and viscosity profiles for cratonic and normal lithosphere are displayed in Fig. 6.1B and 1C.

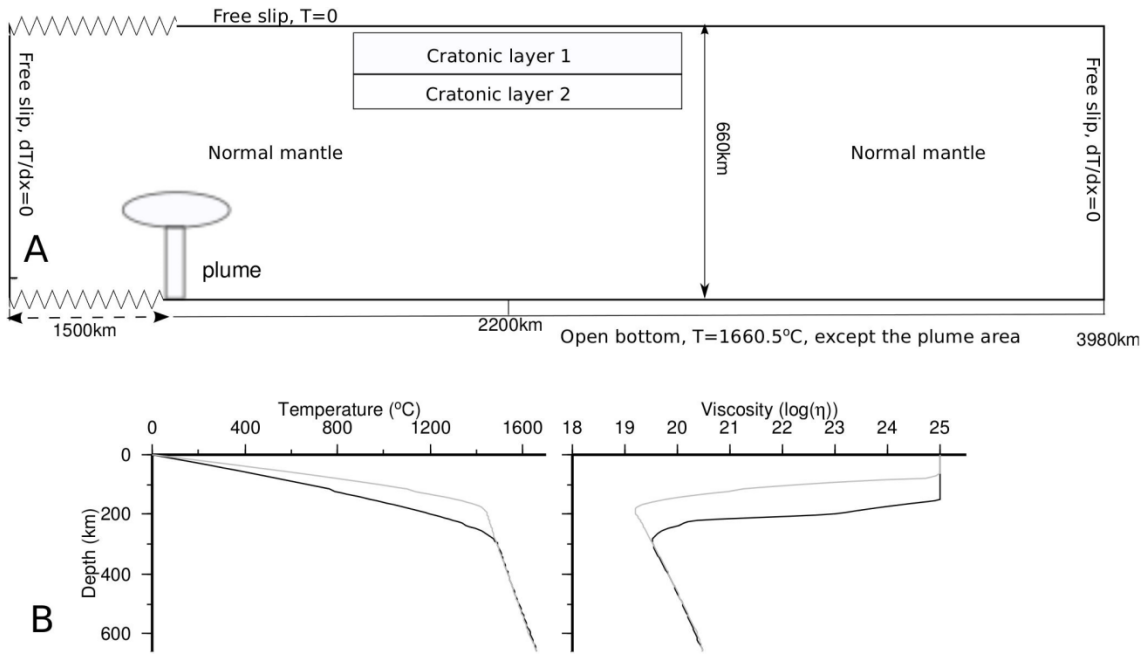

Fig. 6.1: *A) Model setup, including the initial chemical layers of cratonic root, mechanical thermal boundary condition and plume locations. B) Typical geotherms (left) and effective viscosity profile (right) of cratonic (black) and normal lithosphere (grey) as the initial thermal condition.*

A two-layer chemical root is used, with the following characteristics for all the cases in the parametric study (section 6.3): (1) a highly depleted layer from 36 km (Moho) to 150 km depth in which the chemical value decrease from 1 to C_η; (2) a less depleted layer from 150 to 200 with constant chemical value C_η. To avoid the sharp transition between chemical root and asthenosphere, a 20 km thick buffer layer is added underneath the chemical root in which the chemical value gradually decreases to 0. Thus, an initial chemical root of 200-220 km is setup in our models. The composition value C tracked with tracers controls both the buoyancy and strengthening of continental root through:

$$\rho_c = \rho_m - C_i \Delta \rho_i \tag{6.11}$$

$$\Delta\eta = \Delta\eta_0^{\,min(1,\frac{C_2}{C_\eta})} \tag{6.12}$$

Because the two chemical layers in all calculations have initial compositional values larger than or equal to C_η, the initial strengthening factor of the whole root is always $\Delta\eta_0$ in Eq. (6.8)-(5.10). Any reasonable buoyancy variation of the first chemical layer is found to have little effect on the dynamics. So we focus on the compositional buoyancy ($\Delta\rho$) and strengthening factor ($\Delta\eta$) of the second layer to explore the effects of metasomatic refertilization on the depleted continental lithosphere. The density reduction due to a bulk rock Mg number (Mg#) change from fertile mantle (with Mg# = ~88) to depleted cratonic root (Mg# = 92–94) is found to be ~1.5-2.5% [*Schutt and Lesher*, 2010]. As the second layer is less depleted, we use a reduced density of 3258 kg/m^3 (density reduction of 42 kg/m^3 or 1.27% of the reference mantle density

of 3300 kg/m^3) to represent the maximum effect of mantle depletion on the density of lithosphere root. In order to quantitatively monitor the lithosphere thickness changes caused by the convective erosion, we define a thermal lithosphere-asthenosphere boundary (LAB) by the isotherm of T = 1325^{o}C and calculate the average thicknesses of the specific area through time.

Mantle plumes are generated through a basal Gaussian thermal anomaly with excess potential temperature T_p, and radius R_p [*Zhong and Watts*, 2002], centered at x=1500 km (unless stated otherwise) (Fig 6.1A). An open flow boundary condition is used at the bottom, so the thermal plume would rise up where the thermal anomaly is located. The instantaneous non-dimensional plume flux F_p is calculated at every time step as:

$$F_p = \int V_z \cdot dT ds \tag{6.13}$$

while the total plume inflow (F_{total}) is monitored using:

$$F_{total} = \int F_p dt \tag{6.14}$$

where V_z and dT are the vertical velocity and excess temperature at the bottom, respectively. By controlling the location, radius, and total plume inflow of the Gaussian thermal anomaly, a variety of different plumes are set up for different models. The plume forms at an arbitrary time (30 Myrs after the model start in most calculations) and ends automatically when the total plume inflow reaches a pre-defined threshold value. This procedure ensures the same total plume inflow for varying plume parameters such as the plume location or radius.

A total of 96-by-576 finite elements are used with mesh refinement near the root area, which provides a spatial resolution of 4.5 km per element for the root area and 8-9 km per element elsewhere. A total number of >2.5 million tracers are randomly distributed in the domain at the beginning of the computation, which provides an average tracer density of 47 tracers per element. In order to handle the tracer inflow and outflow, tracers at the elements facing any open boundaries are refreshed at every time step. Thus, the total number of tracers in the computation domain is statistically constant.

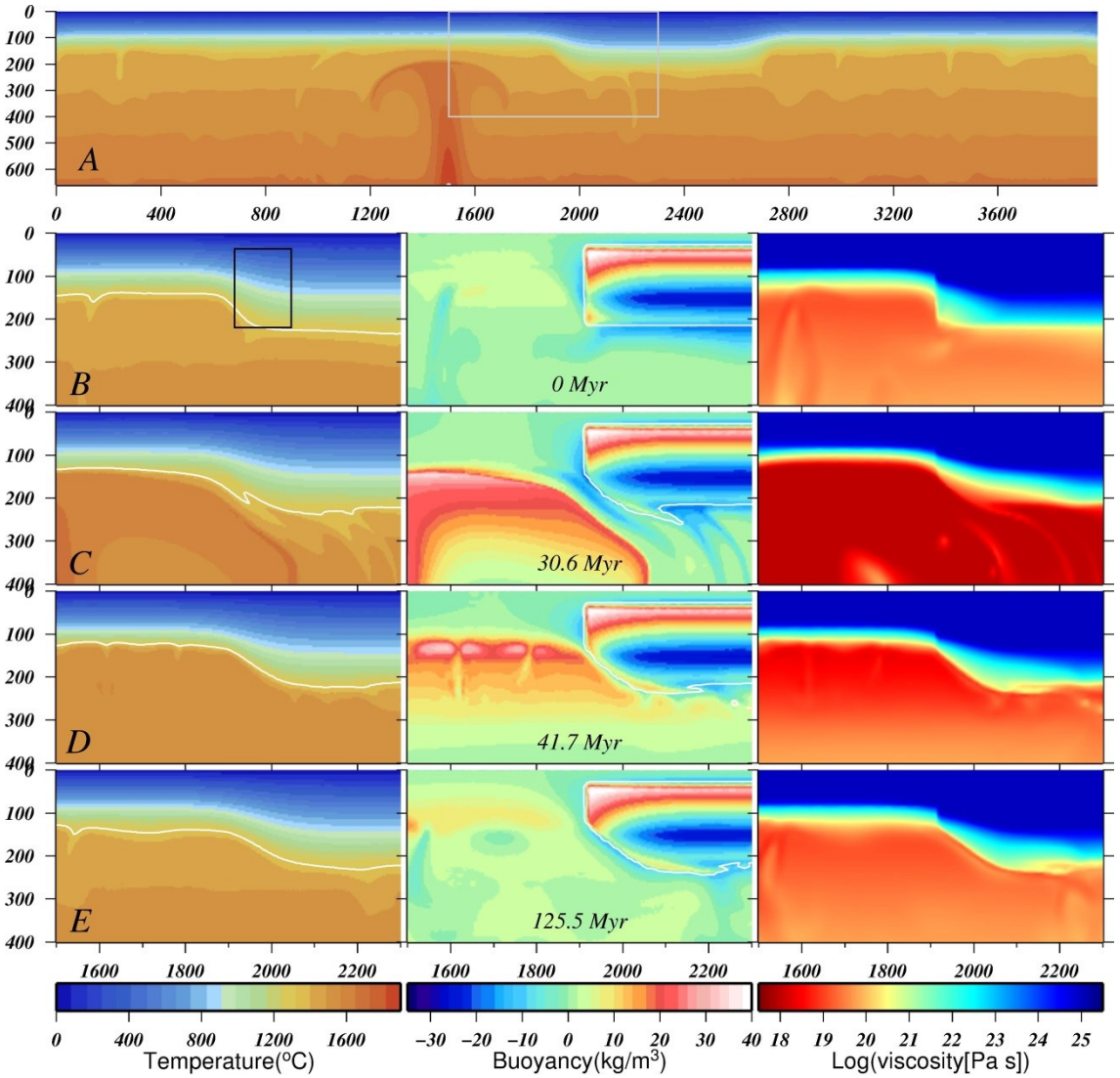

Fig. 6.2: *A) Temperature distribution when a plume rises up near the thick continental root. The grey box indicates the zoomed area in Fig. 6.2B-E to focus on the erosion of continental root by the plume induced flow. Fig. 6.2B-2E) The temperature (left), buoyancy (middle) and effective viscosity (right) of a model in which a plume (30 Myr) impacts the thick root, with four time snapshots at 0 Myr, 30.6 Myr, 41.7 Myr, 125.5 Myr, respectively. The chemical boundary of the root is outlined by the white line in the buoyancy field that is the defined by the C=0.1 contour. The black box in Fig 6.2B specifies the area of the left root edge where the erosion is monitored. This model has $\Delta\rho$=21kg/m^3; $\Delta\eta$=3. The buoyancy field is calculated relative to a reference density profile based on the average geotherm of normal lithosphere before the plume arrival.*

6.3 Plume-root interaction

We first illustrate how the plume impacts and erodes thick continental lithosphere through temperature, buoyancy, chemical, and viscosity evolution. Then the effects of different root buoyancy and strength are explored by monitoring the erosion of the root in different models. We also compare these models with those without any plumes to understand the actual effects of plume impact. Afterward, the effects of different plume setups are investigated.

6. 3. 1 Plume impact on the subcratonic root

Fig. 6.2A illustrates how a plume rises up near the edge of a craton, and impacts on the thick continental root. Fig. 6.2B-E show the temperature, buoyancy and viscosity images of four time snapshots when a plume impinges on the thick root in the enlarged area indicated in Fig 6.2A. The changing chemical root shape through time (Fig. 6.2B-2E) illustrates that the main impact and erosion focuses on the edge of the root whereas the top layer of the root shows little effect from the dynamics of plume impact. Therefore, we only further explore the effects of the compositional buoyancy ($\Delta\rho$) and the strengthening factor ($\Delta\eta$) of the lower cratonic layer on the erosional behavior of the root in the early stage. The root setup in Fig. 6.2 is characterized by $\Delta\rho$=21 kg/m^3, $\Delta\eta$=3 of the second layer, which is further explained in section 6.3.2. For other model calculations with different $\Delta\rho$ and $\Delta\eta$ (see below), the dynamical details might vary, but the general deformation pattern as shown in Fig. 6.2 still applies.

The buoyancy field has a strong vertical stratigraphy and the peak negative buoyancy is at a depth near the LAB of normal lithosphere (middle in Fig. 6.2B-E). This structure is dependent on the chemical layer setup and the thermal structure of both two types of lithosphere. The uppermost root is frozen by its positive or neutral buoyancy and high viscosity (>10^{24}Pa s, Fig. 6.2B-E.), and it has little effect on the dynamics. The deeper root area, that contains the maximum negative buoyancy, is also protected by its high viscosity (>10^{23} Pa s) as it is located in the interior of the root (Fig. 6.2B-E). The lowermost root is almost neutrally buoyant because the negative thermal buoyancy of the root decreases with depth. As it falls into the rheologically active area, the lowermost root is the most susceptible part to dynamical removal, especially in the peripheral area.

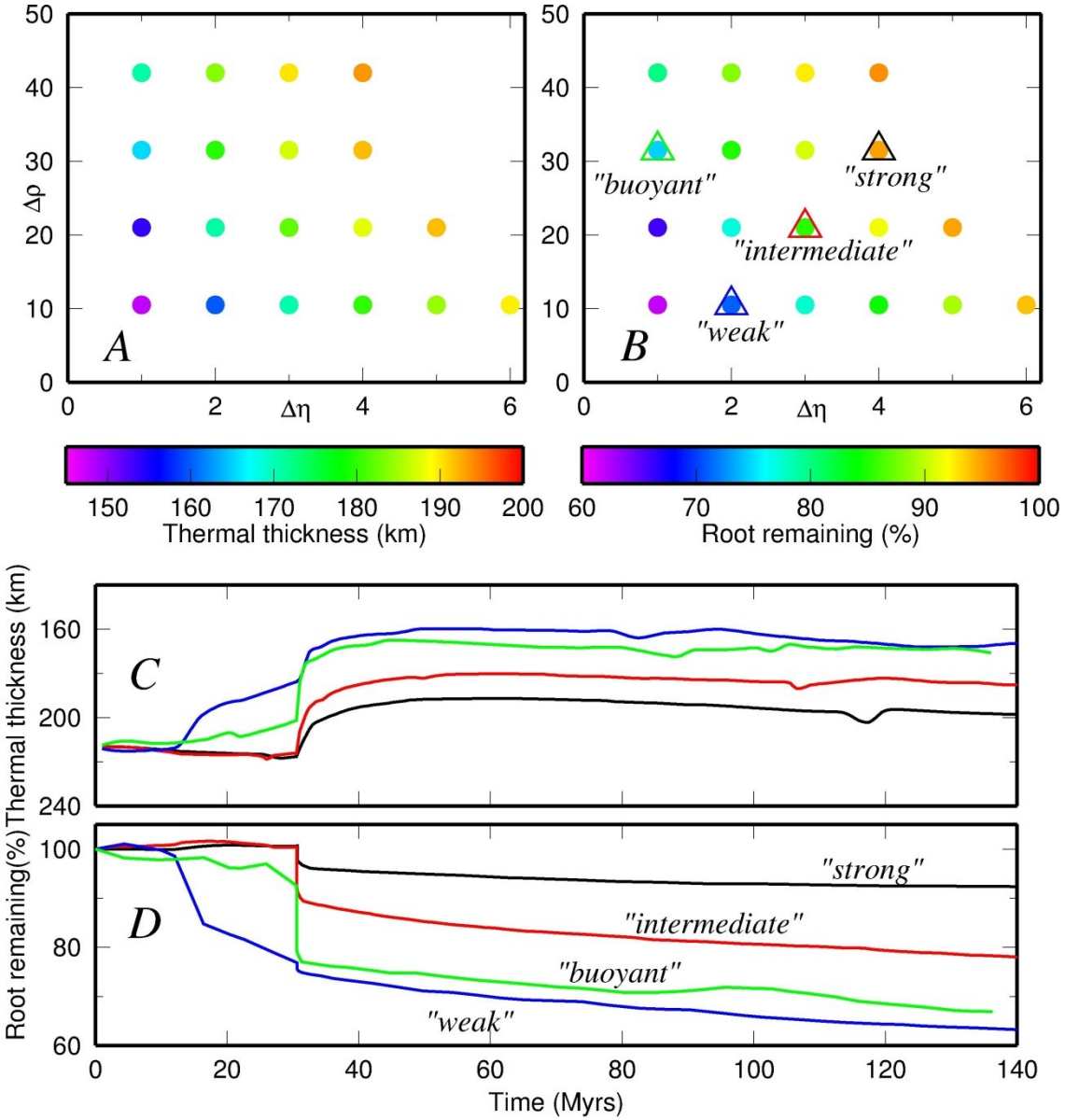

Fig. 6.3: *Effects of root chemical buoyancy and rheology on its erosion. (A) and (B) shows the average thermal lithospheric thickness (A, defined as the T=1325°C isotherm) and remaining chemical root percentage (B, in terms of geometrical volume) of the left root edge (1914 km-2046 km) at 50 Myrs after the model start time. C) and D) Evolution of average thermal thickness (C) and chemical root remaining (D) through 140 Myrs. Each line represents one of the models with a coloured triangle in Fig. 6.3B: a "strong" root (black, Δρ=31.5kg/m^3; Δη=4), an "intermediate" root (red, Δρ=21kg/m^3; Δη=3), a "weak" root (blue, Δρ=10.5kg/m^3; Δη=2), and a "buoyant" root (green, Δρ=31.5kg/m^3; Δη=1).*

When the buoyant plume material arrives and ponds nearby, the lower part of cratonic root becomes gravitationally more unstable and strongly sheared by the plume-induced flow (Fig. 6.2C-D). Due to the non-Newtonian rheology Eq. (6.8), the shearing of plume flow reduces the viscosity of the root edge significantly (Fig. 6.2C), which allows instantaneous erosion. However, the compositional buoyancy and strengthening of the root interior prevents the development of a significant gravitational instability such as described by *Houseman and Molnar* [1997] and only the root material at edge of the root is sheared and eroded away. After the major plume

impact, small-scale convection dominates the underside of the normal, non-cratonic lithosphere, which also propagates to the edge of the cratonic root and causes further local erosion (Fig. 6.2D). Once the plume-affected material has cooled down, the lower part of the root returns back to approximate neutral buoyancy (Fig. 6.2E), in which thermal and compositional buoyancy cancel each other out.

6. 3. 2. Effects of chemical root: buoyancy and strength

The thermochemical erosion of a thick continental root by a plume is studied using two observables: the local geotherm and the removal of the chemical root material. Because a change in the thermal profile does not necessarily correspond directly to the removal of the chemical root, the following two physical quantities are calculated at each time step as monitors of the erosion: (1). the average thermal thickness; (2). the remaining chemical root as a percentage of its original volume. Since the main erosion takes place at the edge of the root, we monitor the erosion of the left root edge between x = 1914 km and x = 2046 km as illustrated by the black rectangular box in Fig. 6.2B.

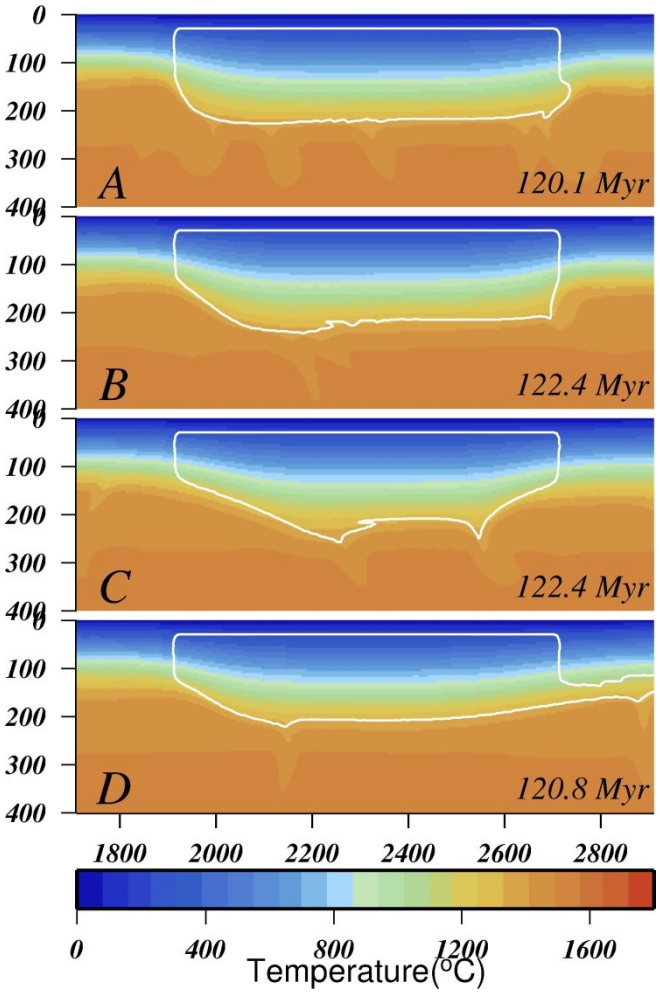

Fig.6.4: *The temperature field and chemical root shape at around 120 Myr for four models with a "strong" (A), "intermediate" (B), "weak" (C) and "buoyant"(D) root.*

Fig. 6.3 shows the average thickness (A) and remaining root percentage (B) for the left edge of the root at 50 Myr (i.e. 20 Myrs after the plume event) for 19 models with different root set-ups. Both of the two erosion monitors demonstrate that the erosive strength of the plume on the root strongly depends on the chemical buoyancy and strengthening of the root: more buoyant and stronger chemical roots experience less erosion. A "strong" root model ($\Delta\rho$ =31.5kg/m^3, $\Delta\eta$=4) shows very limited erosion (~5%), while an "intermediate" root model (with $\Delta\rho$ =21kg/m^3, $\Delta\eta$=3) shows some degree of erosion (~15%). By either reducing the buoyancy (to $\Delta\rho \leq$10 kg/m^3) or the strengthening factor (such as in the "buoyant" root model with $\Delta\rho$ =31.5kg/m^3, $\Delta\eta$=1), the erosion of the root edge would increase substantially. If both the buoyancy and strengthening factor are reduced, such as in a "weak" root model, very significant erosion (>30%) occurs (Fig 6.3A-B).

Four root models ("strong", "intermediate", "weak" and "buoyant") as defined above in Fig. 6.3B, are selected to demonstrate the evolution of the left craton root edge through time in Fig 6.3C-D. The impact of the plume arrivals around 30 Myr is clearly indicated by sudden changes of the curves in Fig. 6.3C and 3D. After the main plume impact, the average thermal lithosphere thickness grows slowly as the mantle cools down (Fig. 6.3C), while the erosion of the "chemical" root might still continue (as in most models) or slow down significantly (such as in the "strong" root model) in Fig. 6.3D. The shapes of chemical roots and thermal structures at around 120 Myr of these four models are shown in Fig. 6.4. Models with the "strong " and "intermediate" root only demonstrate local changes of the root edges by the plume impact (Fig 6.4A, B), while there are more widespread erosion effects in the other models (Fig. 6.4C, 4D).

To separate the effects of a plume impact from normal plate-mantle interaction, we also calculate three non-plume models with "strong", "intermediate", and "weak" roots and monitor the chemical root remaining for the left edge and the whole root for a much longer period of 1 Gyr (Fig. 6.5A). The thermal thickness is not monitored as it is affected significantly by cooling of the lithosphere over such a long period. The "strong" root maintained a well-shaped root (Fig 6.5B) with 99% of the original root still present. The "intermediate" strength root also survived with 92% of the root intact, albeit with significant erosion (Fig. 6.5C) at the edges. The "weak" root, however, almost completely loses its lower part after 1 Gyr with 65% and 75% of the root remaining for the left edge and the whole root, respectively. This implies that such a "weak "root would essentially not survive since its formation in Archean or Proterozoic times until today. Comparison of the erosion at the left craton edge between models with and without plume impact shows that the short term erosion with plume impact is quite similar to the long term erosion without plumes: 92.5 versus 92.8% for the "strong" root, 79.5% versus 76.4% for the "intermediate" root.

All these results demonstrate that the compositional buoyancy and strengthening of the cratonic root plays a significant role in mantle dynamics in which a plume impinges on a thick continental lithosphere. A well-preserved root seems to be characterized by being "strong" ($\Delta\rho$ =31.5 kg/m^3 and $\Delta\eta$=4), and under such conditions, the plume impact does not erode the root very much. While a less buoyant and viscous root ("intermediate" root with $\Delta\rho$ =21kg/m^3, $\Delta\eta$=3) shows significant erosion of its edge by a plume impact, the overall fractional erosion is similar to that which would occur over 1 Gyr of plate-mantle interaction without any plume impact. An even less buoyant and viscous root ("weak" root with $\Delta\rho$ =10.5kg/m^3, $\Delta\eta$=2) will not be able to survive at all, with or without a plume impact. Therefore, the effect of the plume impact is to speed up the erosion significantly over a short period (from 100s Myr to 10s Myr), but it does not necessarily induce extra erosion in the long term. This agrees well with craton stability results presented by *Sleep* [2003].

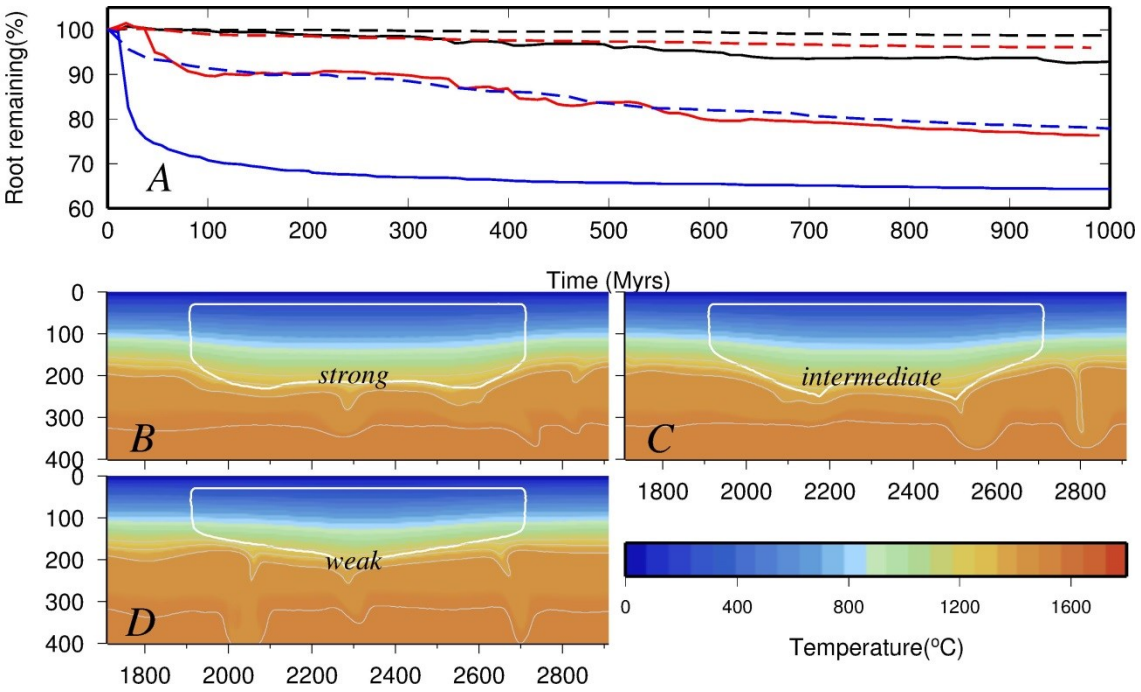

Fig. 6.5: *Results for three long duration models without a plume impact. A) The evolution of the chemical root remains over a time period of 1 Gyr for the "strong" root (black), "intermediate" root (red); and "weak" root (blue). The solid lines show the change of the root remains for the left root edge, while the dashed lines show the result for the whole root. B, C, D) The temperature field and root shape at 1 Gyr for the models with "strong," "intermediate", and "weak" root, respectively.*

6. 3. 3 Influence of plume characteristics

The effects of different plume setups are explored in this section. The temporal evolution of the average thermal thickness and fraction of chemical root remaining at the root edge is shown in Fig. 6.6. The "intermediate" root ($\Delta\rho$=21 kg/m^3, $\Delta\eta$=3) is applied in all models in this section and the default plume setup in previous models is used as the reference. A model with total plume inflow F_{total}=0 (Eq. (6.14)) shows that the root edge would still experience some erosion without any plume impact. But the total erosion after 200 Myrs (i.e. a relatively long period in comparison to a typical plume impact duration) is significantly smaller than the rapid erosion in the reference model with a plume impact. Compared to the reference model, the model with half of the total plume inflow shows much less erosion through both the average thermal thickness and chemical root remaining in Fig. 6.6A-B. However, by doubling the total plume inflow, the erosion of the root edge increases only marginally (Fig. 6.6B), although the average thickness shows a clear difference (Fig. 6.6A). Therefore, a certain critical amount of plume flux is required to erode the thick chemical root substantially and quickly, but increasing the total plume inflow beyond this critical level does not necessarily induce significantly more erosion of the chemical root if the compositional buoyancy and strengthening are unaltered. A model with a much smaller plume radius (25 km) also makes some difference. As the same total plume inflow is applied (i.e. the smaller plume remains active for longer), the change in thermal thickness of the root edge is comparable to the reference model (Fig. 6.6A), but the erosion of the chemical root decreases substantially (Fig. 6.6B). However, no obvious increase is found when an even larger plume radius is applied (not shown). This means that the instantaneous removal of the chemical root by plume impact depends on the vigor of the plume induced flow, but a threshold value of plume vigor is required for the impact to be significant.

A model with the plume rising up directly underneath the root (x=2200 km) does not show an increase of erosion (Fig. 6.6A, B). On the contrary, the average thermal thickness is similar to the model with half of the total plume inflow (Fig. 6.6A). This rather counterintuitive result can be explained by the fact that the impact of plume flow on the root is weaker when it flows from the thick lithosphere to the thin lithosphere and encounters less resistance. Such an impact would cause similar erosion at the right root edge which is not monitored in Fig. 6.6. However, the impact of the plume directly underneath the root is still distinguished, as the root remaining in Fig. 6.6B shows a small increase after the main decrease at 30 Myr. This change is due to the transition of the flow direction near the root area during the plume impact.

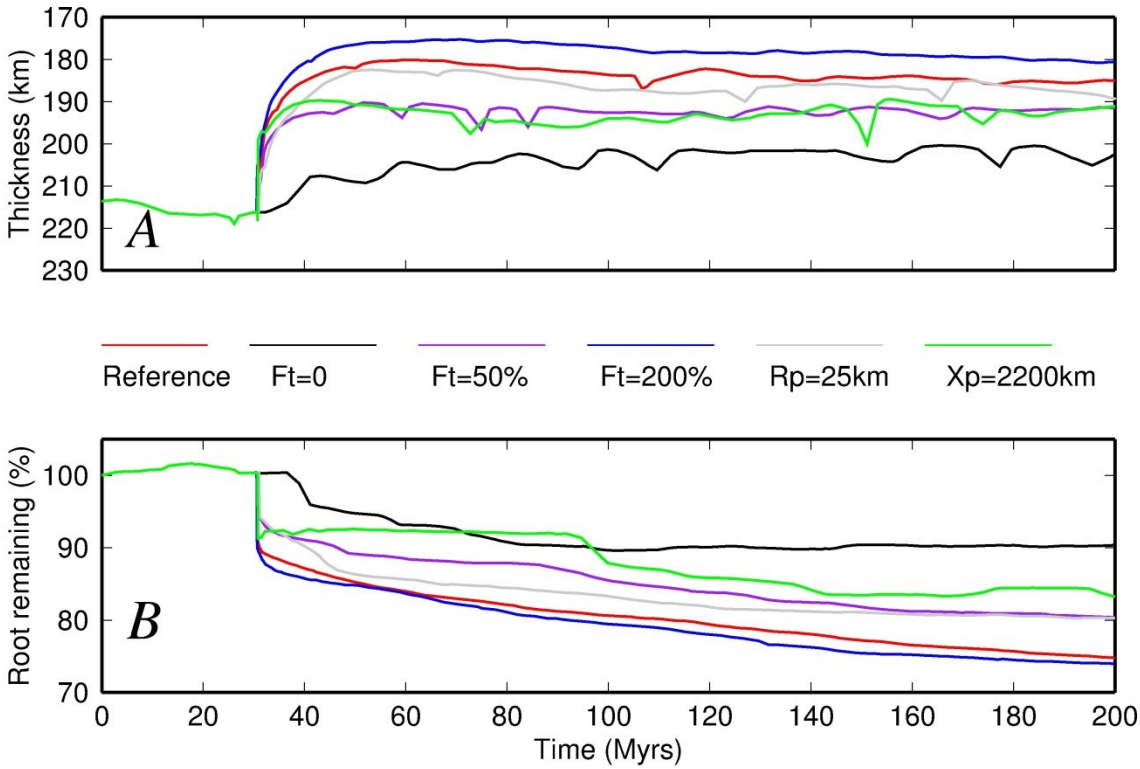

Fig. 6.6: *The evolution of thermal thickness (A) and chemical root remaining (B) over a time period of 200 Myrs for models with different plume setups. F_t, R_p, and X_p are the total plume inflow (relative to the reference case), plume radius and plume location, respectively. The reference model has X_p=1500 km, R_p=50 km, F_t=100%, while the every other model one of these parameters is changed as indicated. For F_t=0, there is no plume event in the model. For other models, the plume is at the left side of chemical root when (X_p=1500 km), except for X_p=2200 km, in which case the plume is right underneath the root as shown in Fig. 6.1A.*

Fig. 6.7 compares the long duration model in section 6.3.2 with a model in which a series of three plumes impacts the subcratonic root sideways, with plume number 1 and 3 positioned at x=1500 km and plume number 2 at the other side of the craton at x=3000 km, each with the intensity of the reference plume above. The chemical portion of the whole cratonic root is not evenly affected by the three plume impacts, though the root edge shows a clear change corresponding to every plume impact (Fig. 6.7A). The slight increase in size of the chemical root remaining at the left-side root edge indicates that plume number 2 transports root material in the direction of plume driven flow. The comparison between Fig.6.7B, D and 6.7C, 7E demonstrates that the most recent plume impact erodes and deforms the chemical root to some extent, but the long-term plate-mantle interaction would overwrite this effect. Therefore, this comparison further confirms the very limited effect on the cratonic lithosphere of thermo-mechanical erosion by mantle plumes.

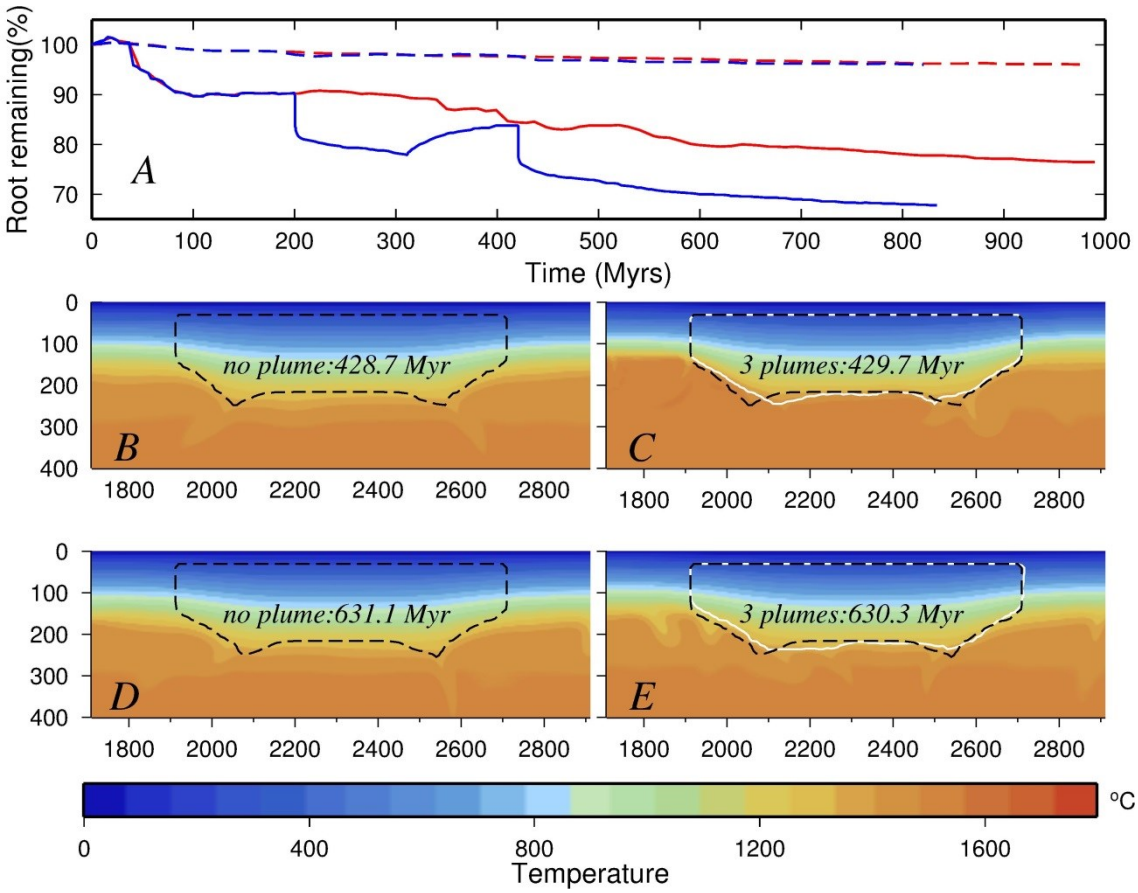

Fig. 6.7: *Results of multiple plumes experiment. A) The evolution of chemical root remains for models with no plume (red) and three plumes (blue) through 1000 Myrs. The dashed lines show the evolution of the whole craton, while the solid lines show the evolution for the left root edge. The three plumes are: 200 Myr at x=1500 km; 310 Myr at x=3000 km and 420 Myr at 1500 km. B) and D) Temperature field and root shapes (dashed lines) in the model without any plume impact at around 430 Myr and 630 Myr. C) and E) Temperature field and root shapes (white lines) in the model with 3 plumes at around 430 Myr and 630 Myr. The root shapes in B) and D) are also plotted as dashed line for comparison in C) and E), respectively.*

6.4 Discussion

6.4.1 Effect of plume impact on thick continental lithosphere.

Our modeling results illustrate that plume arrival beneath cratonic mantle has two main effects: (1) due to the stress-dependent rheology, the arrival of a strong plume-induced mantle flow deforms and weakens the continental root, especially at the root edges; (2) the hot, buoyant plume material increases the vigor of the thermochemical convection surrounding the root and causes further erosion. However, only relatively strong cratonic lithosphere would have survived since its creation in the Archean or Proterozoic.For such cratons, mechanical erosion caused by a nearby plume would be rather limited, unless the chemical root has been recently weakened. Thus, according to our results, a mantle plume is unlikely to cause short-timescale (10s of Myr) mechanical erosion of an unweakened ancient cratonic root.

Plume-craton interaction is likely to be more complicated than our (by definition simple) model calculations suggest. Plume-induced mantle depletion is not included in our models, but it might actually inhibit the thermal erosion of the root once a layer of depleted material formed at the base [*Manglik and Christensen*, 1997]. Plumes in a three-dimensional (3D) dynamic situation might exhibit different behavior compared with 2-dimensional (2D) models [*Ribe and Christensen*, 1994; *van Keken and Gable*, 1995]. However, mechanical plume erosion is not expected to be more efficient in 3D as the plume vigor would reduce with distance from the plume stem, and the 3D situation might require a more proximal plume in order to have a substantial influence on the cratonic root. Our models agree with previous work showing that a plume can reduce the width of a cratonic root [*Sleep et al.*, 2002], but they also indicate that this reduction would be rather limited for classic cratonic roots that have already survived since the Archean. The impact of a plume on a cratonic root might be stronger if widespread melts are induced by a craton-centred plume and lead to metasomatic weakening. Also the advective transport of heat by melts that penetrates the lithosphere is not included in our models and is likely to be more efficient than the thermal conduction alone at the base of lithosphere. The effects of such plume metasomatism require further geodynamic investigation with interactive feedback between melt extraction and metasomatic weakening.

6.4.2 Metasomatic weakening

Rapid, significant removal of thick continental lithosphere that previously survived billions of years of Earth's dynamic history is only likely to happen if the compositional buoyancy and strengthening of large fractions of the root are significantly altered somehow. While the thick lithospheric "lid" provided by cratonic roots limits adiabatic melting compared to that seen in shallower lithosphere, it is clear that silicate melt metasomatism strongly affects lithospheric mantle, even at the base of >150 km thick cratons [e.g., *Smith and Boyd*, 1992]. By refertilization and enrichment in garnet and/or clinopyroxene, the compositional buoyancy of originally depleted cratonic root could be removed. Carbonate-rich low degree melts generated at 6 GPa will infuse the lower-most cratonic lithosphere with phlogopite mica and carbonate [e.g., Foley, 2011]. Such water-rich melts add water both bound to metasomatic phlogopite and by diffusion into olivine. Besides weakening the lithosphere by adding water [*Peslier et al.*, 2012], any melt-rock interaction during the process of metasomatism could also have a substantial weakening effect on the rheology of the refractory continental root [*Foley*, 2008; *Holtzman et al.*, 2012], especially for local melt accumulation. Hence, even though we do not model the process and the rheological effects of metasomatism explicitly, the important geodynamical implications (i.e. a buoyancy and rheological weakening) of metasomatic refertilization on the stability of thick continental root [*Foley*, 2008; *Lee et al.*, 2011; *Tang et al.*, 2013] are manifest in our models.

Our results also show that, for the lower part of the root, there is a range of realistic cratonic compositional buoyancies (21 kg/m^3 < $\Delta\rho$ < 42 kg/m^3) and rheological strengthening ($\Delta\eta \geq 3$),

within which the thick root is not significantly affected by the mechanical erosion of mantle plumes. This suggests that a low degree of metasomatism does not necessarily change the dynamical stability of the whole continental root. As cratonic mantle is not found to be compositionally refertilized significantly on average [*Rudnick et al.,* 1998; *Pearson and Nowell*, 2002], this finding may explain why many cratonic roots are still extant, even though they might be metasomatized locally to some degree during their secular evolution. Kimberlite pipes and other small-degree melts that sample the lower parts of the lithospheric mantle only provide small local snapshots of the cratonic root at specific points in time. More detailed, widespread studies of the distribution, extent and effects of metasomatism on cratonic roots are required to fully understand the geodynamical implications of metasomatic refertilization. Nonetheless, it is clear that the extent of lithospheric weakening that occurs via high-pressure infiltration of carbonate-silicate melts at the base of the cratonic mantle depends on the intensity and spatial extent of the metasomatic events.

6.4.3 Global implications

As discussed above, our numerical models clearly demonstrate the effects of both plume impact and metasomatic refertilization on the erosion of the subcontinental lithosphere during mantle thermal events. The models thus may have important implications for continental dynamics, including the cause of continental breakup and lithosphere thinning. Lithosphere thinning has been suggested for a number of Precambrian terranes [*Lee et al.*, 2011], and here we choose thinning of the lithosphere underneath Gibeon, southern Africa, the destruction of North China Craton (NCC) and the breakup of the North Atlantic Craton as three examples that highlight the global relevance of the presented numerical model results.

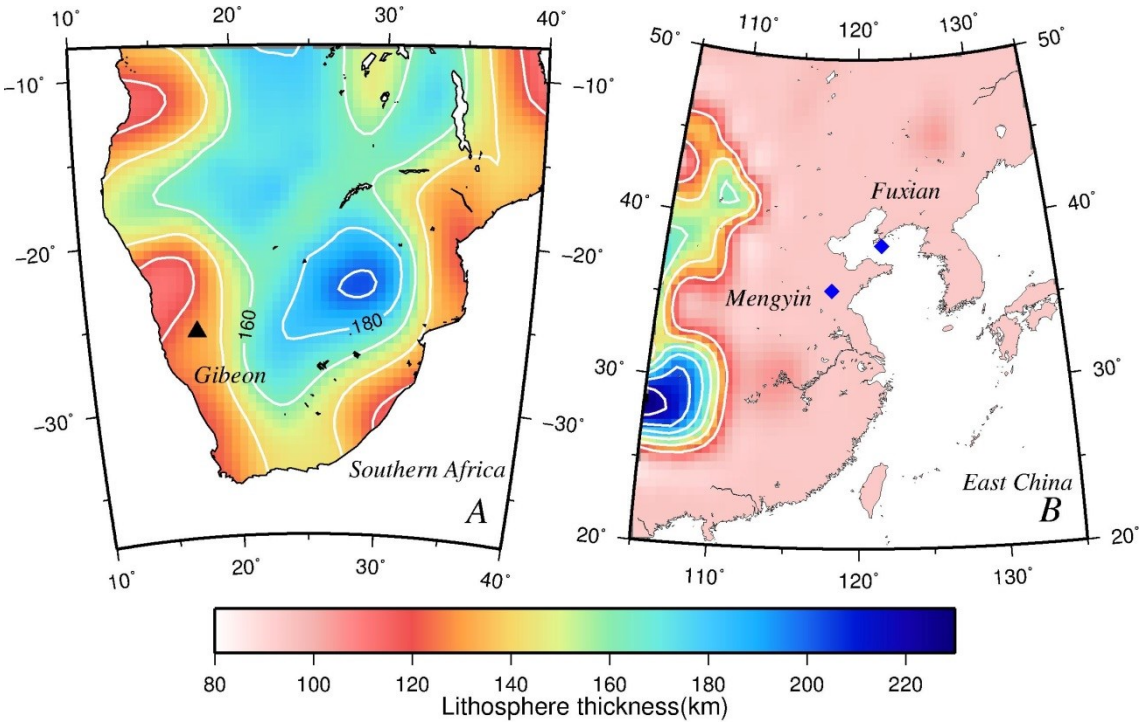

Fig. 6.8: *Comparisons of current thicknesses from global seismic study [Priestley and McKenzie, 2013] and paleo-thickness from kimberlites at southern Africa [Mather et al., 2011] and the North China Craton (NCC) [Menzies et al., 1993]. These comparisons have indicate removals of lithosphere by ~40 km for Gibeon, Southern Africa and by ~120 km for NCC.*

6.4.3.1 Lithosphere thinning beneath southern Africa

Kimberlite-derived mantle xenoliths show that the Proterozoic lithosphere underneath Gibeon, Namibia in southern Africa used to have a similar geotherm to the Kaapvaal craton at 70 Ma, which indicates a lithosphere thinning of 40-50 km to reach the current lithosphere thickness (Fig. 6.8A) of this area [*Bell et al.*, 2003; *Boyd et al.*, 2004; *Mather et al.*, 2011; *Priestley and McKenzie*, 2013]. Given the multiple plume tracks across southern Africa starting at 44 Ma [*O'Connor et al.*, 2012], lithospheric thinning by mantle plume erosion seems to be a good candidate for this thinning event. However, according to our model results, a rather sudden significant thinning of this lithosphere after its long-term survival since Proterozoic times [*Pearson et al.*, 2004] until at least 70 Ma requires a substantial, recent weakening event. This indicates that some metasomatic weakening must have occurred relatively shortly before or during the plume arrival. Multistage metasomatism has indeed been documented since 170 Ma, including the Group I (108-74Ma) and Group II (143-117Ma) kimberlite eruptions [*Konzett et al.*, 1998; *Griffin et al.*, 2003a; *Becker and Le Roex*, 2006; *Gibson et al.*, 2008; *Kobussen et al.*, 2008]. Therefore, we conclude that these documented metasomatism events must have played a very important role in the weakening of the lithosphere mantle, while the recent plume events may help the thinning to occur rapidly after the weakening.

6.4.3.2 Destruction of the North China Craton

The destruction of the eastern part of the North China Craton (NCC) has attracted a lot of attention as the only undisputed example of the almost complete removal of the cratonic root [*Zhu and Zheng*, 2009]. The dramatic loss of >120km of lithosphere was first demonstrated by *Menzies et al.,* [1993] who noted the difference in equilibration depths given by deeply derived garnet-peridotites from Ordovician kimberlites versus the shallow depth of lithosphere in the Cenozoic indicated by spinel peridotites erupted by alkali basalts. The shallow present-day lithospheric thickness is confirmed by seismic tomography (Fig. 6.8B). The survival of this cratonic root from the Archean to the Mesozoic suggests an initially strong cratonic root that could resist long-term thermo-mechanical erosion by interaction with the mantle. Our model results suggest that the relatively sudden removal of this cratonic root requires a recent, significant weakening of more than perhaps 100 km cratonic lithosphere. This unusual requirement has also been suggested by the geodynamic modeling of subduction-related convective erosion of the NCC [*He et al.,* 2014]. A dehydrating stagnant slab underneath east Asia has been suggested to initiate the upwelling of "wet plumes" [*Richard and Iwamori*, 2010] or the formation of a large mantle wedge [*Zhao et al.*, 2009, *He et al.* 2014]. A recent find of hydrous ringwoodite trapped in diamond [Pearson et al., 2014] confirms the enhanced water-carrying capacity of the transition zone. In this scenario, water originating from stagnant slabs in the transition zone that are heating up acts to lowers the solidus of mantle rocks, producing large amount of melts that metasomatize the cratonic root through fluid/melt-rock interaction (hydrous metasomatism) [*Niu et al.,* 2005]. In addition, water or hydrous fluid at the subduction zone might also can trigger the eclogitization of the lower crust [*Jackson et al.*, 2004; *Krystopowicz and Currie*, 2013] and provide the negative buoyancy required for foundering of the lower crust as well as the mantle lithosphere underneath [*Gao et al.*, 2002a; *Yu et al.*, 2012]. The gravitational instability of the chemically buoyant lithosphere [*Jaupart et al.*, 2007; *Wang et al.*, 2015] provides a supportive mechanism of the destruction of the NCC. *Wang et al.* [2015] demonstrated the feasibility of episodic and multistaged gravitational instabilities of the weakened cratonic lithosphere consistent with the episodic magmatism/volcanism events of the NCC in the Mesozoic and Cenozoic. We note that, regardless of the exact mechanism, significant weakening by hydrous metasomatism and related processes must have played an essential role in the sudden destruction of the NCC and is consistent with our model results that emphasize the role of metasomatic weakening.

6.4.3.3 Rifting of the North Atlantic Craton and opening of the Labrador Sea

Our last example highlights the role played by exotic small-degree volatile-rich melts in weakening the base of cratonic mantle over an extended time period prior to full-scale continental rifting. The continental breakup phase during the supercontinent cycle is often linked to plume impingement [*Hill*, 1991; *Anderson*, 1994; *Courtillot et al.*, 1999; *Li and Zhong*, 2009; *Brune et*

al., 2013; *Yoshida*, 2013]. *Brune et al.* [2013] studied the thermal and mechanical influence of a plume on 3D continent breakup and found that a plume would reduce the strength of continents by several TN/m if tens of kilometers of lithosphere are eroded from the base of the continental lithosphere. Continental root erosion by mantle plumes without weakening of the originally stable lithosphere, however, is found to be very limited according to our modeling results. But (potentially plume-generated) melt weakening effects in the lithosphere assist the process of continental rifting [*Buck*, 2006; *Schmeling and Wallner*, 2012]. The North Atlantic Craton, exposed on the W and E sides of the Labrador Sea was rifted apart between 60 and 55 Ma, accompanied by the eruption of flood basalts. Prior to this, the cratonic root experienced a protracted history of metasomatic weakening that began with the eruption of Mesoproterozoic lamproites through deep ancient cratonic lithosphere followed by Neoproterozoic ultramafic lamprophyres in both Labrador and W. Greenland [*Tappe et al.*, 2007, 2011]. This magmatism infused the lower lithosphere with carbonate and water at this time. Initially small-scale (~30 km depth) lithosphere removal appears to have accompanied the eruption of alkalic melts during the Jurassic [Tappe et al., 2007], probably driven by small-scale convective flow whereas the arrival of a major plume at 60-55Ma drove full-scale continental rifting of the metasomatically weakened lithosphere. This sequence of metasomatic weakening and thermomechanical erosion by small and large-scale mantle flow is aligned with our model results.

6.5 Conclusion

The hypothesis that a mantle plume might cause significant thinning of ancient, depleted continental mantle lithosphere is tested in our numerical models. The results show that the erosion caused by a plume impact on a strong continent (moderately strong and buoyant) is rather limited. Plumes impacting on less strong or less buoyant subcontinental roots produce significantly more erosion at root edges in a relatively short (approximately 10s of Myrs) amount of time. Without such a plume impact, a similar amount of erosion could eventually occur due to continued plate-mantle interaction, albeit over much longer time scales (several 100 Myrs to 1 Gyr). Varying the plume radius, location, or total plume inflow does not significantly change the effectiveness of the erosion. Instead, our modeling shows that generating a distinctly weakened root (less strong and less buoyant) is essential for significant thinning of subcontinental lithosphere over timescales of a few 10s of Myr.

Fluid/melt-rock interaction during mantle metasomatism is probably the most likely mechanism to modify and weaken the depleted subcontinental lithosphere. Therefore, metasomatic weakening must have played an essential role on the thinning and reactivation of the originally stable subcontinental lithosphere, while the effect of any plume impact was to speed up the erosion and helped the removal of the lithospheric root to occur rapidly after the weakening. Depending on the extent of the metasomatic weakening, as well as the tectonic environment, dif-

ferent types of reactivation of the subcontinental lithosphere may occur, such as thinning of subcontinental lithosphere (e.g. underneath southern Africa), complete destruction of the cratonic root (e.g at the NCC) and continental rifting (e.g. of the NAC). For the cases of southern Africa and the NAC, the documented plume activity may have enabled this process to occur rapidly. Other Precambrian terranes (e.g. the Colorado plateau and Wyoming craton) may have undergone similar processes, but more detailed studies of the distribution, extent and effects of metasomatism might be needed to confirm this.

Acknowledgments

We thank Keith Priestley and Kathy Mather for kindly providing data and Mark Allen and Antoine Rozel for useful discussions. We also thoroughly appreciate the constructive reviews from Sally Gibson, Shijie Zhong and the (Associate) Editors. The data for this paper are available by contacting the corresponding author. The work has been supported by EU FP7 Marie Curie Initial Training Network "Topomod," contract No. 264517 (HW). JvH acknowledges funding from the European Research Council (ERC StG 279828) and DGP was supported by a Canada Excellence Research Chair.

Chapter 7

Thickening and stabilization of cratonic lithosphere in a thermally evolving mantle

Abstract

The formation mechanism for the Archean craton is still enigmatic, as showed by the strong debate on the plume related versus the subduction related origin. The latest evidence from both geophysical and petrological approaches, however, both suggest a vertical thickening of the cratonic peridotite after its formation. This study therefore focuses on the thickening process of craton formation in a thermally evolving mantle by using geodynamical modelling. Our numerical experiments demonstrate a cratonization process in which a depleted buoyant layer (30~120 km) forms a cratonic root that is thicker than 200 km within a few hundreds of Myr. Our results show that substantial initial tectonic shortening and thickening of previously depleted material is essential to initiate the cratonization process. This could perhaps have been caused by tectonics similar to today's orogenic processes associated with phenomena such as subduction accretion, lithosphere underplating, or continental collision. The Tibetan Plateau serves as a good tectonic modern-day analogue of such a thickening process, though it may not form a craton. Gravitational self-thickening takes place after the initial tectonic compressive shortening and it contributes to a second thickening regime. Unlike previous gravitational instability studies, the intrinsic compositional buoyancy of the cratonic root, as well as the secular cooling of the mantle, prevents a Rayleigh-Taylor type collapse, and stabilizes the thick cratonic root. So our models provide a possible cratonization scenario that is consistent with petrological and geophysical constraints.

7.1 Introduction

Cratons, the geologically oldest parts at the surface of our earth, owe their longevity and stability to the chemical distinction of highly melt-depleted cratonic roots [Jordan, 1975, Boyd, 1989; Carlson et al., 2005; Wang et al 2014]. The formation of this chemically distinctive root, however, continues to be strongly debated, with more and more information about cratonic lithosphere becoming available through recent scientific and technological advances [e.g. *Griffin et al.*, 2003b; *Carlson et al.*, 2005; *Pearson and Wittig*, 2008; *Lee and Chin*, 2014].

Three main endmember hypotheses for the formation of cratonic lithosphere have been proposed [*Pearson and Wittig*, 2008; *Arndt et al.*, 2009; *Lee et al.*, 2011]: 1. extensive melting in a mantle plume; 2. accretion and stacking of oceanic lithosphere; 3. accretion of the arc lithosphere. There has been much debate regarding relative importance of mantle plume origin and subduction related origin [*Lee*, 2006; *Aulbach*, 2012; *Pearson and Wittig*, 2014]. However, even though no current single hypothesis is able to explain all the observations of modern cratons, two aspects of the craton formation seem to be commonly acknowledged [*Carlson et al.*, 2005; *Lee and Chin*, 2014; *Pearson and Wittig*, 2014]: 1. delamination of eclogite (i.e. fate of abundant eclogite); 2 compressional thickening of buoyant root/depleted mantle. The "evolved", andesitic continental crust has a different average composition from the basaltic crust generated at present day crustal growth sites [*Rudnick*, 1995; *Liu and Rudnick*, 2011], which has been referred to as the "crust composition paradox". As one of the main ways to solve this paradox, the delamination of eclogite has been commonly discussed in the theories of craton formation [e.g. *Zegers and van Keken*, 2001; *Griffin et al.*, 2003; *Carlson et al.*, 2005; *Bédard*, 2006; *Rollinson*, 2010; *Tappe et al.*, 2011; *Aulbach*, 2012; *Herzberg and Rudnick*, 2012; *Lee and Chin*, 2014]. However, the dynamics associated with compressional thickening during craton formation (probably related to Wilson cycle) is comparatively less studied [*Rapp et al.*, 2003; *Mckenzie et al.*, 2005; *Rollinson*, 2010; *Pearson and Wittig*, 2014], though it has long been proposed as an important process of cratonization [*Jordan*, 1978], and vertical tectonics might have played a more important role in the Archean that it does today [*Bédard et al.*, 2003; *Sleep*, 2005]. Thus, we will focus on the dynamics of the thickening process of cratonic lithosphere in the Archean-like environment in this study.

The melting depth of the peridotitic protolith is one of the key constraints for formation of cratonic peridotite [*Herzberg*, 1999; *Canil*, 2004; *Pearson and Wittig*, 2008, 2014; *Lee and Chin*, 2014]. High pressure (3-6GPa) melting conditions of craton protoliths obtained from bulk-rock major element studies are used as evidence for a plume origin [e.g. *Pearson et al.*, 1995; *Herzberg*, 1999; *Aulbach*, 2012], although this approach does not consider later metasomatic processes [*Lee*, 2006; *Pearson and Wittig*, 2008]. In contrast, mildly incompatible trace element results that are insensitive to metasomatic processes argue for a low pressure origin of cratonic

peridotite (<3 GPa) [*Canil*, 2004; *Wittig et al.*, 2008]. *Lee and Chin* [2014] explicitly calculated the temperature and pressure conditions of peridotite melting events through bulk FeO and MgO measurements of the residual peridotite. Fig. 7.1 shows the comparison between the subsolidus equilibration P-T status and the calculated P-T condition of the igneous protolith of selected cratonic peridotite samples. They concluded that Archean cratonic peridotites are likely to be formed at melting temperatures of 1400-1750^{o}C and pressures of 1-5GPa (~30-150 km) and then transported to depths of 120-200 km and cooled (Fig. 7.1). The driving force for the vertical movement of cratonic peridotite is either an external tectonic force or the internal gravitational force. The numerical study of the secular thermal evolution of the cratonic lithosphere demonstrated that the isopycnic state of the cratonic lithosphere is an inherently ephemeral phenomenon due to the evolution of the negative thermal buoyancy [*Eaton and Claire Perry*, 2013]. Laboratory experiments on the physical properties of depleted mantle rocks further suggest that subcratonic mantle formed above ~110 km is negatively buoyant with respect to adiabatic mantle [*Schutt and Lesher*, 2006], which suggests a gravitational driven vertical movement.

Geodynamical modelling of the thickening process of depleted mantle rocks is required to know how a craton grows to its current thickness and may help us gain new insights for some geological phenomena. *Cooper and Miller* [2014] studied the thickening of the buoyant material over a mantle downwelling and suggested that mid-lithospheric discontinuities might be related to the localized deformation during the thickening phase of the cratonic lithosphere. In this study, we perform new numerical experiments to investigate the thickening process of cratonic lithosphere in a thermally evolving mantle and explore the potentially important model parameters related to the craton thickening and stabilization.

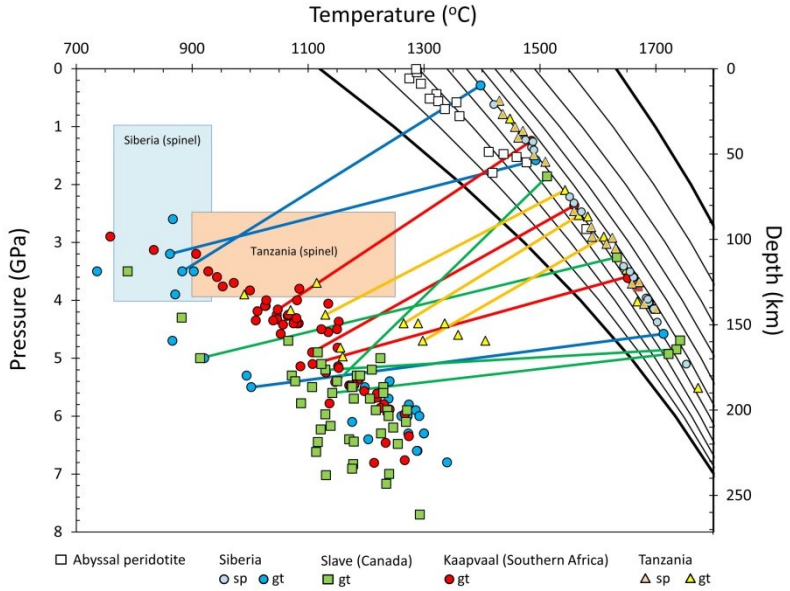

Fig. 7.1: *P-T plot for cratonic peridotite with both igneous protolith and metamorphic, subsolidus conditions (Lee and Chin [2014]). The lines connect protolith and metamorphic P-T conditions for those samples for which both sets of P-Ts could be calculated. They indicate a downward vertical movement of these rock samples as a consequence of root thickening during cratonization.*

7.2 Model description

7.2.1 Governing equations

We use a Cartesian version of the finite element code Citcom [*Moresi and Solomatov*, 1995; *Zhong et al.*, 2000; *van Hunen et al.*, 2005] to solve the incompressible flow with Boussinesq approximations. The non-dimensional governing equations for mass, momentum, energy conservation are:

$$\nabla \cdot \mathbf{u} = 0 , \tag{7.1}$$

$$-\nabla P + \nabla \cdot \left(\eta\left(\nabla \mathbf{u} + \nabla^{T} \mathbf{u}\right)\right) + \left(RaT - Rb_{i} C_{i}\right)\mathbf{e}_{z} = 0 , \tag{7.2}$$

$$\frac{\partial T}{\partial t} + \mathbf{u} \cdot \nabla T = \nabla^{2} T + Q_{0} . \tag{7.3}$$

A standard non-dimensionalisation is used with $x = x'h, t = t'h^{2}/\kappa, \eta = \eta'\eta_{0}$,while the primes of the non-dimensional parameters are dropped for clarity in the above equations. The dimensional physical parameters are listed and explained in Table 7. 1. The thermal and chemical Rayleigh number *Ra* and Rb_i are defined as:

$$Ra = \frac{\alpha \rho_0 g \Delta T h^3}{\kappa \eta_0}, \tag{7.4}$$

$$Rb_i = \frac{\delta \rho_i g h^3}{\kappa \eta_0}. \tag{7.5}$$

A particle-tracking technique is used to track different chemical materials[*van Hunen et al.*, 2000; *Di Giuseppe et al.*, 2008], which has been benchmarked against *van Keken et al.* [1997] and *Schmeling et al.* [2008]. The evolution of the compositional field is solved with:

$$\frac{\partial C_i}{\partial t} + \mathbf{u} \cdot \nabla C_i = 0, \tag{7.6}$$

where C_1,C_2 represent the crust and depleted mantle material, respectively. Considering the significant shortening of both crust and mantle lithosphere in our models, here we use a different rheology for the crust in order to take into account the potentially important effects of the weak and buoyant crust. A critical value of C_1 is set up in order to distinguish between the crust and mantle when the viscosity is calculated. We use a composite rheology of dislocation creep and diffusion creep that is similar to Chapter 6, but we ignore the pressure dependence of the rheology in order to simplify the models and focus on the lithosphere dynamics. The composition-dependent viscosity for dislocation creep and diffusion creep are defined as:

$$\eta_{dl} = A^{-\frac{1}{n}} \dot{\varepsilon}^{(\frac{1-n}{n})} exp\left(\frac{E}{nRT}\right) \times \Delta\eta, \tag{7.7}$$

$$\eta_{df} = Bexp\left(\frac{E}{RT}\right) \times \Delta\eta^{n}. \tag{7.8}$$

In addition, we apply a yielding mechanism [*van Hunen and Allen*, 2011] to consider the brittle yielding of strong lithosphere during the imposed shorting process:

$$\eta_y = \frac{\min(\tau_0 + \mu P, \tau_{max})}{\dot{\varepsilon}}, \tag{7.9}$$

whereas the descriptions of the parameters are listed in Table 7.1. Therefore the effective viscosity is defined as:

$$\eta_{eff} = \min(\eta_{dl}, \eta_{df}, \eta_y). \tag{7.10}$$

Table 7.1 Symbols, units and default parameters.

Symbol	Description	Default value and units
A	rheological pre-exponent	[$MPa^{-n}s^{-1}$] (ds), [MPa^{-1}) (df)
E	mantle activation energy	500 (ds), 310 (df) [kJ/mol]
Ec	crust activation energy	375 (ds), 260 (df)
g	gravitational acceleration	9.8 [m/s^2]
h	model height	400 [km]
C_p	Thermal capacity	1250 [$J\ kg^{-1}K^{-1}$]
n	rheological power law exponent	3.5, 3.4 (ds), 1 (df) [-]
P	deviatoric pressure	[Pa]
R	gas constant	8.3 [J/mol]
Ra	thermal Rayleigh number	$1.1228x10^6$ [-]
Rb_i[a]	compositional Rayleigh number	$3.7632x10^6$, $1.9757x10^5$ [-]
T	Temperature	[^0C]
ΔT	temperature drop over model domain	1350 [^0C]
$\dot{\varepsilon}$	strain rate	[s^{-1}]
A	thermal expansion coefficient	$3.5x10^{-5}$ [K^{-1}]
η_0	reference viscosity	10^{20} [Pa·s]
η	viscosity	[Pa·s]
κ	thermal diffusivity	10^{-6} [m^2/s]
ρ	mantle density	3300 [kg/m^3]
$\Delta\rho_1$	density difference of crust and mantle	600 [kg/m^3]
$\Delta\rho_2$	maximum density change due to depletion	31.5 [kg/m^3]
Q_0	present day mantle radioactive heating	0.02 [$\mu W/m^3$]
C_i	composition field	0~1 [-]
$C\eta$[b]	rheologically effective composition value	0.6 [-]
τ_0	yield stress at the surface	40 [MPa]
τ_{max}	maximum yield stress	400 [MPa]
μ	friction coefficient	0.6 [-]
P_0	lithostatic pressure	[Pa]

[a] $3.7632x10^6$ and $1.9757x10^5$ are the compositional Rayleigh numbers for crust and cratonic root, respectively.

[b] $C\eta$ is chosen to make the second cratonic layer has the maximum strengthening factor due to its initial compositional field.

Different rheological parameters are applied to the crust and mantle as listed in Table 7.1. For the crust rheology, there is no strengthening factor ($\Delta\eta$=1). For the mantle rheology, a strengthening factor of $\Delta\eta$=3 is used in Eqs. (7.7) and (7.8) for the depleted cratonic root areas. Due to the non-linear stress-strain rate relationship used in the non-Newtonian rheology, the effective compositional viscosity increase depends on the ambient stress or strain rate. In this study, we report 'constant strain rate' values $\Delta\eta$, and values used in this study ($\Delta\eta$ = 3) correspond to 'constant stress' values of $\Delta\eta^n$ = 46.8, for n=3.5. The choice of $\Delta\eta$ = 3 is based on the study of Chapter 5 and 6 and it is well within the range of acceptable values obtained from laboratory measurements [*Hirth and Kohlstedt*, 1996; *Karato*, 2010; *Fei et al.*, 2013].

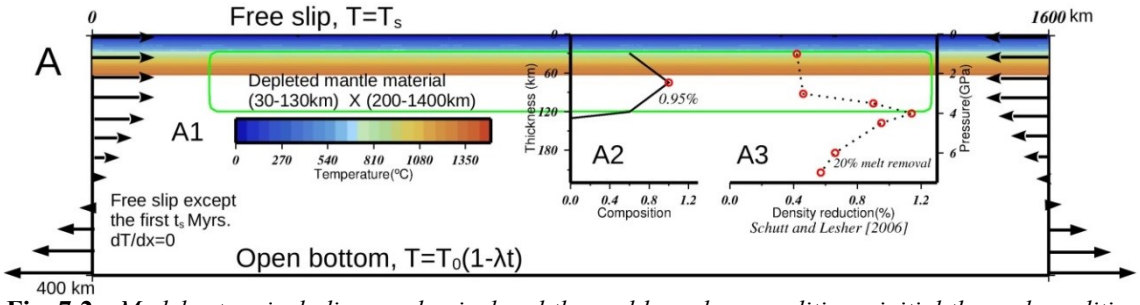

Fig. 7 2: *Model setup, including mechanical and thermal boundary conditions, initial thermal condition and initial chemical profile of the cratonic root. The initial compositional profile C, as plotted in the left inset diagram A2, increases from 0.6 to 1 between 30 km and 75 km and decreases from 1 to 0.6 between 75 km and 120 km. The chemical buoyancy reaches its maximum value at 75 km, where it is 0.95% less dense than typical 3300 kg/m^3 reference density for peridotite. For comparison, the depth-dependent depletion effect for 20% melting on the density of mantle peridotite is plotted in the right inset diagram A3 [Schutt and Lesher, 2006].*

7.2.2 Model setup

The computational domain is 400 km deep and 1600 km wide, with the layered depleted mantle material at located between x=200 km and x=1400 km. This model setup is illustrated in Fig. 7.2, together with the mechanical and thermal boundary conditions. The side boundaries of computation domain have an imposed constant in/outflow velocity profile as shown in Fig. 7.2 which pushes the lithosphere towards the centre of the domain for a given period. This process shortens the lithosphere with the chemical root as well as the remaining lithosphere in the model domain and could potentially form a thick cratonic root. The shortening of the lithosphere is mainly controlled by the imposed boundary inflow velocity and duration, and we define a shortening length as:

$$L_s = 2 \times V_s \times t_s \,. \tag{7.11}$$

So strictly speaking, this shortening length L_S represents the amount of lithosphere pushed into the model domain from two side boundaries. It is 1000 km in the reference model L (see Table 7.2). After the compressive shortening phase, free slip boundary conditions are applied at

the side boundaries. The bottom boundary is open to allow material to flow in or out of the model domain. We ignore any initial thermal differences between the depleted mantle and normal mantle, and use a 30 Myrs halfspace cooling age for the initial thermal structure of the whole lithosphere as shown in Fig.7.2. We define the thermal lithosphere asthenosphere boundary (LAB) as the T=1350^{0}C isotherm. As we aim to model the thickening of cratonic root in the hotter Archean era, we use a mantle potential temperature of 1550^{0}C in the models, which is well within the range of petrological estimates [*Herzberg et al.*, 2010]. The first order effect of mantle secular cooling is included by a constant cooling rate λ (^{0}C/Gyr) for the temperature boundary condition at the bottom, as described by:

$$T_b = T_{b0}(1 - \lambda t) \tag{7.12}$$

Secular cooling of the Earth's mantle has been estimated to be 50-100 ^{0}C/Gyr [*Schubert et al.*, 1980; *Grove and Parman*, 2004; *Michaut and Jaupart*, 2007; *Herzberg et al.*, 2010]. In order to highlight/protrude the effects of the secular cooling, we use λ =100 ^{0}C/Gyr in the reference model, but we also explore the effects of different cooling rates in section 7.3.2.3. The depleted mantle material is composed of two layers: 1) a highly depleted layer from 30 to 75 km depth; and 2) a less depleted layer from 75 to 120 km with compositional value decrease from 1 to C_η. The effects of melt depletion on the mantle density has been suggested to be smallest at pressures between 1 and 3 GPa, within which 20% melt removal results in only a 0.42% ~0.46% density reduction (Fig.7.2A3)[*Schutt and Lesher*, 2006]. Thus, even though the depletion profile ideally decreases with depth, the chemical buoyancy may peak within the depleted layer because of the depth-dependent effects of depletion on density. Instead of considering a complicated depth-dependence of depletion on density, we simply use a chemical profile as illustrated in Fig. 7.2A2 to mimic its effects. To avoid the sharp transition between chemical root and asthenosphere, a 10-km thick buffer layer is added underneath the chemical root in which the chemical value gradually decreases to 0. This profile results in a maximum chemical buoyancy at 75 km(C=1) in the initial chemical field, which would transport to deeper mantle during the thickening of the root. We use a maximum density reduction of 31.5 kg/m^3 (0.95%) in our models, which is within the range 0.90%~1.14% where the depletion has maximum effects on the density under the pressure 3.5~4.5 GPa [*Schutt and Lesher*, 2006]. This value also agrees with the results in Chapter 5 and 6. More or less density reduction would have significant effects on the stability of the cratonic root as discussed in the previous chapters. In this chapter, we simply use 0.95% as default value, and focus more the effects of other model parameters. The composition value C controls both the buoyancy and strengthening of continental root through:

$$\rho_c = \rho_m - C_i \Delta \rho_i \tag{7.13}$$

$$\Delta\eta = \Delta\eta_0^{\,min(1,\frac{C_2}{C_\eta})} \tag{7.14}$$

Because the two chemical layers in all calculations have initial compositional values larger than or equal to Cη, the initial strengthening factor of the whole root is always $\Delta\eta_0$ in Eqs. (7.7) and (7.8). Besides the rheology and buoyancy of the crust, the high radiogenic heating in the crust may also play a role in the lithosphere dynamics during the shortening of the lithosphere. We made the following assumptions: 1. a constant ratio of 30 of the radiogenic heating between the crust and mantle; 2. The heat production in the Archean is 3 times of the present-day value based using exponential decay with a half-life of 1.8 Gyrs for both the crust and mantle. These assumptions fall within the suggested ranges for the Earth's thermal evolution and heat production values [*Mareschal and Jaupart*, 2006; *Michaut and Jaupart*, 2007; *Michaut et al.*, 2009]. The crustal rheology and radiogenic heating may have significant influence on the lithosphere dynamics, especially shortly after the imposed shortening in our models. But as we focus on the long-term thickening and stabilization of the cratonic root, we did not vary these crustal parameters, and as such, their effects on craton formation are not explicitly examined in this study.

A total of 96-by-394 finite elements are used, which provides a uniform spatial resolution of 4.17 km per element. A total number of ~1 million tracers are randomly distributed in the domain at the beginning of the computation, which provides an average tracer density of 25 tracers per element. In order to handle the tracer inflow and outflow, tracers at the elements facing any open boundaries are refreshed at every time step. Thus, the total number of tracers in the computation domain is statistically constant. The tracer velocity interpolation is done with the method described in Chapter 4.

7.3 Numerical modelling results

7.3.1 Thickening process of the cratons

Fig. 7.3 demonstrates the general thickening process of cratonic root in our reference model L (Table 7.2). A layer of thin depleted mantle material grows to a thick cratonic root in a few 100s of Myrs after 50 Myrs of the compressive shortening. The green contour outlines the depleted mantle material. As the area with T>1350^{0}C is removed, the temperature images actually show the thermally defined lithosphere. Hereafter, we refer the areas showed by the temperature image and chemical contour (green) as the thermal root and chemical root, respectively. The thickness of the cratonic root is monitored through time as the average depth extent of the chemical root (defined as the depth of the green contour in Figure 7.3) between x=550 km and x=1050 km. We also calculate the amount of remaining root defined as the remaining percentage of the original chemical root volume to monitor its erosion. The results of four models are shown in Fig. 7.4 with the red lines indicate the evolution of average root thickness (Fig. 7.4A) and remaining root (Fig. 7.4B), respectively.

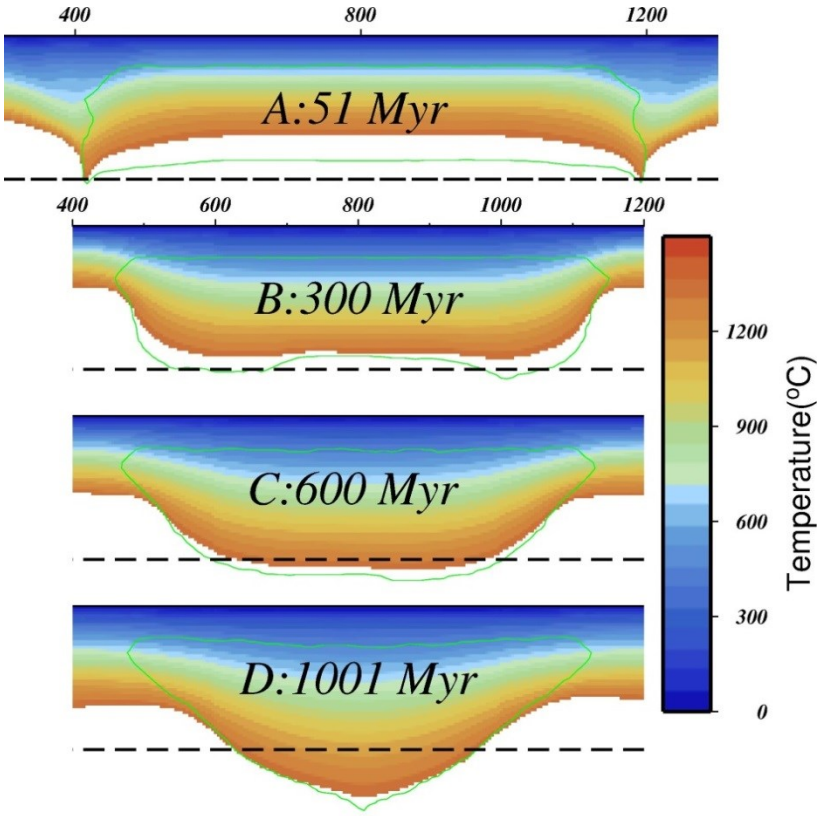

Fig. 7.3: *The thickening process of the cratonic root in the reference model L. The initial thermal status and chemical field are shown in Fig. 7.2. Colours indicate the temperature distribution, from which temperatures above 1350°C (taken as the 'thermal root' in this study) are removed to clarify the lithosphere thickening process. The dashed black lines show the depth of 200 km. The green lines depict the cratonic root with chemical contours. These rules also apply to the following figures with temperature images.*

There are two regimes of the thickening process: 1) the quick compressional tectonic shortening imposed by the velocity at the two side boundaries, for $t < 50$ Myrs in this case, and 2) the self-driven gravitational thickening of the pre-thickened root after $t = 50$ Myrs. As constant inward velocities are imposed at both side boundaries, the depleted root material in the middle of the domain is pushed downward to the deeper mantle which causes the initial thickening and shortening of the cratonic root (Fig. 7.2 and 7.3A). As the depleted mantle material is compositionally buoyant and viscous compared to normal mantle, it resists this thickening process, which results in more thickening at the edge than at its interior (Fig. 7.3A). In this case, the depleted root material is thickened from 120 km to about 175 km depth within 50 Myrs (Fig. 7.2 to 7.3A), while the thermal root is significantly thinner. The resultant thermal and chemical structure after the imposed compressional thickening ceases is by no means in steady state. When the thickened root cools down and becomes denser, the negative thermal buoyancy exceeds the chemical buoyancy and causes further thickening. In this phase, the cratonic root grows from 175 km at $t = 50$ Myrs to 220 km depth at $t = 600$ Myrs (Fig. 7.4A), during which the thermal root grows to approximately the same depth as the chemical root (Fig. 7.3A-C). This self-driven gravitational thickening is controlled by the cooling of the cratonic lithosphere

and thus it has similar timescale as that of the thermal diffusive cooling of the lithosphere. Both of the two thickening regimes involve some recycling of the root material as illustrated in Fig. 7.4B: ~17.5% during the compressive thickening regime and another ~5.5% during the self-driven thickening regime. The cratonic root still slowly thickens and shortens as a result of the deformation after 600 Myrs (Fig. 7.3C-D), but almost no chemical root recycling occurs as indicated by Fig. 7.4B. This indicates that the buoyancy and high viscosity of the depleted root prevent the development of a significant Rayleigh Taylor instability and stabilizes the root in the long term.

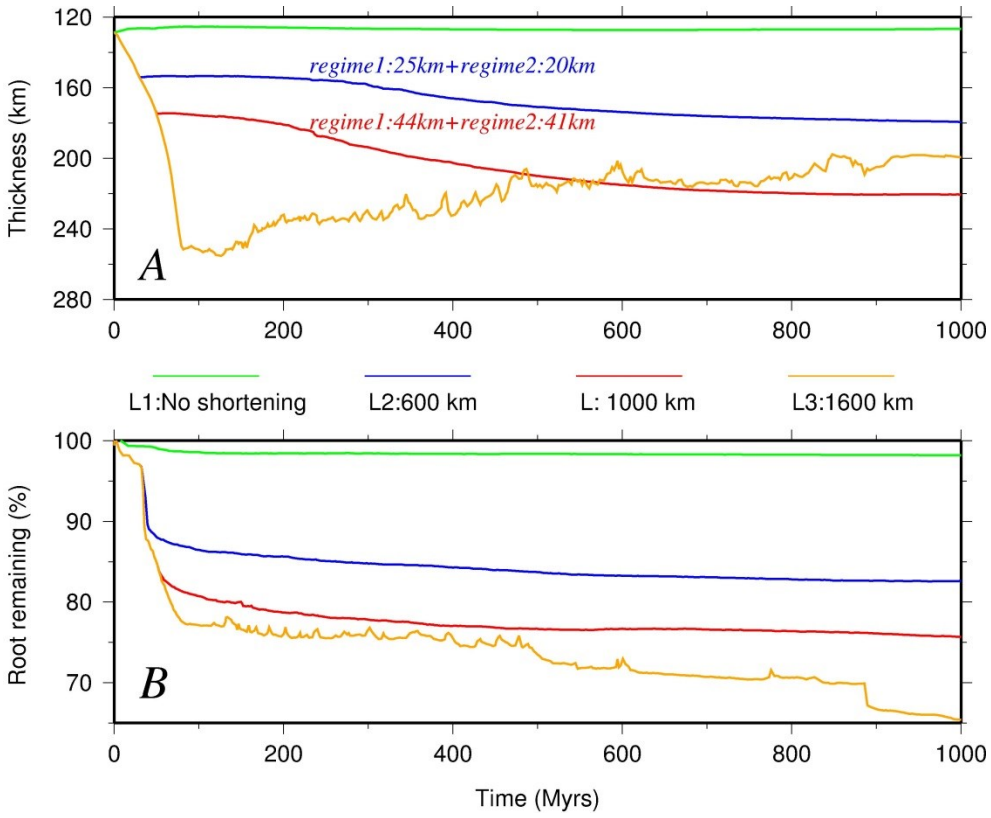

Fig.7. 4: *A) Thickening of the cratonic roots over a time period of 1000 Myrs, measured as their average thickness between x=550 km and x=1050 km in models with different shortening lengths. The thickness is calculated by using the compositional (rather than thermal) root definition in order to exclude any effects of secular cooling. There are two thickening regimes in model L and L2: tectonic compressive thickening and gravitational thickening. B) Volumetric percentage of remaining root material over time to illustrate the amount of recycling into the underlying upper mantle of chemical root material.*

7.3.2 Parameters sensibility study

7.3.2.1 Shortening length

The effects of different shortening lengths are investigated in this section. The same shortening velocity is imposed at the boundary but with different shortening durations of 0 Myr (L1), 30 Myrs (L2), 50 Myrs (L) and 80Myrs (L3), which result in shortening length of 0 km, 600 km, 1000 km and 1600 km (Table 7.2), respectively. Fig. 7.4 illustrates the evolutions of the chemical thickness and the amount of remaining root in these models. Without any imposed shortening (model L1), the self-driven thickening of the depleted mantle material doesn't occur (Fig. 7.4A). Although most of the depleted material survives for 1Gyrs in this case (Fig. 7.4B), a thick cratonic root is not formed. In model L2 (1cm/yr × 30 Myr) , the slow self-driven thickenings as described in section 7.3.1 follows the imposed shortenings and helps to form a cratonic root with an average depth of 180 km (Fig. 7.4, Fig. 7.5A-D). However, 180 km is thinner than the thicknesses of most cratons [*Rudnick and Nyblade*, 1999; *Gung et al.*, 2003]. From the thickness evolutions in Fig. 7.4A, the self-driven thickening after the initial imposed thickening in the reference model (~41 km) is larger than in model L2 (~20 km). This indicates that the substantial initial thickening and shortening of the depleted material is essential for the development of further, late stage gravitational thickening of the cratonic root.

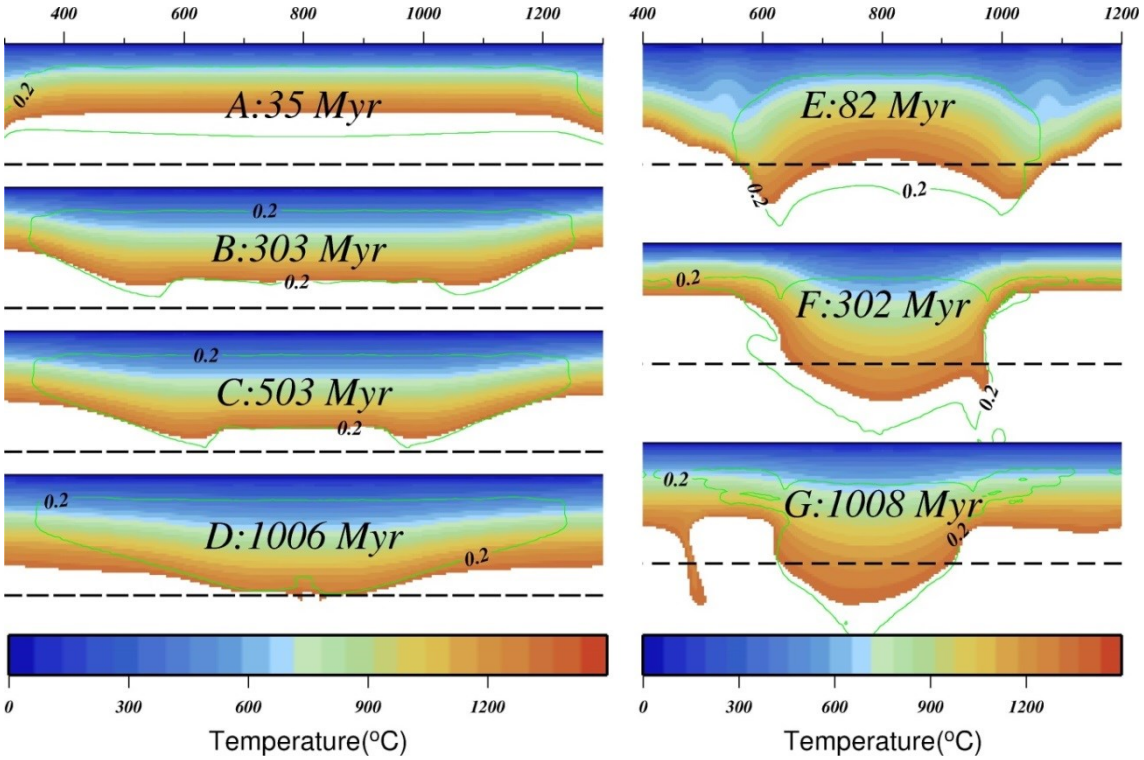

Fig. 7.5: *A)-D) The thickening of the chemical root in model L2 that has less shortening (600 km) than in the reference model L (1000 km). E)-G) The shortening and recycling of chemical root material in model L3, which has undergone much more shortening (1600 km).*

However, too much imposed shortening leads to different dynamics, as demonstrated by model L3 (Fig. 7.4 and 7.5E-G). In that case, the depleted material is pushed down to a depth of more than 240 km within 80 Myrs, but late stage, further thickening is not occurring in this model, and instead, significant thinning of the root occurs (Fig. 7.4). Unlike the previous models, the chemical root undergoes significant instability and recycling before it has the chance to cool down sufficiently to form a stabilizing thermal boundary as in the reference models (Fig. 7.5E-G). Instead, more and more root material is recycled over time (Fig. 7.4B) and the root becomes progressively smaller (Fig. 7.5) over time, which is not the characteristic of a stable craton. Therefore, a certain minimum amount of shortening is required to create thick enough cratons, but too much initial shortening may prohibit the formation of a stable cratonic root.

Table 7.2 Comparison of parameters in all discussed models.

model	shortening length (km)	shortening velocity(cm/yr)	basal cooling rate (^{0}C/Gyr)
L1	0	0	100
L	1000	1	100
L2	600	1	100
L3	1600	1	100
S1	1000	2	100
S2	1000	0.5	100
S3	1000	0.25	100
S4	1000	0.125	100
SC1	1000	1	50
SC2	1000	1	0

7.3.2.2 Shortening speed

Next, we apply the same shortening length as in the reference model but with different shortening speed, which results in 25, 100, 200, 400 Myrs shortening period in models S1, S2, S3, S4 (Table 7.2), respectively. As Fig. 7.6A shows, although the imposed shortening speed varies over more than an order of magnitude between the models, all of these models form a cratonic root of ~220 km or even thicker. The root recycling during the craton thickening shows a positive correlation with the imposed shortening speed as illustrated in Fig. 7.6B: faster shortening recycles more root material. The sudden drop in the amount of remaining root at the end of the imposed shortening period in the S1, L, and S2 models in Fig. 7.6B are caused by the delamination of root material in these models, which doesn't occur in the slow shortening models (S3, S4). This can be explained by the stress field imposed by the shortening, as faster shortening induces stronger stress weakening effects on the rheology of the root material which leads to the delamination or dripping of the root material.

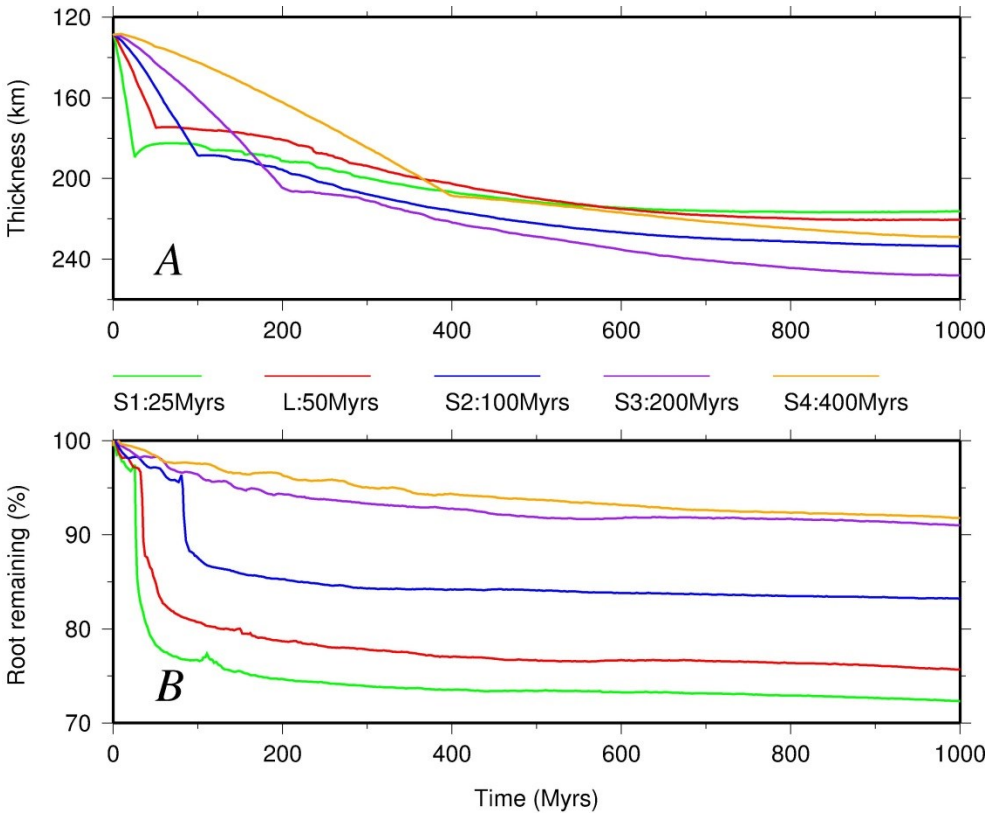

Fig. 7.6: *The thickening and recycling of the cratonic root in models with different shortening speeds (Models S1, L, S2, S3, S4) over a time period of 1000 Myrs. The same shortening lengths are applied in these models (1000 km), which results in different shortening periods (25Myrs, 50 Myrs, 100 Myrs, 200 Myrs, 400 Myrs, respectively). Faster shortening leads to more and faster root recycling.*

The root shapes at around 600 Myrs in model S1-S4 are plotted in Fig. 7.7 in order to clarify the effect of the shortening speed. In the fastest case, this shortening occurs within 25 Myrs (Model S1), significant yielding of the lithosphere occurs, and induces an undulating boundary on the top of the root. This preserved undulating structure is similar to those described for the localized thickening of cratonic lithosphere by *Cooper and Miller* [2014]. In the slowest endmember (model S4), the shortening of the lower part of the root is not very developed (Fig. 7.7D) compared to other models because the shortening is so slow that the mobility of lower root is reduced significantly by the secular cooling for 400 Myrs. The wider root shape of model S4 (Fig. 7.7D) also explains why it doesn't have a thicker root than other models, even though it has more root material survived (Fig. 7.6B). Therefore, slow shortening is generally better than fast shortening for the amount of root survival, but a well-developed cratonic root requires the thickening to be fast enough to avoid the significant effect that simultaneous cooling may have on the thickening process.

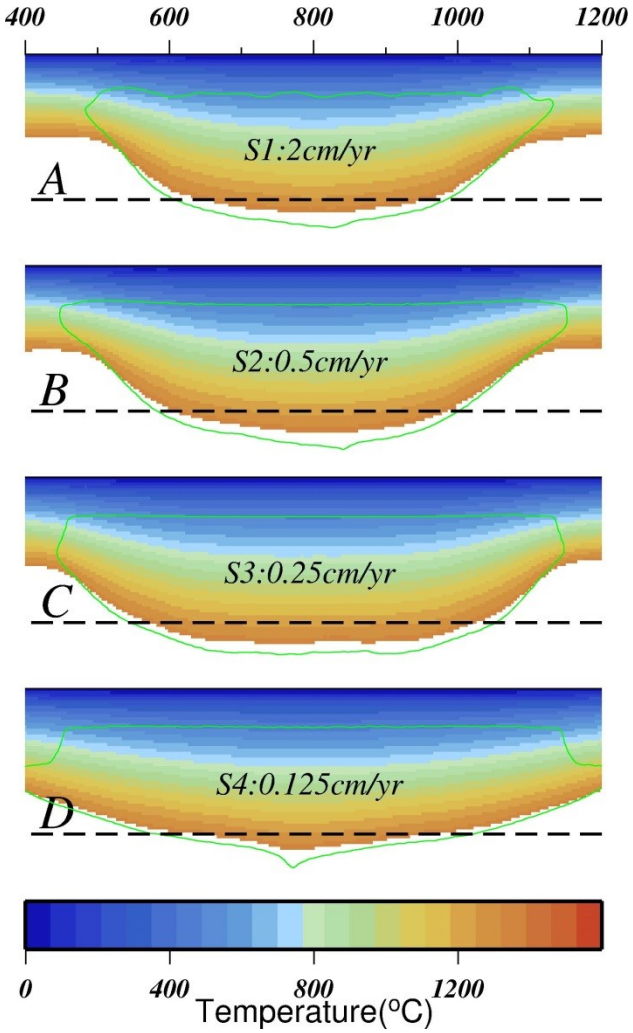

Fig. 7.7: *Cratonic root shapes at 600 Myrs model time for models with different shortening speeds. Strong yielding in model S1 (A) induces an undulating boundary at the top of the chemical root. The chemical root shape in S4 (D) is not well-developed since the mantle cools down significantly during the imposed shortening.*

7.3.2.3 Secular cooling

In our reference model *L*, the basal temperature reduces by $\lambda=100^0$C/Gyr in order to mimic effects of the secular cooling of the mantle. In this section, we compare models with different cooling rates (Table 7.2) and demonstrate how this affects the craton thickening and stabilization process. Fig. 7.8 shows the thickness and remaining root evolution of three models with cooling rates of 100^0C/Gyr (L), 50^0C/Gyr (C1), and 0^0C/Gyr (i.e. no cooling, C2). While the reference model and model C1 remain stable even after t = 1 Gyr, model C2 without basal cooling (^{0}C/Gyr) has a quiet period until t=1Gyr, but then start to show significant perturbations as observed in both the thickness (Fig. 7.8A) and remaining root percentage (Fig. 7.8B). The cratonic root is clearly thinned and recycled during this period, which requires substantial dynamics of the cratonic root. The root-mean-square velocities of the cratonic root ("vrms") are calculated based on the composition field and plotted in Fig. 7.8C. It shows that the cratonic root in

model C2 becomes dynamically active after 1 Gyrs by approaching the "vrms" of the whole domain area (thick, red), while the root in the reference model L becomes more and more inactive over time and the root in model C1 suggests a relatively constant degree of activity through time.

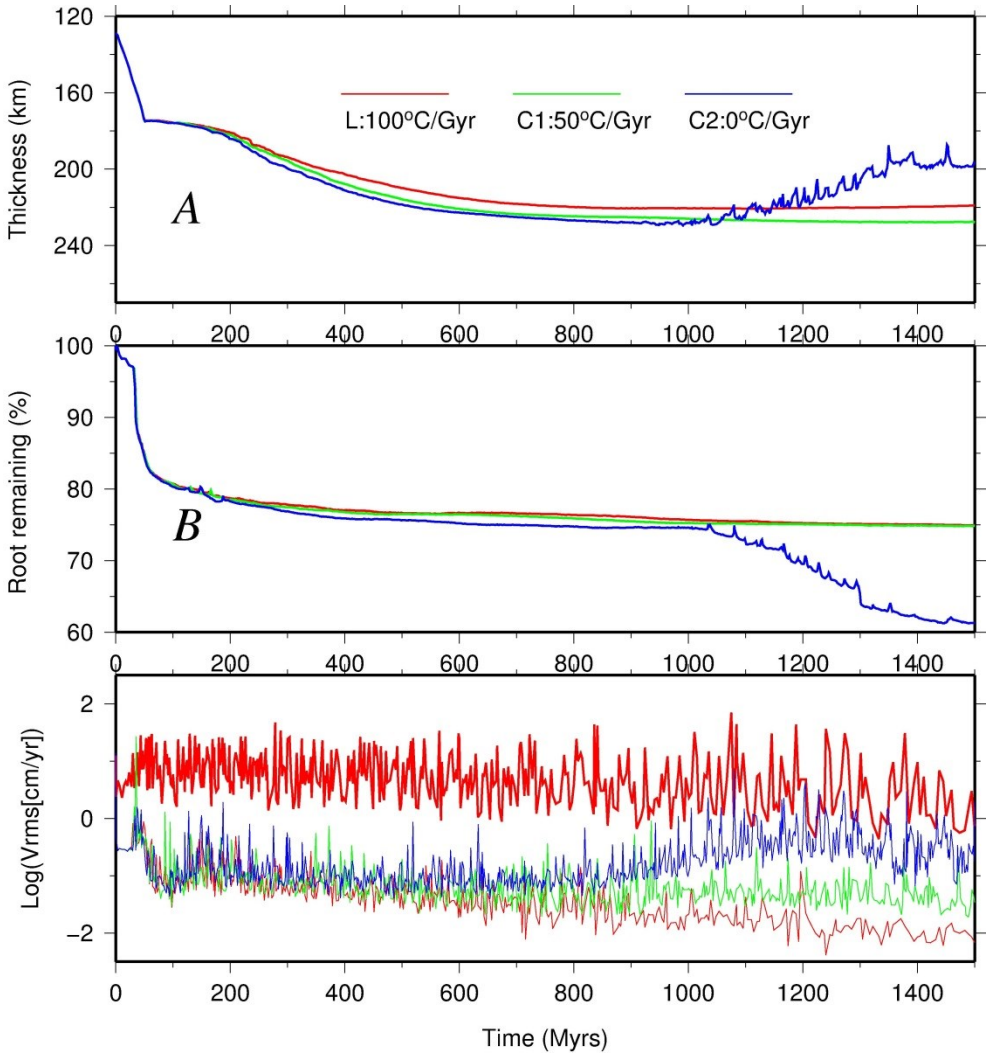

Fig. 7.8 *Thickness (A), remaining volumetric percentage (B) and root-mean-square velocity (C) of the cratonic root material in models with different secular basal cooling rates over a time period of 1500 Myrs. As a comparison, the thick red line in C is root-mean-square velocity of the whole model domain (model L). Whereas models L (100^{0}C/Gyr) and C1 (50^{0}C/Gyr) remain stable indefinitely, the cratonic root in model C2 without basal cooling starts to show significant thinning and recycling of the root material after ~1 Gyrs.*

Fig. 7.9 shows the root dynamics of model C2 over a short period of 45 Myrs. The core of the thermal root doesn't really change shape within this small period as showed by the evolution of temperature field in Fig.7.9. However, a dramatic cycle of the movement of the root material is illustrated in the same period (Fig. 7.9): the root material to the left side of the craton sinks down to the bottom (Fig.7.9A to 9B) in 19 Myrs, then it move back upward (Fig. 7.9C) to its original position (Fig. 7.9D) after 26 Myrs. This cycle occurs over and over again with more and more root material eroding away (Fig.7.8B). Unlike a Rayleigh Taylor instability of the thickening lithosphere [*Houseman and Molnar*, 1997] in which the root material typically never returns, this instability of the compositionally buoyant root demonstrates an oscillatory behaviour. Similar oscillatory instabilities was also found in both laboratory studies [e.g. *Jaupart et al.*, 2007] and independent numerical modelling studies [e.g. *Wang et al.*, 2015].

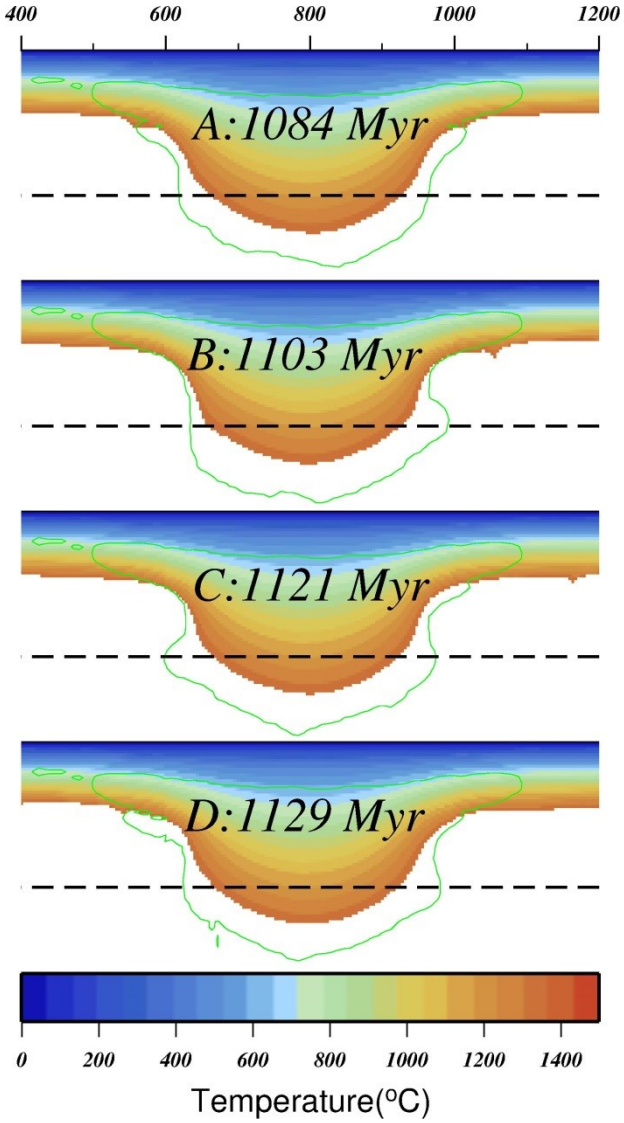

Fig. 7.9: *Illustration of the oscillatory instability of the cratonic root after 1 Gyrs in model C2 without secular cooling of the mantle: the chemical cratonic root undergoes periodic dripping down and moving up over several 10s of Myrs.*

7.4 Discussion

Our numerical models demonstrate that a craton with a >200 km deep root can be formed through the compressive shortening of a layer (30-120 km) of depleted mantle material, followed by a self-driven thickening process. Significant downward movements of cratonic root material occurs in our models, which agrees well with the observation that the equilibration P-T position of cratonic root material is deeper and cooler than that of its protolith as illustrated in Fig. 7.1. Using the presented modelling results from this chapter, we discuss below the cratonization of depleted mantle material as a combination of two processes: craton thickening and craton stabilization.

7.4.1 Thickening of cratons

Our modelling results show that root recycling during the thickening process is positively correlated with the shortening speed: fast shortening mostly induces faster and more recycling of root material than slow shortening (Fig. 7.4, 7.6). However, such compressive shortening and thickening is not likely to last 100s of Myrs (Model S3, S4) in reality. Thus, even though the slow, long-term shortening (model S3,S4) preserves more root material, faster shortening models (L, S1) with substantial recycling (~20%) of the root probably provide more realistic scenarios of how a craton builds its thick root. This also suggests that more initially depleted material is required for craton formation than is presently observed in craton roots.

The initial, externally driven compressive thickening plays an essential role in the initialization of the thickening process. Without enough initial compressive thickening of the depleted mantle material, the self-driven thickening of the root will not take place (model L1) or cannot form a realistic root thickness (model L2). The compressive thickening may be a tectonically more complex process, and might involve phenomena such as subduction accretion, lithosphere underplating, or continental collision, all of which require tectonic, localised deformation that cannot be achieved by our relatively simple model setup. A present-day example of lithosphere thickening is the formation of the Tibetan plateau, which has undergone a several 100-km shortening of the lithosphere over 10s of Myrs [*DeCelles*, 2002; *Tian et al.*, 2013]. McKenzie et al. [2008] suggested this to be a modern example of a craton-forming process. Whether the Tibetan plateau will eventually form a stable craton or not is beyond the scope of this study, but it provides a real example of the scale of compressive thickening as envisioned in our craton thickening models. *Sleep* [2005] suggested that cratonic lithosphere formed by processes analogous to modern tectonics. Our models demonstrate how a process analogous to modern orogenic shortening could lead to the formation of the thick cratonic lithosphere.

On the basis of laboratory studies of the effects of melt depletion on the physical properties, *Schutt and Lesher* [2006] concluded that any subcratonic mantle formed above ~110 km is negatively buoyant relative to the adiabatic mantle. This negative buoyancy provides an inherent

driving force for the vertical transportation and thickening of the cratonic root besides the imposed compressive thickening. It would promote the thickening of the cratonic root in the case of less compressive shortening, but it is unlikely to form a thick craton by itself without the externally imposed compressive thickening.

The gravitational, second-stage thickening regime of our models is driven by the cooling and growth of the negative thermal buoyancy of the root material as a result of the compressive thickening and subsequent diffusive cooling. The cratonic root grows vertically by ~41 km in ~600 Myrs in our reference model. *Mareschal and Jaupart* [2006] suggested that the thermal field of cratonic lithosphere remains in disequilibrium for ~1-2 Gyrs after the root emplacement, which is not out of line with the ~600 Myrs of thickening in our models as result of the thermal adjustment.

7.4.2 Stabilization of cratons

Even though the high viscosity and chemical buoyancy of the depleted root play an important role in the long-term stability of the cratons, our models show that a large amount of depleted mantle material doesn't guarantee the stabilization of cratons. In the reference model, a self-thickening process is driven by the growth of the negative thermal buoyancy due to cooling of the root after the 50 Myrs compressive shortening. This process, leads to the convergence of the thermal root and chemical root and thus stabilizes the cratonic root (Fig. 7.3C-D). In model L3, where significantly more shortening is applied, the same amount of depleted mantle material cannot stabilize the cratonic root, not even after 1 Gyrs. Unlike in the reference model, the thick root in model L3 experiences continuous, significant recycling of the root as the chemical root cannot form a strong thermal layer even after 1 Gyr. Although part of the chemical root survives for more than a billion years in model L3, such an unstable root is not a good example for the cratons that survived many tectonic events. Therefore, the quick compressive shortening (10s of Myrs) of the depleted mantle material to a depth as observed for the present cratons may not form a stable craton. Instead, a slow self-driven thickening and adjustment process is required to stabilize the thick cratonic root.

Apart from an instability caused by too much thickening, our model results also illustrate another type of instability that can occur if no secular cooling is taken into account. In that case, a specific mode in which parts of the cratonic root drip down and move up again periodically (over 10s of Myrs). These models demonstrate such oscillatory characteristic after an initial, long quiet period of ~1 Gyr (model C2 in Fig. 7.9). Previous 2D thermochemical convection modelling with varying buoyancy number (ratio between chemical buoyancy and the negative thermal buoyancy) and lithospheric Rayleigh numbers have identified three dynamic regimes of chemically buoyant lithosphere [*Jaupart et al.*, 2007; *Wang et al.*, 2015]: a stable regime, a layered convection regime and an unstable regime. The unstable regime includes an oscillatory

sub-regime in which the destabilized root moves up and down in the mantle [*Wang et al.*, 2015] similar to our model results in Fig. 7.9. Due to the different model setups, direct comparison of buoyancy numbers with these studies is difficult, but the oscillatory instability in models without secular cooling suggests that the initial chemical and thermal buoyancy in these models actually falls into an oscillatory regime. The secular cooling rates of 100 or 50 ^{0}C/Gyr (model L, C1), however, increases the buoyancy number (ratio between chemical buoyancy and thermal buoyancy) into a stable regime by reducing the total thermal buoyancy and leads to the stabilization of the cratonic root. In addition, the increase of mantle viscosity as a result of mantle cooling also contributes to the stabilization of the thick root by reducing the Rayleigh numbers as suggested by *Michaut et al* [2009]. Increasing the buoyancy number by an even more chemically buoyant root would dampen the oscillatory instability beyond 1 Gyr, but a root with too much buoyancy may not allow for enough thickening to form a thick craton.

As a result of the long-term thermal evolution, the cratonic root that is approximately isopycnic under present conditions would be either more or less buoyant in the past [*Eaton and Claire Perry*, 2013]. This indicates that the long-term stability of cratons require other mechanism than the isopycnic status, thus the contributions from high viscosity of the root and secular cooling to the craton stabilization must be essential. *Schutt and Lesher* [2006] proposed another possible stabilization mechanism based on the laboratory study of the physical properties of the melt depleted mantle rock. They argue that the highly depleted mantle material that formed above 110 km is negatively buoyant relative to the adiabatic mantle but it may be neutrally buoyant once it is moved to a larger depth because of the depth-dependent effects of melt depletion on the density of the rocks and the thermal expansivity. How such a mechanism promotes the stabilization of cratonic root is yet unclear, but it is worthy of a future investigation.

7.5 Conclusion

Numerical experiments have been performed to study the thickening and stabilization of cratonic root in a thermally evolving mantle. The following conclusions are drawn based on the analyses and discussions of our numerical models:

1. Geodynamical modelling supports the vertical movement of depleted material during the cratonization process as previously suggested on petrological grounds [Lee and Chin, 2014] and using geophysical arguments [*Schutt and Lesher,* 2006].

2. Substantial initial tectonic shortening and thickening of previously depleted material is essential to initiate the cratonization process, and could perhaps have been caused by tectonics similar to today's orogenic processes associated with phenomena such as subduction accretion, lithosphere underplating, or continental collision.

3. Gravitational self-thickening occurs after the initial tectonic compressive shortening and causes further thickening, while intrinsic compositional buoyancy of the cratonic root prevents a Rayleigh-Taylor type collapse, and stabilizes the thick cratonic root.

4. Secular cooling has a stabilizing effect on the cratonic root by reducing the thermal buoyancy contrast between lithosphere and asthenosphere and increasing mantle viscosity, and may be an essential ingredient for the long-term survival of cratons.

Chapter 8

Summary and outlook

8.1 Summary and conclusions

This thesis has aimed to study the different scenarios of the evolution of the cratonic lithosphere by using geodynamical modelling. The most salient but relatively poorly understood observation of cratons is the long term survival of both the crust and mantle lithosphere, which led to the study of the stability and longevity of cratonic lithosphere as in Chapter 5. It was found that the composition-dependent rheology of the mantle rheology is essential for the longevity and stability of cratonic lithosphere. A related question is how such a stable craton responds to major tectonic events such as nearby mantle plumes, subduction zones, or continental collisions. Chapter 6 tested the hypothesis that a mantle plume may cause significant thinning of the subcontinental lithosphere by modelling such plume-craton interaction. Underlying all of these studies is the basic scientific question how such stable, thick cratonic lithosphere was formed in the first place if it is so impregnable because of its chemical root. The modelling results in Chapter 7 demonstrated that a thick cratonic root could have been formed through initial compressive tectonic shortening followed by further gravitational thickening of viscous, buoyant, mantle material. Unlike most previous, related numerical studies, non-Newtonian rheologies with composition dependence was used in these studies, and the rheological parameters are thus directly comparable with laboratory experiment of mantle rheology [e.g. *Hirth and Kohlstedt*, 1996; *Karato*, 2006; *Fei et al.*, 2013]. Through these numerical studies, two hypotheses about the craton stability and evolution were revisited and the process of cratonization was investigated.

The first hypothesis is the "isopycnic" hypothesis of the cratonic lithosphere [*Jordan*, 1978, 1988]. It had been found that the strict "isopycnic" status of cratonic root is not necessary for craton stability and longevity, and a modest negative buoyancy of the root is allowed if the cratonic root is compositionally more viscous than the normal mantle. Furthermore, such a compositionally more viscous cratonic root was found to be essential to maintain a thickness difference between cratonic and non-cratonic lithosphere for billions of years. With non-Newtonian rheology, a strengthening factor of 10 (in the constant strainrate definition, corresponding to a factor of 10^n in the constant-stress definition) can preserve a cratonic root from the erosion by small scale convection over 2 Gyrs, no matter whether the cratonic root is compositionally

buoyant or not. A smaller strengthening factor of 3 can also protect a cratonic root from eroding away for billions of years but a chemically buoyant root is also required in this scenario.

The second hypothesis is that the mantle plumes might cause the significant removal of subcontinental lithosphere. The results presented in this thesis show that the erosion caused by a plume impact on a strong continent is rather limited. Plumes impacting on less strong (and/or less buoyant) subcontinental roots produce significantly more erosion at root edges in a relatively short (~10s of Myrs) amount of time, but even without such a plume impact, a similar amount of erosion could eventually occur due to continued plate-mantle interaction, albeit over much longer time scales (several 100 Myrs - 1 Gyr). Instead, this work illustrates that generating a distinctly weakened root (less strong and less buoyant) is essential for significant thinning of subcontinental lithosphere by a mantle plume impingement over timescales of a few 10s of Myrs. In other words, highly viscous and buoyant cratonic roots can provide the long term stability of most cratons as observed, but a special weakening mechanism of such roots is required in order to reactivate the cratonic lithosphere by a tectonic or mantle dynamic event such as a mantle plume impingement. Fluid/melt-rock interaction during mantle metasomatism is probably the most likely mechanism to modify and weaken the depleted subcontinental lithosphere. Depending on the extent of the metasomatic weakening, as well as the tectonic environment, different types of reactivation of the cratonic lithosphere may occur, such as thinning of subcontinental lithosphere (e.g. underneath southern Africa), complete destruction of the cratonic root (e.g at the North China Craton) and continental rifting (e.g. of the North Atlantic Craton).

As a potentially important process of cratonization, the thickening of cratonic lithosphere in a thermally evolving mantle is studied with geodynamical models. The numerical results show that substantial initial tectonic shortening and thickening of previously depleted material is essential to initiate the cratonization process. This initial shortening could perhaps have been caused by tectonics similar to today's orogenic processes associated with phenomena such as subduction accretion, lithosphere underplating, or continental collision. Gravitational self-thickening takes place after the initial tectonic compressive shortening and causes further thickening, while compositional buoyancy resists the Rayleigh-Taylor instability collapse and stabilizes the thick cratonic root. Secular cooling since the Archean has a stabilizing effect on the cratonic root by reducing the thermal buoyancy contrast between lithosphere and asthenosphere and increasing mantle viscosity. More importantly, the presented numerical results are consistent with the vertical movement of cratonic peridotite as suggested on petrological grounds [*Lee and Chin*, 2014] and using geophysical arguments [*Schutt and Lesher*, 2006].

8.2 Research outlook

8.2.1 3D plume craton interaction with melting effects

In this thesis, I mainly focused on the 2D geodynamical modelling and ignored any 3D features of the cratonic lithosphere for simplicity. However, it is worthwhile to further investigate similar geodynamic problems in 3D models as the cratons are not typically elongated in both two horizontal directions. Plumes in a 3-dimensional (3D) dynamic situation might exhibit different behaviour compared with 2-dimensional (2D) models [*Ribe and Christensen*, 1994; *van Keken and Gable*, 1995]. For example, the plume flow around the cratonic root in 3D geometry cannot be modeled in 2D simulation (Fig 8.1). Protracted regional heating events between 150Ma and 65 Ma have been recorded around the Kaapvaal craton in southern Africa [*Bell et al.*, 2003]. The 3D geodynamic modelling of plume craton interaction may help to find out how they correlated spatially to the various mantle plume events in Africa.

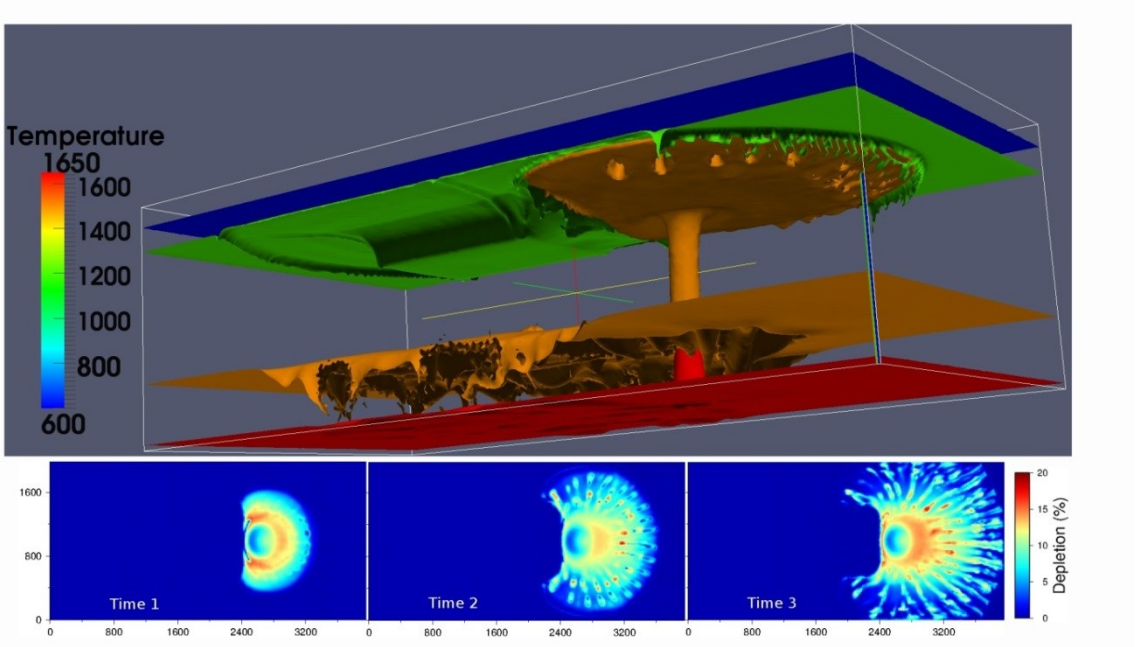

Fig 8.1: *3D plume-craton interaction with plume induced melting and depletion. The three bottom images show the mantle depletion at a depth of 120 km caused by the plume induced melting.*

Also, melting and depletion effects of a plume impingement event are not explicitly modelled in the presented studies (even though they are implicitly incorporated). As mentioned in Chapter 6, such mantle plume event might induce widespread melting and thus may cause metasomatic weakening of the cratonic lithosphere. Since the cratonic lithosphere is significantly thicker than normal lithosphere, any decompression melting underneath cratons is rather limited and it is the edge of the cratonic lithosphere that is most likely affected by plume melting. Fig.8.1 demonstrates how a mantle plume event impacts the cratonic lithosphere by using 3D geodynamical modelling in which melting is explicitly incorporated. How and to what extent

these melts migrate and interact with the cratonic root is of significant importance to the erosion of cratonic lithosphere. Recent laboratory experiments show that the interaction between melt segregation and stress would weaken mantle material more than a homogeneous melt distribution [*Holtzman et al.*, 2012]. This effect would enhance the stress and strain rate localization during any thermal-tectonic events and make significant removal of cratonic lithosphere possible, which need to be included in future geodynamic modelling. Another interesting observation from Fig. 8.1 is the depletion patterns of the mantle at 120 km. These patterns share similar structure with the giant radiating dyke swarms on Earth and Venus [*Ernst et al.*, 1995], such as the Mackenzie swarm.

8.2.2. Growth of Cratonic lithosphere.

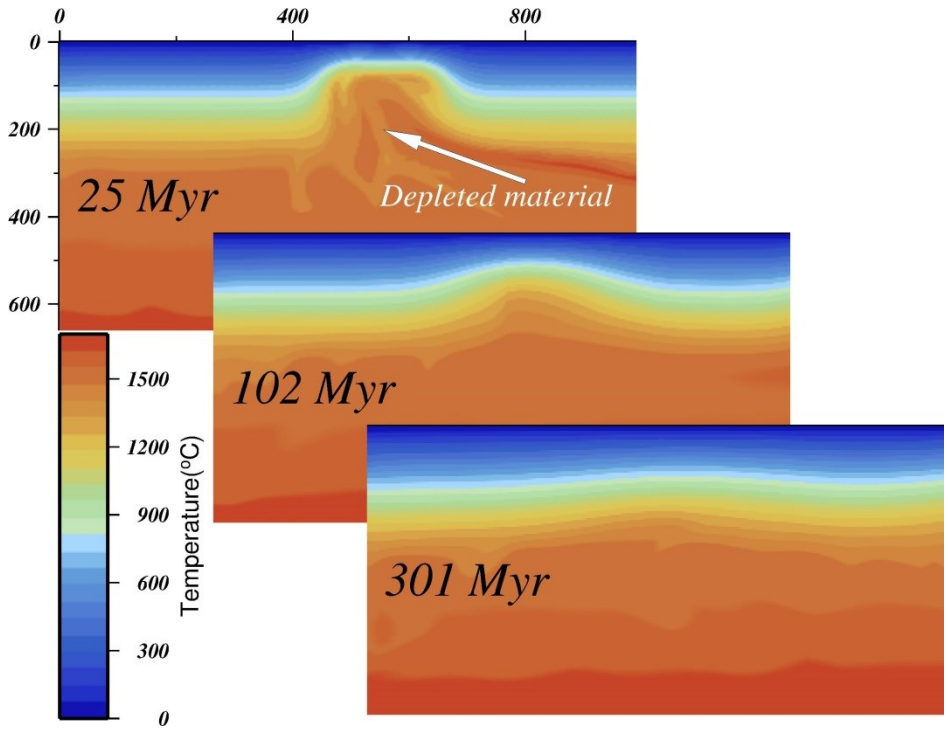

Fig. 8.2: *The growth of the cratonic lithosphere by adding depleted mantle material from nearby mantle plumes. The thin lithosphere represents the rifted lithosphere after the Midcontinent rift underneath Victor Mine at Superior craton. The melting and depletion are explicitly incorporated in this model.*

Another possible scenario of craton evolution is the growth of cratonic lithosphere by adding depleted mantle material. Kimberlite evidence shows that diamond-stability field conditions formed after the Midcontinent rift at 1.1 Ga underneath the Victor Mine (a world-class primary diamond deposit) in the northern Superior superterrane [*Smit et al.*, 2014]. The rift failed to break up the continent, so the two parts of thick lithosphere are separated by a thinned, but not completely rifted lithosphere. The preliminary modelling shown in Fig 8.2 illustrates that the thin, intermediate lithosphere grows to a similar thickness as the surrounding thick lithospheres

in ~300 Myrs: after a major melting event, the depleted (and therefore compositionally strong, but still thermally weak) mantle material first fills up the gap between thick lithosphere at ~25Myr, and the following mantle cooling thickens the thinning lithosphere and combine two separate thick root together in ~300 Myr. A similar experiment without depletion strengthening effect does not show any significant growth of lithosphere. This suggests again that the rheological effect of mantle depletion plays an important role in the growth of thick cratonic lithosphere, even for parts of the cratonic lithosphere that are growing laterally adjacent to an already existing craton. These results illustrate how mantle plume melting might lead to the growth of the cratonic lithosphere after the failed continent rift. In Chapter 6, the plume and plume related metasomatism was shown to be capable of causing significant thinning of the subcontinental lithosphere. Thus, it is very interesting to investigate in future studies that under which conditions a mantle plume might result in the removal of the lithosphere, and in which cases it can help cratonic lithosphere grow.

8.2.3. Crust dynamics during the craton formation.

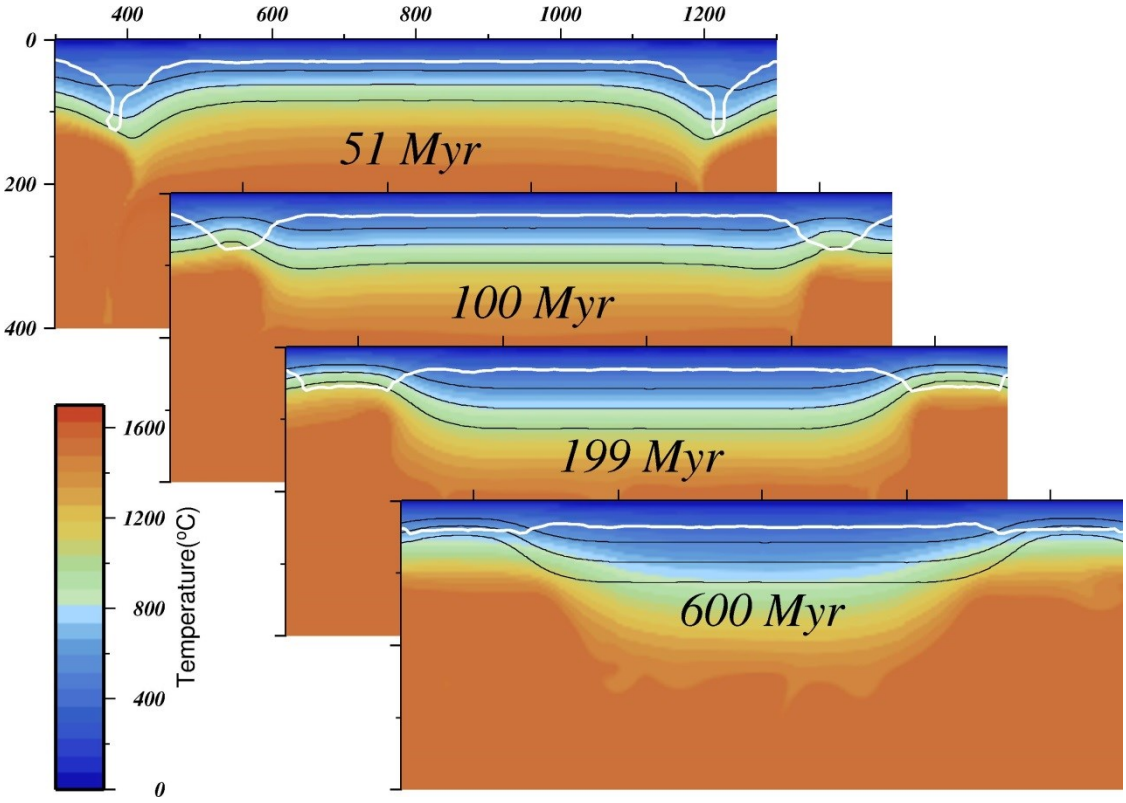

Fig. 8.2: *The crust dynamics during the thickening of the cratonic lithosphere. The white lines indicate the Moho discontinuity.*

Any hypothesis for craton formation must address the question how the continental crust evolved to its current status [*Carlson et al.*, 2005; *Herzberg and Rudnick*, 2012; *Pearson and Wittig*, 2014]. The continental crust paradox mentioned in Chapter 7 remains an important problem in the Earth science community. Sofar, the added complexity of crust dynamics during the thickening of the cratonic lithosphere in Chapter 7 has been ignored in order to focus on the formation of the thick mantle root. But preliminary numerical models show that the high heat production of the crust has a pronounced dynamical influence over short timescales, especially during and shortly after the compressive tectonic shortening. The crust also experiences significant thickening during the compressive shortening, but this mainly focuses near the edge of the craton because the viscous and buoyant interior of the mantle root make crustal thickening more difficult in the craton interior (Fig. 8.3). The high radiogenic heating in the Archean crust heats the edge of the cratonic root significantly and forms a sharp transition between cratonic mantle and normal mantle after ~50-200 Myrs (Fig. 8.3). This hot, weak crust at the cratonic edge may help to form the weak mobile belts around cratons that have been proposed to shield them from later tectonic stresses [*Lenardic and Moresi*, 1999; *Lenardic et al.*, 2000]. The transition from basalt to eclogite (at around 1.2 Gpa and 800^0C under equilibrium conditions) causes a significant increase in density of the lower crust. This effect was not included in the presented models, but, if added, could potentially cause substantial amounts of eclogite to be formed at the edge of the craton and to be delaminated into the mantle. The delamination of eclogite might contribute significantly to the current composition of the Archean crust by removing mafic materials [*Arndt and Goldstein*, 1989; *Jull and Kelemen*, 2001], and as such be a possible solution to the continental crust paradox. A combined geodynamical-petrological modelling approach for the formation of cratonic root and continental crust is an important and challenging problem.

Appendix A: Conservative Velocity Interpolation[4]

Derivation of 3D Conservative Velocity Interpolation (CVI) for Incompressible Flow Problem

We focus on the incompressible flow problem, in which the conservative velocity interpolation is actually a divergence-free interpolation. Here we first describe the 2D divergence-free velocity interpolation by *Meyer and Jenny* [2004] and further derive 3D divergence-free interpolation formulations.

In a 4-node 2D rectangular cell system, bilinear interpolation provides a simple and quick interpolation scheme and is widely used. If we transform the rectangular cells into unit squares (Fig 1), the interpolation we used can be written as:

$$U_i{}^L(x_1,x_2) = \{(1-x_1)(1-x_2), x_1(1-x_2), (1-x_1)x_2,\ \ x_1x_2\}$$

$$\cdot \{U_i^a, U_i^b, U_i^c, U_i^d\} \tag{A1}$$

where the two velocity components are interpolated independently as two separate scalars without considering the divergence of the vector field need to be 0:

$$\frac{\partial U_1}{\partial x_1}+\frac{\partial U_2}{\partial x_2}=0 \tag{A2}$$

The 2D divergence-free interpolation is achieved by adding correction items as follows [*Meyer and Jenny*, 2004]:

$$U_i = U_i{}^L + \Delta U_i, \tag{A3}$$

$$\Delta U_1 = \frac{\Delta x_1}{2\Delta x_2} x_1(1-x_1)\left(U_2^a - U_2^b - U_2^c + U_2^d\right), \tag{A4}$$

$$\Delta U_2 = \frac{\Delta x_2}{2\Delta x_1} x_2(1-x_2)(U_1^a - U_1^b - U_1^c + U_1^d). \tag{A5}$$

In Eqs (A4) and (A5), the correction item for each velocity component is calculated based on the other velocity component of the nodes. We extend this approach into 3D situation by adding a quadratic item of x_i to each velocity component:

[4] This Appendix has been submitted as Supplementary material to a manuscript that has been submitted for publication, and that appears as Chapter 4 in this thesis.

$$\begin{aligned} U_i^L(x_1,x_2,x_3) = {} & (1-x_1)(1-x_2)\left[(1-x_3)U_i^a + x_3U_i^e\right] + \\ & x_1(1-x_2)\left[(1-x_3)U_i^b + x_3U_i^f\right] + \\ & (1-x_1)\,x_2\left[(1-x_3)U_i^c + x_3U_i^g\right] + \\ & x_1\,x_2\left[(1-x_3)U_i^d + x_3U_i^h\right] \end{aligned}, \tag{A6}$$

$$\Delta U_1 = x_1(1-x_1)(C_{10} + x_2C_{12}), \tag{A7}$$

$$\Delta U_2 = x_2(1-x_2)(C_{20} + x_3C_{23}), \tag{A8}$$

$$\Delta U_3 = x_3(1-x_3)(C_{30} + x_1C_{31}). \tag{A9}$$

The coefficients C_{10}, C_{12}, C_{20}, C_{23}, C_{30}, C_{31} in Eqs (A7-A9) are to be determined. They should satisfy the following divergence free condition for 3D incompressible flow field:

$$\frac{\partial U_1}{\partial x_1} + \frac{\partial U_2}{\partial x_2} + \frac{\partial U_3}{\partial x_3} = 0. \tag{A10}$$

Thus, we take the first derivatives of U_i with respect to x_i based on Eqs (A3, A6, A7, A8, and A9):

$$\begin{aligned} \Delta x_1\frac{\partial U_1}{\partial x_1} = {} & (1-x_2)*(1-x_3)*\left[U_1^b - U_1^a\right] + x_2*(1-x_3)*\left[U_1^d - U_1^c\right] \\ & +(1-x_2)*x_3*\left(U_1^f - U_1^e\right) + x_2*x_3*\left(U_1^h - U_1^g\right) \\ & +(1-2x_1)*(C_{10} + C_{12}*x_2) \end{aligned} \tag{A11}$$

$$\begin{aligned} \Delta x_2\frac{\partial U_2}{\partial x_2} = {} & (1-x_1)*(1-x_3)*\left[U_2^c - U_2^a\right] + x_1*(1-x_3)*\left[U_2^d - U_2^b\right] \\ & +(1-x_1)*x_3*\left(U_2^g - U_2^e\right) + x_1*x_3*\left(U_2^h - U_2^f\right) \\ & +(1-2x_2)*(C_{20} + C_{23}*x_3) \end{aligned} \tag{A12}$$

$$\begin{aligned} \Delta x_3\frac{\partial U_3}{\partial x_3} = {} & (1-x_1)*(1-x_2)*\left[U_3^e - U_3^a\right] + x_1*(1-x_2)*\left[U_3^f - U_3^b\right] \\ & +(1-x_1)*x_2*\left(U_3^g - U_3^c\right) + x_1*x_2*\left(U_3^h - U_3^d\right) \\ & +(1-2x_3)*(C_{30} + C_{31}*x_1) \end{aligned} \tag{A13}$$

Substitute Eqs (A11-A13) in to Eq (A10) and we have an identical equation with the six unknowns (C_{10}, C_{12}, C_{20}, C_{23}, C_{30}, C_{31}). As the result, the following items should have their coefficients to be zeros: 1, x_1, x_2, x_3, x_1x_2, x_2x_3, x_3x_1, which leads to 7 equations:

$$1: \frac{1}{\Delta x_1}[U_1^b - U_1^a + C_{10}] + \frac{1}{\Delta x_2}[U_2^c - U_2^a + C_{20}] + \frac{1}{\Delta x_3}[U_3^e - U_3^a + C_{30}] = 0$$

$$x_1: \frac{1}{\Delta x_1}[-2C_{10}] + \frac{1}{\Delta x_2}[U_2^a - U_2^c + U_2^d - U_2^b] + \frac{1}{\Delta x_3}[U_3^a - U_3^e + U_3^f - U_3^b + C_{31}] = 0$$

$$x_2: \frac{1}{\Delta x_1}[U_1^a - U_1^b + U_1^d - U_1^c + C_{12}] + \frac{1}{\Delta x_2}[-2C_{20}] + \frac{1}{\Delta x_3}[U_3^a - U_3^e + U_3^g - U_3^c] = 0$$

$$x_3: \frac{1}{\Delta x_1}[U_1^a - U_1^b + U_1^f - U_1^e] + \frac{1}{\Delta x_2}[U_2^a - U_2^c + U_2^g - U_2^e + C_{23}] + \frac{1}{\Delta x_3}[-2C_{30}] = 0$$

$$x_1x_2: \frac{1}{\Delta x_1}[-2C_{12}] + \frac{1}{\Delta x_3}[U_3^e - U_3^a + U_3^b - U_3^f + U_3^c - U_3^g + U_3^h - U_3^d] = 0$$

$$x_2x_3: \frac{1}{\Delta x_1}[U_1^b - U_1^a + U_1^c - U_1^d + U_1^e - U_1^f + U_1^h - U_1^g] + \frac{1}{\Delta x_2}[-2C_{23}] = 0$$

$$x_3x_1: \frac{1}{\Delta x_2}[U_2^c - U_2^a + U_2^b - U_2^d + U_2^e - U_2^g + U_2^h - U_2^f] + \frac{1}{\Delta x_3}[-2C_{31}] = 0 \qquad \text{(A14)}$$

From Eq.(A10), we could also derive

$$\frac{(U_1^a+U_1^c+U_1^e+U_1^g-U_1^b-U_1^d-U_1^f-U_1^h)}{\Delta x1} + \frac{(U_2^a+U_2^b+U_2^e+U_2^f-U_2^c-U_2^d-U_2^g-U_2^h)}{\Delta x2} + \frac{(U_3^a+U_3^b+U_3^c+U_3^d-U_3^e-U_3^f-U_3^g-U_3^h)}{\Delta x3} = 0 \qquad \text{(A15)}$$

which reduces 7 equations (A14) into 6 independent equations. Therefore, the coefficients in Eqs (A7-A9) as the six unknowns are determined as follows :

$$C_{12} = \frac{\Delta x_1}{2\Delta x_3}\left[-U_3^a + U_3^b + U_3^c - U_3^d + U_3^e - U_3^f - U_3^g + U_3^h\right]$$

$$C_{23} = \frac{\Delta x_2}{2\Delta x_1}\left[-U_1^a + U_1^b + U_1^c - U_1^d + U_1^e - U_1^f - U_1^g + U_1^h\right]$$

$$C_{31} = \frac{\Delta x_3}{2\Delta x_2}\left[-U_2^a + U_2^b + U_2^c - U_2^d + U_2^e - U_2^f - U_2^g + U_2^h\right]$$

$$C_{10} = \frac{\Delta x_1}{2\Delta x_2}\left[U_2^a - U_2^b - U_2^c + U_2^d\right] + \frac{\Delta x_1}{2\Delta x_3}\left[U_3^a - U_3^b - U_3^e + U_3^f + C_{31}\right] \qquad \text{(A16)}$$

$$C_{20} = \frac{\Delta x_2}{2\Delta x_1}\left[U_1^a - U_1^b - U_1^c + U_1^d + C_{12}\right] + \frac{\Delta x_2}{2\Delta x_3}\left[U_3^a - U_3^c - U_3^e + U_3^g\right]$$

$$C_{30} = \frac{\Delta x_3}{2\Delta x_1}\left[U_1^a - U_1^b - U_1^e + U_1^f\right] + \frac{\Delta x_3}{2\Delta x_2}\left[U_2^a - U_2^c - U_2^e + U_2^g + C_{23}\right]$$

Bibliography

Agrusta, R., J. van Hunen, S. Goes, J. Van Hunen, S. Goes, J. van Hunen, and S. Goes (2014), The effect of metastable pyroxene on the slab dynamics, *Geophys. Researc Lett.*, *41*(24), 8800–8808, doi:10.1002/2014GL062159.

Anderson, D. L. (1994), Superplumes or supercontinents?, *Geology*, *22*(4), 39–42.

Arndt, N. T., and S. L. Goldstein (1989), An open boundary between lower continental crust and mantle: its role in crust formation and crustal recycling, *Tectonophysics*, *161*(3-4), 201–212, doi:10.1016/0040-1951(89)90154-6.

Arndt, N. T., N. Coltice, H. Helmstaedt, and M. Gregoire (2009), Origin of Archean subcontinental lithospheric mantle: Some petrological constraints, *Lithos*, *109*(1-2), 61–71, doi:10.1016/j.lithos.2008.10.019.

Artemieva, I., and W. Mooney (2001), Thermal thickness and evolution of Precambrian lithosphere: a global study, *J. Geophys. Res.*, *106*(B8), 16387–16414.

Atanga, J., and D. Silvester (1992), Iterative methods for stabilized mixed velocity-pressure finite elements, *Int. J. Numer. Methods Fluids*, *14*(1), 71–81, doi:10.1002/fld.1650140106.

Aulbach, S. (2012), Craton nucleation and formation of thick lithospheric roots, *Lithos*, *149*, 16–30, doi:10.1016/j.lithos.2012.02.011.

Ballmer, M. D., J. van Hunen, G. Ito, P. J. Tackley, and T. A. Bianco (2007), Non-hotspot volcano chains originating from small-scale sublithospheric convection, *Geophys. Res. Lett.*, *34*(23), n/a–n/a, doi:10.1029/2007GL031636.

Ballmer, M. D., J. Van Hunen, G. Ito, T. a. Bianco, and P. J. Tackley (2009), Intraplate volcanism with complex age-distance patterns: A case for small-scale sublithospheric convection, *Geochemistry, Geophys. Geosystems*, *10*(6), doi:10.1029/2009GC002386.

Becker, M., and A. P. le Roex (2005), Geochemistry of South African On- and Off-craton, Group I and Group II Kimberlites: Petrogenesis and Source Region Evolution, *J. Petrol.*, *47*(4), 673–703, doi:10.1093/petrology/egi089.

Bédard, J. H. (2006), A catalytic delamination-driven model for coupled genesis of Archaean crust and sub-continental lithospheric mantle, *Geochim. Cosmochim. Acta*, *70*(5), 1188–1214, doi:10.1016/j.gca.2005.11.008.

Bédard, J. H., P. Brouillette, L. Madore, and A. Berclaz (2003), Archaean cratonization and deformation in the northern Superior Province, Canada: An evaluation of plate tectonic versus vertical tectonic models, *Precambrian Res.*, *127*(1-3), 61–87, doi:10.1016/S0301-9268(03)00181-5.

Bell, D., M. Schmitz, and P. Janney (2003), Mesozoic thermal evolution of the southern African mantle lithosphere, *Lithos*, *71*(2-4), 273–287, doi:10.1016/S0024-4937(03)00117-8.

Beuchert, M. J., Y. Y. Podladchikov, N. S. C. Simon, and L. H. Rüpke (2010), Modeling of craton stability using a viscoelastic rheology, *J. Geophys. Res.*, *115*(B11), B11413, doi:10.1029/2009JB006482.

Blankenbach, B. et al. (1989), A benchmark comparison for mantle convection codes, *Geophys. J. Int.*, *98*(1989), 23–38, doi:10.1111/j.1365-246X.1989.tb05511.x.

Bowring, S. A., and I. S. Williams (1999), Priscoan (4.00-4.03 Ga) orthogneisses from northwestern Canada, *Contrib. to Mineral. Petrol.*, *134*(1), 3–16, doi:10.1007/s004100050465.

Bowring, S. A., I. S. Williams, and W. Compston (1989), 3.96 Ga gneisses from the Slave province, Northwest Territories, Canada, *Geology*, *17*(11), 971–975, doi:10.1130/0091-7613(1989)017.

Boyd, F., D. Pearson, K. Hoal, and B. Hoal (2004), Garnet lherzolites from Louwrensia, Namibia: bulk composition and P/ T relations, *Lithos*, *77*, 573–592, doi:10.1016/j.lithos.2004.03.010.

Boyd, F. . (1973), A pyroxene geotherm, *Geochim. Cosmochim. Acta*, *37*(12), 2533–2546, doi:10.1016/0016-7037(73)90263-9.

Boyd, F. R. (1989), Compositional distinction between oceanic and cratonic lithosphere, *Earth Planet. Sci. Lett.*, *96*(1-2), 15–26, doi:10.1016/0012-821X(89)90120-9.

Boyd, F. R., and J. J. Gurney (1986), Diamonds and the african lithosphere., *Science*, *232*(2), 472–477, doi:10.1126/science.232.4749.472.

Boyd, F. R., N. P. Pokhilenko, D. G. Pearson, S. a. Mertzman, N. V. Sobolev, and L. W. Finger (1997), Composition of the Siberian cratonic mantle: evidence from Udachnaya peridotite xenoliths, *Contrib. to Mineral. Petrol.*, *128*(2-3), 228–246, doi:10.1007/s004100050305.

Brooks, Alexander Nelson (1981) A Petrov-Galerkin finite element formulation for convection dominated flows. Dissertation (Ph.D.), California Institute of Technology. http://resolver.caltech.edu/CaltechETD:etd-02012005-161447

Brune, S., A. a. Popov, and S. V. Sobolev (2013), Quantifying the thermo-mechanical impact of plume arrival on continental break-up, *Tectonophysics*, *604*(3), 51–59, doi:10.1016/j.tecto.2013.02.009.

Buck, W. R. (2006), The role of magma in the development of the Afro-Arabian Rift System, *Geol. Soc. London, Spec. Publ.*, *259*(1), 43–54, doi:10.1144/GSL.SP.2006.259.01.05.

Burov, E. B., and A. B. Watts (2006), The long-term strength of continental lithosphere : " jelly sandwich " or " crème brûlée "? Inside : The long-term strength of continental lithosphere : " jelly sandwich " or " crème brûlée "?, , *16*(1), doi:10.1130/1052-5173(2006)016<4.

Cammarano, F., S. Goes, P. Vacher, and D. Giardini (2003), Inferring upper-mantle temperatures from seismic velocities, *Phys. Earth Planet. Inter.*, *138*(3-4), 197–222, doi:10.1016/S0031-9201(03)00156-0.

Canil, D. (2004), Mildly incompatible elements in peridotites and the origins of mantle lithosphere, *Lithos*, *77*, 375–393, doi:10.1016/j.lithos.2004.04.014.

Carlson, R. R. W., D. G. Pearson, and D. D. E. James (2005), Physical, chemical, and chronological characteristics of continental mantle, *Rev. Geophys.*, (2004), 1–24, doi:10.1029/2004RG000156.

Carlson, R. W., A. J. Irving, D. J. Schulze, and B. C. Hearn Jr. (2004), Timing of Precambrian melt depletion and Phanerozoic refertilization events in the lithospheric mantle of the Wyoming Craton and adjacent Central Plains Orogen, *Lithos*, *77*(1-4), 453–472, doi:10.1016/j.lithos.2004.03.030.

Choukroune, P., H. Bouhallier, and N. T. Arndt (1995), Soft lithosphere during periods of Archaean crustal growth or crustal reworking, *Geol. Soc. London, Spec. Publ.*, *95*(1), 67–86, doi:10.1144/GSL.SP.1995.095.01.05.

Christensen, U. (1984), Convection with pressure- and temperature-dependent non-Newtonian rheology, *Geophys. J. Int.*, *77*(2), 343–384, doi:10.1111/j.1365-246X.1984.tb01939.x.

Christensen, U., and D. Yuen (1985), Layered convection induced by phase transitions, *J. Geophys. Res.*, *90*(B12), 10291–10300.

Cooper, C. M., and M. S. Miller (2014), Craton formation: Internal structure inherited from closing of the early oceans, *Lithosphere*, *6*(1), 35–42, doi:10.1130/L321.1.

Courtillot, V., C. Jaupart, I. Manighetti, P. Tapponnier, and J. Besse (1999), On causal links between flood basalts and continental breakup, *Earth Planet. Sci. Lett.*, *166*(3-4), 177–195, doi:10.1016/S0012-821X(98)00282-9.

DeCelles, P. G. (2002), Implications of shortening in the Himalayan fold-thrust belt for uplift of the Tibetan Plateau, *Tectonics*, *21*(6), doi:10.1029/2001TC001322.

Doin, M.-P., L. Fleitout, and U. Christensen (1997), Mantle convection and stability of depleted and undepleted continental lithosphere, *J. Geophys. Res.*, *102*(B2), 2771, doi:10.1029/96JB03271.

Duretz, T., D. a. May, T. V. Gerya, and P. J. Tackley (2011), Discretization errors and free surface stabilization in the finite difference and marker-in-cell method for applied geodynamics: A numerical study, *Geochemistry, Geophys. Geosystems*, *12*(7), doi:10.1029/2011GC003567.

Eaton, D. W., and H. K. Claire Perry (2013), Ephemeral isopycnicity of cratonic mantle keels, *Nat. Geosci.*, *6*(11), 967–970, doi:10.1038/ngeo1950.

Ebinger, C., and N. Sleep (1998), Cenozoic magmatism throughout east Africa resulting from impact of a single plume, *Nature*, *395*, 788–791.

Edwards, E., and R. Bridson (2012), A high-order accurate particle-in-cell method, *Int. J. Numer. Methods Eng.*, *90*(9), 1073–1088, doi:10.1002/nme.3356.

Erlank, A. J., F. G. Waters, C. J. Hawkesworth, E. Haggerty, H. L. Allsopp, R. S. Rickard, and M. Menzies (1987), Evidence for mantle metasomatism in peridotite nodules from the Kimberley pipes, South Africa, in *Mantle metasomatism*, pp. 221–311.

Ernst, R. E., J. W. Head, E. Parfitt, E. Grosfils, and L. Wilson (1995), Giant radiating dyke swarms on Earth and Venus, *Earth Sci. Rev.*, *39*, 1–58, doi:10.1016/0012-8252(95)00017-5.

Fan, W., and M. Menzies (1992), Destruction of aged lower lithosphere and accretion of asthenosphere mantle beneath eastern China, *Geotecton. Metallog.*, *16*, 171–181.

Farrell, P. E., and J. R. Maddison (2011), Conservative interpolation between volume meshes by local Galerkin projection, *Comput. Methods Appl. Mech. Eng.*, *200*(1-4), 89–100, doi:10.1016/j.cma.2010.07.015.

Fei, H., M. Wiedenbeck, D. Yamazaki, and T. Katsura (2013), Small effect of water on upper-mantle rheology based on silicon self-diffusion coefficients, *Nature*, *498*(7453), 213–215, doi:10.1038/nature12193.

Foley, S. F. (2008), Rejuvenation and erosion of the cratonic lithosphere, *Nat. Geosci.*, *1*(8), 503–510, doi:10.1038/ngeo261.

Foley, S. F. (2011), A reappraisal of redox melting in the earth's mantle as a function of tectonic setting and time, *J. Petrol.*, *52*(7-8), 1363–1391, doi:10.1093/petrology/egq061.

François, T., E. Burov, B. Meyer, and P. Agard (2012), Surface topography as key constraint on thermo-rheological structure of stable cratons, *Tectonophysics*, doi:10.1016/j.tecto.2012.10.009.

Gao, S., R. L. Rudnick, R. W. Carlson, W. F. McDonough, and Y. S. Liu (2002a), Re-Os evidence for replacement of ancient mantle lithosphere beneath the North China craton, *Earth Planet. Sci. Lett.*, *198*(3-4), 307–322, doi:10.1016/S0012-821X(02)00489-2.

Gao, S. et al. (2008), Recycling deep cratonic lithosphere and generation of intraplate magmatism in the North China Craton, *Earth Planet. Sci. Lett.*, *270*(1-2), 41–53, doi:10.1016/j.epsl.2008.03.008.

Gao, S. S., P. G. Silver, K. H. Liu, and S. Group (2002b), Mantle discontinuities beneath Southern Africa, , *29*(10), 4–7.

Gerya, T. V, and D. a Yuen (2003a), Rayleigh–Taylor instabilities from hydration and melting propel "cold plumes" at subduction zones, *Earth Planet. Sci. Lett.*, *212*(1-2), 47–62, doi:10.1016/S0012-821X(03)00265-6.

Gerya, T. V., and D. a. Yuen (2003b), Characteristics-based marker-in-cell method with conservative finite-differences schemes for modeling geological flows with strongly

variable transport properties, *Phys. Earth Planet. Inter.*, *140*(4), 293–318, doi:10.1016/j.pepi.2003.09.006.

Gibson, S. a., J. Malarkey, and J. a. Day (2008), Melt depletion and enrichment beneath the Western Kaapvaal craton: Evidence from Finsch peridotite xenoliths, *J. Petrol.*, *49*(10), 1817–1852, doi:10.1093/petrology/egn048.

Gibson, S. A., S. C. McMahon, J. a. Day, and J. B. Dawson (2013), Highly refractory lithospheric mantle beneath thetanzanian craton: Evidence from lashaine pre-metasomatic garnet-bearing peridotites, *J. Petrol.*, *54*(8), 1503–1546, doi:10.1093/petrology/egt020.

Di Giuseppe, E., J. Van Hunen, F. Funiciello, C. Faccenna, and D. Giardini (2008), Slab stiffness control of trench motion: Insights from numerical models, *Geochemistry, Geophys. Geosystems*, *9*(2), doi:10.1029/2007GC001776.

Goes, S., S. Van Der Lee, and S. van der Lee (2002), Thermal structure of the North American uppermost mantle inferred from seismic tomography, *J. Geophys. Res.*, *107*(B3), B32050, doi:10.1029/2000JB000049.

Goes, S., F. J. Simons, and K. Yoshizawa (2005), Seismic constraints on temperature of the Australian uppermost mantle, *Earth Planet. Sci. Lett.*, *236*(1-2), 227–237, doi:10.1016/j.epsl.2005.05.001.

Green, D. H., W. O. Hibberson, I. Kovács, and A. Rosenthal (2010), Water and its influence on the lithosphere-asthenosphere boundary., *Nature*, *467*(7314), 448–51, doi:10.1038/nature09369.

Griffin, W. ., C. . Ryan, F. . Kaminsky, S. Y. O'Reilly, L. . Natapov, T. . Win, P. . Kinny, and I. . Ilupin (1999), The Siberian lithosphere traverse: mantle terranes and the assembly of the Siberian Craton, *Tectonophysics*, *310*(1-4), 1–35, doi:10.1016/S0040-1951(99)00156-0.

Griffin, W. L., S. Y. O'Reilly, L. M. Natapov, and C. . Ryan (2003a), The evolution of lithospheric mantle beneath the Kalahari Craton and its margins, *Lithos*, *71*(2-4), 215–241, doi:10.1016/j.lithos.2003.07.006.

Griffin, W. L., S. Y. O'Reilly, N. Abe, S. Aulbach, R. M. Davies, N. J. Pearson, B. J. Doyle, and K. Kivi (2003b), The origin and evolution of Archean lithospheric mantle, in *Precambrian Research*, vol. 127, pp. 19–41.

Grove, T. L., and S. W. Parman (2004), Thermal evolution of the Earth as recorded by komatiites, *Earth Planet. Sci. Lett.*, *219*, 173–187, doi:10.1016/S0012-821X(04)00002-0.

Gung, Y., M. Panning, and B. Romanowicz (2003), Global anisotropy and the thickness of continents, *Nature*, *422*(April), 707–711, doi:10.1038/nature01557.1.

Gurnis, M. (1988), Large-scale mantle convection and the aggregation and dispersal of supercontinents, *Nature*, doi:10.1038/332695a0.

Herzberg, C. (1999), Phase equilibrium constraints on the formation of cratonic mantle, in *Mantle Petrology: Field Observations and High-Pressure Experimentation. Spec. Publ. Geochem. Soc. No. 6*, pp. 241–257.

Herzberg, C., and R. Rudnick (2012), Formation of cratonic lithosphere: An integrated thermal and petrological model, *Lithos*, *149*, 4–15, doi:10.1016/j.lithos.2012.01.010.

Herzberg, C., K. Condie, and J. Korenaga (2010), Thermal history of the Earth and its petrological expression, *Earth Planet. Sci. Lett.*, *292*(1-2), 79–88, doi:10.1016/j.epsl.2010.01.022.

Hill, R. I. (1991), Starting plumes and continental break-up, *Earth Planet. Sci. Lett.*, *104*(2-4), 398–416, doi:10.1016/0012-821X(91)90218-7.

Hirth, G., and D. L. Kohlstedt (1996), Water in the oceanic upper mantle: implications for rheology, melt extraction and the evolution of the lithosphere, *Earth Planet. Sci. Lett.*, *144*(1-2), 93–108.

Hirth, G., R. L. Evans, and A. D. Chave (2000), Comparison of continental and oceanic mantle electrical conductivity: Is the Archean lithosphere dry?, *Geochemistry, Geophys. Geosystems*, *1*(12), DOI: 10.1029/2000GC000048, doi:10.1029/2000GC000048.

Holtzman, B. K., D. S. H. King, and D. L. Kohlstedt (2012), Effects of stress-driven melt segregation on the viscosity of rocks, *Earth Planet. Sci. Lett.*, *359-360*, 184–193, doi:10.1016/j.epsl.2012.09.030.

Houseman, G. a., and P. Molnar (1997), Gravitational (Rayleigh-Taylor) instability of a layer with non-linear viscosity and convective thinning of continental lithosphere, *Geophys. J. Int.*, *128*(1), 125–150, doi:10.1111/j.1365-246X.1997.tb04075.x.

Hughes, T. J. R. (2000), *The Finite Element Method: Linear Static and Dynamic Finite Element Analysis*, Dover Publications.

Van Hunen, J., and M. B. Allen (2011), Continental collision and slab break-off: A comparison of 3-D numerical models with observations, *Earth Planet. Sci. Lett.*, *302*(1-2), 27–37, doi:10.1016/j.epsl.2010.11.035.

Van Hunen, J., and O. Čadek (2009), Reduced oceanic seismic anisotropy by small-scale convection, *Earth Planet. Sci. Lett.*, *284*(3-4), 622–629, doi:10.1016/j.epsl.2009.05.034.

Van Hunen, J., and S. Zhong (2003), New insight in the Hawaiian plume swell dynamics from scaling laws, *Geophys. Res. Lett.*, *30*(15), 3–6, doi:10.1029/2003GL017646.

Van Hunen, J., A. P. van den Berg, N. J. Vlaar, A. P. Van Den Berg, and N. J. Vlaar (2000), A thermo-mechanical model of horizontal subduction below an overriding plate, *Earth Planet. Sci. Lett.*, *182*(2), 157–169, doi:10.1016/S0012-821X(00)00240-5.

Van Hunen, J., S. Zhong, N. M. Shapiro, and M. H. Ritzwoller (2005), New evidence for dislocation creep from 3-D geodynamic modeling of the Pacific upper mantle structure, *Earth Planet. Sci. Lett.*, *238*, 146 – 155, doi:10.1016/j.epsl.2005.07.006.

Jackson, J. A., H. Austrheim, D. McKenzie, and K. Priestley (2004), Metastability, mechanical strength, and the support of mountain belts, *Geology*, *32*(7), 625–628, doi:10.1130/G20397.1.

James, D. E., M. J. Fouch, J. C. Vandecar, and S. Van Der Lee (2001), Tectospheric structure beneath southern Africa, *Geophys. Researc Lett.*, *28*(13), 2485–2488.

Jaupart, C., P. Molnar, and E. Cottrell (2007), Instability of a chemically dense layer heated from below and overlain by a deep less viscous fluid, *J. Fluid Mech.*, *572*, 433, doi:10.1017/S0022112006003521.

Jenny, P., S. B. Pope, M. Muradoglu, and D. a. Caughey (2001), A Hybrid Algorithm for the Joint PDF Equation of Turbulent Reactive Flows, *J. Comput. Phys.*, *166*(2), 218–252, doi:10.1006/jcph.2000.6646.

Jordan, T. H. (1978), Composition and development of the continental tectosphere, *Nature*, *274*(5671), 544–548, doi:10.1038/274544a0.

Jordan, T. H. (1988), Structure and Formation of the Continental Tectosphere, *J. Petrol.*, *21*(10), 11–37, doi:10.1093/petrology/Special_Volume.1.11.

Jull, M., and P. B. Kelemen (2001), On the conditions for lower custal convective instability, *J. Geophys. Res.*, *106*(B4), 6423–6446.

Kaban, M. K., P. Schwintzer, I. M. Artemieva, and W. D. Mooney (2003), Density of the continental roots: compositional and thermal contributions, *Earth Planet. Sci. Lett.*, *209*(1-2), 53–69, doi:10.1016/S0012-821X(03)00072-4.

Karato (2010), Rheology of the deep upper mantle and its implications for the preservation of the continental roots: A review, *Tectonophysics*, *481*(1-4), 82–98, doi:10.1016/j.tecto.2009.04.011.

Karato, S. (2006), Influence of hydrogen-related defects on the electrical conductivity and plastic deformation of mantle minerals : a critical review, *Geeophysical Monogr. Ser.*, *168*, 113–129, doi:10.1029/168GM09.

Karato, S., and P. Wu (1993), Rheology of the upper mantle: a synthesis., *Science (80-.).*, *260*(5109), 771–778.

Keefner, J. W., S. J. Mackwell, D. L. Kohlstedt, and F. Heidelbach (2011), Dependence of dislocation creep of dunite on oxygen fugacity: Implications for viscosity variations in Earth's mantle, *J. Geophys. Res.*, *116*(B5), 1–15, doi:10.1029/2010JB007748.

Van Keken, P. E., S. D. King, H. Schmeling, U. R. Christensen, D. Neumeister, and M.-P. Doin (1997), A comparison of methods for the modeling of thermochemical convection, *J. Geophys. Res.*, *102*(B10), 22477–22495, doi:10.1029/97JB01353.

Van Keken, P., and C. Gable (1995), The interaction of a plume with a rheological boundary: A comparison between two-and three-dimensional models, *J. Geophys. Res. Solid Earth*, *100*(B10), 20291–20302.

Kelemen, P. B., H. J. B. Dick, and J. E. Quick (1992), Formation of harzburgite by pervasive melt/rock reaction in the upper mantle, *Nature*, *358*(6388), 635–641, doi:10.1038/358635a0.

Kelly, R. K., P. B. Kelemen, and M. Jull (2003), Buoyancy of the continental upper mantle, *Geochemistry, Geophys. Geosystems*, *4*(2), doi:10.1029/2002GC000399.

King, S. (2005), Archean cratons and mantle dynamics, *Earth Planet. Sci. Lett.*, *234*(1-2), 1–14, doi:10.1016/j.epsl.2005.03.007.

King, S. D., C. Lee, P. E. Van Keken, W. Leng, S. Zhong, E. Tan, N. Tosi, and M. C. Kameyama (2010), A community benchmark for 2-D Cartesian compressible convection in the Earth's mantle, *Geophys. J. …*, *180*, 73–87, doi:10.1111/j.1365-246X.2009.04413.x.

Kobussen, A. F., W. L. Griffin, S. Y. O'Reilly, and S. R. Shee (2008), Ghosts of lithospheres past: Imaging an evolving lithospheric mantle in southern Africa, *Geology*, *36*(7), 515, doi:10.1130/G24868A.1.

Kohlstedt, D. L., B. Evans, and S. J. Mackwell (1995), Strength of the lithosphere: Constraints imposed by laboratory experiments, *J. Geophys. Res.*, doi:10.1029/95JB01460.

Konzett, J., R. A. Armstrong, R. J. Sweeney, and W. Compston (1998), The timing of MARID metasomatism in the Kaapvaal mantle: an ion probe study of zircons from MARID xenoliths, *Earth Planet. Sci. Lett.*, *160*(1-2), 133–145, doi:10.1016/S0012-821X(98)00073-9.

Kopylova, M. G., and J. K. Russell (2000), Chemical stratification of cratonic lithosphere: Constraints from the Northern Slave craton, Canada, *Earth Planet. Sci. Lett.*, *181*(1-2), 71–87, doi:10.1016/S0012-821X(00)00187-4.

Van Kranendonk, M. J., R. H. Smithies, W. L. Griffin, D. L. Huston, a. H. Hickman, D. C. Champion, C. R. Anhaeusser, and F. Pirajno (2014), Making it thick: a volcanic plateau origin of Palaeoarchean continental lithosphere of the Pilbara and Kaapvaal cratons, *Geol. Soc. London, Spec. Publ.*, doi:10.1144/SP389.12.

Krystopowicz, N. J., and C. a. Currie (2013), Crustal eclogitization and lithosphere delamination in orogens, *Earth Planet. Sci. Lett.*, *361*, 195–207, doi:10.1016/j.epsl.2012.09.056.

Kusky, T. M., B. F. Windley, and M.-G. Zhai (2007), Lithospheric thinning in eastern Asia; constraints, evolution, and tests of models, *Geol. Soc. London, Spec. Publ.*, *280*(1), 331–343, doi:10.1144/SP280.18.

Lee, C., and R. Rudnick (1999), Compositionally stratified cratonic lithosphere: petrology and geochemistry of peridotite xenoliths from the Labait tuff cone, Tanzania, in *Proceedings of the 7th international Kimberlite conference*, pp. 503–521.

Lee, C.-T. A. (2006), Geochemical/Petrologic constraintOn the origin of cratonic mantle, *Geophys. Monogr. - Am. Geophys. union*, *164*, 89–114, doi:10.1029/164gm08.

Lee, C.-T. a., and E. J. Chin (2014), Calculating melting temperatures and pressures of peridotite protoliths: Implications for the origin of cratonic mantle, *Earth Planet. Sci. Lett.*, *403*, 273–286, doi:10.1016/j.epsl.2014.06.048.

Lee, C.-T. A., X. Cheng, and U. Horodyskyj (2006), The development and refinement of continental arcs by primary basaltic magmatism, garnet pyroxenite accumulation, basaltic recharge and delamination: insights from the Sierra Nevada, California, *Contrib. to Mineral. Petrol.*, *151*(2), 222–242, doi:10.1007/s00410-005-0056-1.

Lee, C.-T. A., P. Luffi, and E. J. Chin (2011), Building and Destroying Continental Mantle, *Annu. Rev. Earth Planet. Sci.*, *39*(1), 59–90, doi:10.1146/annurev-earth-040610-133505.

Lenardic, A., and L. Moresi (1999), Some thoughts on the stability of cratonic lithosphere: Effects of buoyancy and viscosity, *J. Geophys. Res.*, *104*(B6), 12747–12758.

Lenardic, A., L. Moresi, and H. Muhlhaus (2000), The role of mobile belts for the longevity of deep cratonic lithosphere: The crumple zone model, *Geophys. Researc Lett.*, *27*(8), 1235–1238.

Lenardic, A., L. Moresi, and H. Mühlhaus (2003), Longevity and stability of cratonic lithosphere: insights from numerical simulations of coupled mantle convection and continental tectonics, *J. Geophys. Res.*, *108*, 1–15, doi:10.1029/2002JB001859.

Levander, a, B. Schmandt, M. S. Miller, K. Liu, K. E. Karlstrom, R. S. Crow, C.-T. a Lee, and E. D. Humphreys (2011), Continuing Colorado plateau uplift by delamination-style convective lithospheric downwelling., *Nature*, *472*(7344), 461–5, doi:10.1038/nature10001.

Li, Z.-X., and S. Zhong (2009), Supercontinent–superplume coupling, true polar wander and plume mobility: Plate dominance in whole-mantle tectonics, *Phys. Earth Planet. Inter.*, *176*(3-4), 143–156, doi:10.1016/j.pepi.2009.05.004.

Liu, D. Y., A. P. Nutman, W. Compston, J. S. Wu, and Q. H. Shen (1992), Remnants of >=3800 Ma crust in the Chinese part of the Sino-Korean craton, *Geology*, *20*(4), 339–342, doi:10.1130/0091-7613(1992)020.

Liu, X.-M., and R. L. Rudnick (2011), Constraints on continental crustal mass loss via chemical weathering using lithium and its isotopes., *Proc. Natl. Acad. Sci. U. S. A.*, *108*(52), 20873–80, doi:10.1073/pnas.1115671108.

Mainprice, D., A. Tommasi, H. Couvy, P. Cordier, and D. J. Frost (2005), Pressure sensitivity of olivine slip systems and seismic anisotropy of Earth's upper mantle., *Nature*, *433*(7027), 731–733, doi:10.1038/nature03266.

Manglik, A., and U. R. Christensen (1997), Effect of mantle depletion buoyancy on plume flow and melting beneath a stationary plate, *J. Geophys. Res.*, *102*(B3), 5019, doi:10.1029/96JB03623.

Mareschal, J. C., and C. Jaupart (2006), Archean thermal regime and stabilization of the cratons, in *Archean Geodynamics and Environments*, vol. 164, pp. 61–73.

Mather, K. a., D. G. Pearson, D. McKenzie, B. A. Kjarsgaard, and K. Priestley (2011), Constraints on the depth and thermal history of cratonic lithosphere from peridotite xenoliths, xenocrysts and seismology, *Lithos*, *125*(1-2), 729–742, doi:10.1016/j.lithos.2011.04.003.

McKenzie, D., and K. Priestley (2008), The influence of lithospheric thickness variations on continental evolution, *Lithos*, *102*, 1–11, doi:10.1016/j.lithos.2007.05.005.

Mckenzie, D., J. Jackson, and K. Priestley (2005), Thermal structure of oceanic and continental lithosphere, *Earth Planet. Sci. Lett.*, *233*(3-4), 337–349, doi:10.1016/j.epsl.2005.02.005.

Mckenzie, D. P., J. M. Roberts, and N. O. Weiss (1974), Convection in the earth's mantle: towards a numerical simulation, *J. Fluid Mech.*, *62*(03), 465, doi:10.1017/S0022112074000784.

McNally, C. (2011), Divergence-free interpolation of vector fields from point values–exact $\nabla \cdot B = 0$ in numerical simulations, *Mon. Not. R. Astron. Lett.*, *413*(1), L76–L80, doi:10.1111/j.1745-3933.2011.01037.x.

McNamara, A. K., and S. Zhong (2004), The influence of thermochemical convection on the fixity of mantle plumes, *Earth Planet. Sci. Lett.*, *222*(2), 485–500, doi:10.1016/j.epsl.2004.03.008.

Mei, S., and D. L. Kohlstedt (2000a), Influence of water on plastic deformation of olivine aggregates: 1.Diffusion creep regime, *J. Geophys. Res.*, *105*(B9), 21471–21481, doi:10.1029/2000JB900180.

Mei, S., and D. L. Kohlstedt (2000b), Influence of water on plastic deformation of olivine aggregates: 2. Dislocation creep regime, *J. Geophys. Res.*, *105*(B9), 21471, doi:10.1029/2000JB900180.

Meyer, D., and P. Jenny (2004), Conservative velocity interpolation for PDF methods, *PAMM*, *467*, 466–467, doi:10.1002/pamm.200410.

Michaut, C., and C. Jaupart (2007), Secular cooling and thermal structure of continental lithosphere, *Earth Planet. Sci. Lett.*, *257*(1-2), 83–96, doi:10.1016/j.epsl.2007.02.019.

Michaut, C., C. Jaupart, and J.-C. Mareschal (2009), Thermal evolution of cratonic roots, *Lithos*, *109*(1-2), 47–60, doi:10.1016/j.lithos.2008.05.008.

Mooney, W. D., and J. E. Vidale (2003), Thermal and chemical variations in subcrustal cratonic lithosphere: evidence from crustal isostasy, *Lithos*, *71*(2-4), 185–193, doi:10.1016/j.lithos.2003.07.004.

Moresi, L., S. Zhong, and M. Gurnis (1996), The accuracy of finite element solutions of Stokes's flow with strongly varying viscosity, *Phys. Earth Planet. Inter.*, *97*(1-4), 83–94, doi:10.1016/0031-9201(96)03163-9.

Moresi, L., F. Dufour, and H.-B. Mühlhaus (2003), A Lagrangian integration point finite element method for large deformation modeling of viscoelastic geomaterials, *J. Comput. Phys.*, *184*(2), 476–497, doi:10.1016/S0021-9991(02)00031-1.

Moresi, L., S. Quenette, V. Lemiale, C. Mériaux, B. Appelbe, and H.-B. Mühlhaus (2007), Computational approaches to studying non-linear dynamics of the crust and mantle, *Phys. Earth Planet. Inter.*, *163*(1-4), 69–82, doi:10.1016/j.pepi.2007.06.009.

Moresi, L.-N., and V. S. Solomatov (1995), Numerical investigation of 2D convection with extremely large viscosity variations, *Phys. Fluids*, *7*(9), 2154–2162, doi:10.1063/1.868465.

Morgan, P. (1984), The thermal structure and thermal evolution of the continental lithosphere, *Phys. Chem. Earth*, *15*, 107–193, doi:10.1016/0079-1946(84)90006-5.

Niu, Y. (2005), Generation and Evolution of Basaltic Magmas : Some Basic Concepts and a New View on the Origin of Mesozoic-Cenozoic Basaltic Volcanism in Eastern China, *Geol. J. Chine Univ.*, *11*(1), 9–46.

Nyblade, A. A. (1999), Heat flow and the structure of Precambrian lithosphere, , 81–91.

Nyblade, A. A., and N. H. Sleep (2003), Long lasting epeirogenic uplift from mantle plumes and the origin of the Southern African Plateau, *Geochemistry, Geophys. Geosystems*, *4*(12), doi:10.1029/2003GC000573.

O'Connor, J. M., W. Jokat, A. P. le Roex, C. Class, J. R. Wijbrans, S. Keßling, K. F. Kuiper, and O. Nebel (2012), Hotspot trails in the South Atlantic controlled by plume and plate tectonic processes, *Nat. Geosci.*, *5*(10), 735–738, doi:10.1038/ngeo1583.

O'Neill, C. J., a. Lenardic, W. L. Griffin, and S. Y. O'Reilly (2008), Dynamics of cratons in an evolving mantle, *Lithos*, *102*(1-2), 12–24, doi:10.1016/j.lithos.2007.04.006.

Pearson (1999), The age of continental roots, *Lithos*, *48*(1-4), 171–194, doi:10.1016/S0024-4937(99)00026-2.

Pearson, D. ., R. W. Carlson, S. B. Shirey, F. R. Boyd, and P. H. Nixon (1995), Stabilisation of Archaean lithospheric mantle : A Re-0s isotope study of peridotite xenoliths from the Kaapvaal craton, *Earth Planet. Sci. Lett.*, *134*, 341–357.

Pearson, D. ., G. . Irvine, D. . Ionov, F. . Boyd, and G. . Dreibus (2004), Re–Os isotope systematics and platinum group element fractionation during mantle melt extraction: a study of massif and xenolith peridotite suites, *Chem. Geol.*, *208*(1-4), 29–59, doi:10.1016/j.chemgeo.2004.04.005.

Pearson, D. G., and G. M. Nowell (2002), The continental lithospheric mantle: characteristics and significance as a mantle reservoir., *Philos. Trans. A. Math. Phys. Eng. Sci.*, *360*(1800), 2383–410, doi:10.1098/rsta.2002.1074.

Pearson, D. G., and N. Wittig (2014), The Formation and Evolution of Cratonic Mantle Lithosphere - Evidence from Mantle Xenoliths, in *Treatise on Geochemistry: Second Edition*, vol. 3, pp. 255–292, Elsevier Ltd.

Pearson, D. G. D., and N. Wittig (2008), Formation of Archaean continental lithosphere and its diamonds: the root of the problem, *J. Geol. Soc. London.*, *165*(5), 895–914, doi:10.1144/0016-76492008-003.

Peslier, A. H., A. B. Woodland, D. R. Bell, and M. Lazarov (2010), Olivine water contents in the continental lithosphere and the longevity of cratons., *Nature*, *467*(7311), 78–81, doi:10.1038/nature09317.

Peslier, A. H., A. B. Woodland, D. R. Bell, M. Lazarov, and T. J. Lapen (2012), Metasomatic control of water contents in the Kaapvaal cratonic mantle, *Geochim. Cosmochim. Acta*, *97*, 213–246, doi:10.1016/j.gca.2012.08.028.

Poliakov, a, and Y. Podladchikov (1992), Diapirism and topography, *Geophys. J. Int.*, 553–564, doi:10.1111/j.1365-246X.1992.tb00117.x.

Poudjom Djomani, Y. H., W. L. Griffin, S. Y. O'Reilly, and B. J. Doyle (2005), Lithospheric domains and controls on kimberlite emplacement, Slave Province, Canada: Evidence from elastic thickness and upper mantle composition, *Geochemistry, Geophys. Geosystems*, *6*(10), n/a–n/a, doi:10.1029/2005GC000978.

Priestley, K., and D. Mckenzie (2006), The thermal structure of the lithosphere from shear wave velocities, *Earth Planet. Sci. Lett.*, *244*(1-2), 285–301, doi:10.1016/j.epsl.2006.01.008.

Priestley, K., and D. McKenzie (2013), The relationship between shear wave velocity, temperature, attenuation and viscosity in the shallow part of the mantle, *Earth Planet. Sci. Lett.*, *381*, 78–91, doi:10.1016/j.epsl.2013.08.022.

Ranalli, G., and S.-I. Karato (1995), *Rheology of the Earth*, Springer Science & Business Media.

Rapp, R. P., N. Shimizu, and M. D. Norman (2003), Growth of early continental crust by partial melting of eclogite, *Nature*, *425*, doi:10.1038/nature02031.

Ribe, N. M., and U. R. Christensen (1994), Three-dimensional modeling of plume-lithosphere interaction, *J. Geophys. Res.*, *99*(B1), 669–682, doi:10.1029/93JB02386.

Richardson, S. H., J. J. Gurney, A. J. Erlank, and J. W. Harris (1984), Origin of diamonds in old enriched mantle, *Nature*, *310*(5974), 198–202, doi:10.1038/310198a0.

Rollinson, H. (2010), Coupled evolution of Archean continental crust and subcontinental lithospheric mantle, *Geology*, *38*(12), 1083–1086, doi:10.1130/G31159.1.

Rozel, A. (2012), Impact of grain size on the convection of terrestrial planets, *Geochemistry, Geophys. Geosystems*, *13*(10), n/a–n/a, doi:10.1029/2012GC004282.

Rudnick, R. L., and A. A. Nyblade (1999), The thickness and heat production of Archean lithosphere: constraints from xenolith thermobarometry and surface heat flow, in *Mantle Petrology: Field Observations and High-Pressure Experimentation. Spec. Publ. Geochem. Soc. No. 6*, vol. 6, pp. 3–12.

Rudnick, R. L. R. (1995), Making continental crust, *Nature*, *378*(6557), 570–577, doi:10.1038/378571a0.

Schmeling, H. (2000), Partial melting and melt segregation in a convecting mantle, *Phys. Chem. Partial. Molten Rocks*, *11*, 141–178, doi:10.1007/978-94-011-4016-4.

Schmeling, H., and H. Wallner (2012), Magmatic lithospheric heating and weakening during continental rifting: A simple scaling law, a 2-D thermomechanical rifting model and the East African Rift System, *Geochemistry, Geophys. Geosystems*, *13*(8), doi:10.1029/2012GC004178.

Schmeling, H. et al. (2008), A benchmark comparison of spontaneous subduction models—Towards a free surface, *Phys. Earth Planet. Inter.*, *171*(1-4), 198–223, doi:10.1016/j.pepi.2008.06.028.

Schubert, G., and D. L. Turcotte (2004), *Mantle Convection in the Earth and Planets*, Cambridge University Press, Cambridge.

Schubert, G., D. Stevenson, and P. Cassen (1980), Whole planet cooling and the radiogenic heat source contents of the earth and moon, , *85*, 2531–2538, doi:10.1029/JB085iB05p02531.

Schutt, D. L., and C. E. Lesher (2006), Effects of melt depletion on the density and seismic velocity of garnet and spinel lherzolite, *J. Geophys. Res.*, *111*(B5), B05401, doi:10.1029/2003JB002950.

Schutt, D. L., and C. E. Lesher (2010), Compositional trends among Kaapvaal Craton garnet peridotite xenoliths and their effects on seismic velocity and density, *Earth Planet. Sci. Lett.*, *300*(3-4), 367–373, doi:10.1016/j.epsl.2010.10.018.

Shapiro, S., B. Hager, and T. Jordan (1999), Stability and dynamics of the continental tectosphere, *Lithos*, *48*(February), 115–133.

Shirey, S. B., and R. J. Walker (1998), The Re-Os isotope system in cosmochemistry and high-temperature geochemistry, *Annu. Rev. Earth Planet. Sci.*, *26*(1), 423–500, doi:10.1146/annurev.earth.26.1.423.

Simon, N., G. R. Irvine, and G. Davies (2003), The origin of garnet and clinopyroxene in "depleted" Kaapvaal peridotites, *Lithos*, *71*(2-4), 289–322, doi:10.1016/S0024-4937(03)00118-X.

Sleep, N. H. (2003), Survival of Archean cratonal lithosphere, *J. Geophys. Res.*, *108*(B6), 1–29, doi:10.1029/2001JB000169.

Sleep, N. H. (2005), Evolution of the Continental Lithosphere, *Annu. Rev. Earth Planet. Sci.*, *33*(1), 369–393, doi:10.1146/annurev.earth.33.092203.122643.

Sleep, N. H., C. J. Ebinger, and J.-M. Kendall (2002), Deflection of mantle plume material by cratonic keels, *Geol. Soc. London, Spec. Publ.*, *199*(1), 135–150, doi:10.1144/GSL.SP.2002.199.01.08.

Smit, K. V., D. G. Pearson, T. Stachel, and M. Seller (2014), Peridotites from Attawapiskat, Canada: Mesoproterozoic Reworking of Palaeoarchaean Lithospheric Mantle beneath the Northern Superior Superterrane, *J. Petrol.*, *55*(9), 1829–1863, doi:10.1093/petrology/egu043.

Solomatov, V. S., and L.-N. Moresi (2000), Scaling of time-dependent stagnant lid convetion: Application to small-scale convection on earth and other terrestrial planets, *J. Geophys. Res.*, *105*(B9), 21795–21817.

Tackley, P. J. (2008), Modelling compressible mantle convection with large viscosity contrasts in a three-dimensional spherical shell using the yin-yang grid, *Phys. Earth Planet. Inter.*, *171*, 7–18, doi:10.1016/j.pepi.2008.08.005.

Tackley, P. J., and S. D. King (2003), Testing the tracer ratio method for modeling active compositional fields in mantle convection simulations, *Geochemistry, Geophys. Geosystems*, *4*(4), n/a–n/a, doi:10.1029/2001GC000214.

Tackley, P. J., G. Schubert, G. A. Glatzmaier, P. Schenk, J. T. Ratcliff, and J.-P. Matas (2001), Three-Dimensional Simulations of Mantle Convection in Io, *Am. Geophys. Union*, *28*, 231–253, doi:10.1006/icar.2000.6536.

Tang, Y.-J., H. Zhang, J.-F. Ying, and B.-X. Su (2013), Widespread refertilization of cratonic and circum-cratonic lithospheric mantle, *Earth-Science Rev.*, *118*(0), 45–68, doi:http://dx.doi.org/10.1016/j.earscirev.2013.01.004.

Tappe, S., S. F. Foley, A. Stracke, R. L. Romer, B. a. Kjarsgaard, L. M. Heaman, and N. Joyce (2007), Craton reactivation on the Labrador Sea margins: 40Ar/39Ar age and Sr–Nd–Hf–Pb isotope constraints from alkaline and carbonatite intrusives, *Earth Planet. Sci. Lett.*, *256*(3-4), 433–454, doi:10.1016/j.epsl.2007.01.036.

Tappe, S., D. G. Pearson, G. Nowell, T. Nielsen, P. Milstead, and K. Muehlenbachs (2011), A fresh isotopic look at Greenland kimberlites: Cratonic mantle lithosphere imprint on deep source signal, *Earth Planet. Sci. Lett.*, *305*(1-2), 235–248, doi:10.1016/j.epsl.2011.03.005.

Thielmann, M., D. a. May, and B. J. P. Kaus (2014), Discretization Errors in the Hybrid Finite Element Particle-in-cell Method, *Pure Appl. Geophys.*, *171*(9), 2165–2184, doi:10.1007/s00024-014-0808-9.

Tian, X., Z. Liu, S. Si, and Z. Zhang (2013), The crustal thickness of NE Tibet and its implication for crustal shortening, *Tectonophysics*, *634*, 198–207, doi:10.1016/j.tecto.2014.07.001.

Vennell, R., and R. Beatson (2009), A divergence-free spatial interpolator for large sparse velocity data sets, *J. Geophys. Res.*, *114*(C10), C10024, doi:10.1029/2008JC004973.

Wang, H., J. van Hunen, D. G. Pearson, and M. B. Allen (2014), Craton stability and longevity: The roles of composition-dependent rheology and buoyancy, *Earth Planet. Sci. Lett.*, *391*, 224–233, doi:10.1016/j.epsl.2014.01.038.

Wang, Y., J. Huang, and S. Zhong (2015), Episodic and Multi-staged Gravitational Instability of Cratonic Lithosphere and its Implications for Reactivation of the North China Craton, *Geochemistry Geophys. Geosystems*, doi:doi: 10.1002/2014GC005681.

Weinberg, R. F., and H. Schmeling (1992), Polydiapirs: multiwavelength gravity structures, *J. Struct. Geol.*, *14*, 425–436, doi:10.1016/0191-8141(92)90103-4.

Wittig, N., D. G. Pearson, M. Webb, C. J. Ottley, G. J. Irvine, M. Kopylova, S. M. Jensen, and G. M. Nowell (2008), Origin of cratonic lithospheric mantle roots : A geochemical study of peridotites from the North Atlantic Craton , West Greenland, *Earth Planet. Sci. Lett.*, *274*, 24–33, doi:10.1016/j.epsl.2008.06.034.

Yoshida, M. (2010), Preliminary three-dimensional model of mantle convection with deformable, mobile continental lithosphere, *Earth Planet. Sci. Lett.*, *295*(1-2), 205–218, doi:10.1016/j.epsl.2010.04.001.

Yoshida, M. (2012), Dynamic role of the rheological contrast between cratonic and oceanic lithospheres in the longevity of cratonic lithosphere: A three-dimensional numerical study, *Tectonophysics*, *532–535*(0), 156–166, doi:http://dx.doi.org/10.1016/j.tecto.2012.01.029.

Yoshida, M. (2013), Mantle temperature under drifting deformable continents during the supercontinent cycle, , *40*(February), 681–686, doi:10.1002/GRL.50151.

Yoshida, M., and M. Santosh (2011), Supercontinents, mantle dynamics and plate tectonics: A perspective based on conceptual vs. numerical models, *Earth-Science Rev.*, *105*(1-2), 1–24, doi:10.1016/j.earscirev.2010.12.002.

Yu, C.-Q., W.-P. Chen, J.-Y. Ning, K. Tao, T.-L. Tseng, X.-D. Fang, Y. John Chen, and R. D. van der Hilst (2012), Thick crust beneath the Ordos plateau: Implications for instability of the North China craton, *Earth Planet. Sci. Lett.*, *357-358*, 366–375, doi:10.1016/j.epsl.2012.09.027.

Zegers, van K. P. E. (2001), Middle Archean continent formation by crustal delamination, *Geology*, *29*(12), 1083–1086.

Zhong, S. (1996), Analytic solutions for Stokes' flow with lateral variations in viscosity, *Geophys. J. Int.*, *124*(1), 18–28, doi:10.1111/j.1365-246X.1996.tb06349.x.

Zhong, S., M. T. Zuber, L. Moresi, and G. Michael (2000), Role of temperature-dependent viscosity and surface plates in spherical shell models of mantle convection, *J. Geophys. Res.*, *105*(B5), 11063–11082, doi:10.1029/2000JB900003.

Zhu, R., and T. Zheng (2009), Destruction geodynamics of the North China craton and its Paleoproterozoic plate tectonics, *Chinese Sci. Bull.*, *54*(19), 3354–3366, doi:10.1007/s11434-009-0451-5.